

CHARM PRODUCTION IN PION-NUCLEON INTERACTIONS

by

Avram Dan Montag

**A Dissertation
Presented to the
Faculty of Princeton University
in Candidacy for the Degree of
Doctor of Philosophy**

**Recommended for Acceptance by the
Department of Physics**

October 1982

ABSTRACT

Hadronic production of charm has been investigated using a π^- beam incident on a nucleon target at momenta of 200 and 250 GeV/c. At 200 GeV/c the total cross section for the production of charged D^* mesons, $[\sigma(D^{*+}) + \sigma(D^{*-})]$, was measured to be $8.4 \pm 2.8 \mu\text{b}$. At 250 GeV/c the result was $0.8 \pm 2.9 \mu\text{b}$. The average of these values, $4.6 \pm 2.0 \mu\text{b}$, corresponds to a total charm production cross section of $8.8 \pm 3.8 \mu\text{b}$. Results are also reported on the production of states that decay into $\Lambda - \pi$ pairs.

ACKNOWLEDGEMENTS

The experiment whose results are presented in this thesis was conceived and the essential components of the apparatus were designed well before I entered graduate school. My entire career as a graduate student was spent working on this enterprise, starting as an unskilled laborer, serving as an apprentice, and finally being given the first look at a set of data. In acknowledging the contributions of my colleagues who participated in Fermilab Experiment 650, I also acknowledge my debt to them as teachers and guides.

The co-spokesmen of the collaboration were Robert Webb and Michael Witherell. Professor Webb took principal responsibility for coordinating and overseeing the construction of the apparatus. Professor Witherell guided the analysis and provided the major portion of the track reconstruction program. I owe all of my knowledge of the techniques of experimental high energy physics to these two men.

Steven Sherman graciously delayed the start of a post doctoral appointment in order to help get the experiment running, most notably by reviving and updating the data acquisition system. The core of the reconstruction program for the slow pion spectrometer was provided by Armand Zylberstejn. Daniela Maurizio and Rosanna Cester-Regge provided many independent checks throughout the analysis. Sandro Palestini assisted in the frustrating task of aligning the drift chambers off-line. Val Fitch, who came up with the idea of exploiting the special properties of the D^0 for this experiment, played the necessary role of devil's advocate in his scrutiny of the analysis and provided the algorithm for reconstructing the track of the slow pion.

The final run of the experiment was scheduled on extremely short notice, but the technical staffs at Princeton, Saclay, and Fermilab met the challenge. Special mention must be made of Marius Isaila for the design of the mass matrix module, of Carl Bopp for the data acquisition system and enlarged buffer memory, and of Ann David for the layout of the electronics for the mass matrix module as well as the new drift chambers.

Except for the segmented target which was constructed at Fermilab and the slow pion spectrometer which was constructed at Saclay, all of the apparatus was built by the staff of the Princeton University Elementary Particles Laboratory. Richard Rabberman who worked on the assembly of the mass matrix and John Quinn and William Sands who constructed the drift chambers should be singled out in connection with Experiment 650.

For the preparation of this thesis I am indebted to the critical insight of my advisor, Professor Fitch, and of Professor Bernard Pope, both of whom read several versions of the entire manuscript. I am also grateful to Ann David for the editorial guidance she provided.

8"28e15

CONTENTS

ABSTRACT	ii
ACKNOWLEDGEMENTS	iii

<u>Chapter</u>	<u>Page</u>
I. INTRODUCTION	1
Why Measure Charm Production Cross Sections?	1
Modeling Hadronic Charm Production	9
The Experimental Situation	18
This Experiment	30
II. APPARATUS	33
Overview of the Spectrometer	33
Beam	39
Target	44
Trigger and Mass Matrix	48
Drift Chambers	59
Cerenkov Counters	66
Data Acquisition and On-Line Monitoring	71
III. EVENT RECONSTRUCTION	73
Drift Chamber Alignment	73
Track Reconstruction	79
Particle Identification	84
Fast Arms Momentum and Mass Calculation	91
Momentum and Angles in the Slow Arms	93
Q Value Resolution	97
Resolution in the Fast Arms	99
IV. RESULTS	103
The J/ψ Signal	103
Lambda Production and Correlations	108
D^*	116
Conclusions	126

LIST OF FIGURES

<u>Figure</u>	<u>Page</u>
1. Lowest Order QCD Charm Production Processes	12
2. BCF Collaboration Mass Plots	28
3. Mass Plots from the 200 GeV/c Run	32
4. Layout of the Spectrometers	36
5. Geometric Acceptance of the Spectrometers	38
6. Beam Profile at Target	41
7. Time Structure of the Beam Spill	43
8. Target Assembly	45
9. Z of Fast Arm Vertex	47
10. Trigger Logic	49
11. Mass Matrix Logic	53
12. Choice of Two Arm Coincidences	55
13. $\pi - K$ Mass Spectra	58
14. First Slow Arm Drift Chamber	60
15. First Fast Arm Drift Chamber	64
16. Y Vertex in Fast Arms	65
17. Cerenkov Counters	70
18. Hit - Fit in the Front Slow Arm Chamber	78
19. Track Reconstruction Program Flow Chart	80
20. Pulse Height Spectrum in Threshold Cerenkov Counter	85
21. Variation in Phototube Calibration	86
22. Excitation Curve for Threshold Cerenkov Counter	87
23. Kaons in the Differential Cerenkov Counter	89
24. Proton Feed-Through in the Differential Cerenkov Counter	90
25. Muon Pair Masses 250 GeV/c Run	104
26. Muon Pair Masses 200 GeV/c Run	107
27. Λ Candidates	110
28. $\Lambda - \pi$ Mass Spectra	112
29. $\Lambda - \pi$ Acceptance Versus Mass	113
30. $\Lambda - \pi$ Differential Cross Section	115
31. $K \pi \pi$ Mass Spectrum	117

32.	Mass Versus Q Scatter Plot	118
33.	D ⁺ Mass Plots	122
34.	Background Distributions	124
35.	Mass Plot for Q near 7.1 MeV	125

LIST OF TABLES

<u>Table</u>		<u>PAGE</u>
1.	CERN Beam Dump Results	21
2.	Scintillator Hodoscopes	51
3.	Drift Chamber Characteristics	62
4.	Gases Used in E650 Cerenkov Counters	66
5.	Primary Event Format	71
6.	Data Summary Tape Format	84
7.	Magnetic Field Parameters	92
8.	Sensitivity for J/ψ	105
9.	Relative Sensitivity for J/ψ	108
10.	Sensitivity for D ⁺	126

Chapter I

INTRODUCTION

1.1 WHY MEASURE CHARM PRODUCTION CROSS SECTIONS?

The theoretical motivation for the introduction of charm in 1970 was to solve a problem in weak interaction theory. Specifically, a fourth quark flavor was introduced to explain the suppression of strangeness changing neutral current interactions such as the decay $K_1 \rightarrow \mu^+\mu^-$ which violated no known or postulated conservation laws.¹ Today the study of charm production in hadron-hadron interactions, both experimentally and theoretically, is aimed primarily toward increasing our understanding of the strong interaction. This change in emphasis implies no irony whatsoever. Rather, it is a direct result of the success of the discovery and interpretation of the new particles in convincing physicists that they were on the right track in understanding the weak and electromagnetic interactions and the structure of hadrons.

Several other developments of the late 1960's and early 1970's were also responsible for the new synthesis. One was the SLAC-MIT electron on nucleon deep inelastic scattering experiments. The dependence of the scattering amplitude only on the four-momentum transfer, known as Bjorken scaling, was interpreted as evidence that the nucleon contained free pointlike constituents which were given the name partons. Another development was the proof of the renormalizability of non-Abelian quantum gauge field theories. A third was the discovery of weak neutral current interactions.²

¹ S.L. Glashow, J. Iliopoulos, and L. Maiani, Phys. Rev. D 2, 1285 (1970).

Prior to these developments doubts lingered over two of the most promising ideas of the previous decade. The weak interaction was well described at low energies by the old four-point interaction theory of Fermi, but that theory was known to be inadequate. Because the theory describes a four-point interaction, the cross section grows linearly with the center of mass energy: $\sigma \sim G^2 s$. Basic considerations of point scattering, however, show that the cross section has a unitarity bound with $\sigma \sim 1/s$. So at $s \sim 1/G^2 = (500 \text{ GeV})^2$ the Fermi theory violates unitarity. An attractive model, with the added feature of unifying the description of the weak and electromagnetic interactions, was developed by Weinberg³ and Salam.⁴ Aside from being a non-Abelian gauge theory, whose renormalizability was still in question, this model also suffered from the limitation that it only applied to leptons. Hadrons were ignored.

The second idea dealt with the structure of hadrons. The dynamics of the strong interaction could only be partially explained through use of several, purely phenomenological concepts, but the spectroscopy of the hadrons had been successfully fit into a model of meson and baryon states made up of appropriate combinations of quarks and antiquarks serving as representations of the Lie group SU(3). It was not clear, however, whether the quarks were corporeal entities whose dynamics could be analyzed or only mathematical constructs.

² The debate over how these pieces fit together just at the time the J/ Ψ was discovered is covered in M.K. Gaillard, B.W. Lee, and J. Rosner, *Rev. Mod. Phys.*, 47, 277 (1975).

³ S. Weinberg, *Phys. Rev. Lett.*, 18, 507 (1967).

⁴ A. Salam in Elementary Particle Theory: Proceedings of 8th Nobel Symposium, edited by N. Svartholm (Stockholm: Almqvist and Wiksell, 1968) p. 367.

The title of the 1970 Glashow-Iliopoulos-Maiani paper was "Weak Interactions with Lepton-Hadron Symmetry." Its aim was to show that any model of the weak interactions applicable to leptons could also be applied to hadrons by treating the quarks in the same manner as the model in question deals with the leptons. Instead of constructing the weak currents among the observed hadrons, they were constructed among the quarks. An integral part of the treatment was the addition of the charm quark to be the partner in a charge current interaction of the strange quark, just as the two different neutrinos were of the two charged leptons.

The excitement over the discovery of the J/ψ is readily understandable. Once the charmonium states and several bare charm states were discovered it became clear that the classification of states under $SU(3)$ symmetry could be extended to $SU(4)$ (albeit greatly perturbed by the large mass of the charm quark). The quark model became almost universally accepted. Quarks were gradually identified with the partons inferred from the scaling experiments, and the Glashow-Weinberg-Salam model became known as the standard model.

The success of a gauge theory in describing the weak interaction and in unifying it with electromagnetism encouraged the attempts to apply similar ideas to the strong interaction. In particular it was what was known as the non-Abelian nature of the models that theorists found most attractive. To understand the central features of these theories it is instructive to write down a model Lagrangian density:

$$L(x) = i\bar{q}_\alpha D_{\alpha\beta} q_\beta - \frac{1}{4} F_{\mu\nu}^a F^{a\mu\nu}$$

The q 's represent the fermion fields, and the F^a represents the field strength tensor of the intermediary gauge bosons, analogous to the photons or QED. This class of Lagrangian density was first studied by Yang and Mills in 1954.⁵ Unlike QED which contains only one gauge boson, a non-Abelian gauge theory requires as many gauge bosons as there are generators of the regular representation of the group under which the fundamental fermions transform, and it must be invariant under transformations of the form:

$$\tilde{A}_\mu(x) = A_\mu^a(x) \frac{T^a}{2} \longrightarrow U(x) \tilde{A}_\mu(x) U^{-1}(x) + \frac{1}{g} \partial_\mu U(x)$$

$$q(x) \longrightarrow U(x)q(x)$$

where the U 's are unitary matrices which can have different values at different points in space-time.⁶ That is what is meant by the term local gauge invariance. In order to insure this property, in addition to the terms in the field strength tensor familiar from QED

$$F_{\mu\nu}^a = \partial_\mu A_\nu^a - \partial_\nu A_\mu^a$$

there is a term

$$gf^{abc} A_\mu^b A_\nu^c$$

where f^{abc} represents the structure constants of the symmetric unitary group in question, and g is the coupling constant. Another way of writing this term is

⁵ C.N. Yang and R. Mills, Phys. Rev. 96, 191 (1954).

⁶ The T matrices represent the algebraic structure of the symmetry group.
 $[T^a, T^b] = if^{abc} T^c$
 For $SU(2)$ they are the Pauli matrices; for $SU(3)$ the Gell-Mann matrices.

$$-ig[\mathcal{K}_\mu, \mathcal{K}_n] .$$

The commutator does not vanish: this is the meaning of non-Abelian. This extra term, a product of the gauge fields and coupling constant, means that the gauge bosons interact among themselves. Unlike the neutral photon, they are charged.

When the fundamental Lagrangian density is recast into its phenomenological form, appealing consequences emerge. For the weak interaction, where the underlying gauge group is SU(2), the self interaction is intimately related to the existence of electrically charged weak bosons that when radiated or absorbed flip the weak isospin (or change the flavor) of the fundamental fermions. The matrix structure does, however, also call for a neutral boson with the consequent neutral current interactions. It was their prediction that was the major triumph of the Weinberg-Salam model.

There are charged and neutral bosons in the theory of the strong interaction as well, but here the most remarkable manifestation of the self interactions among the gauge bosons is asymptotic freedom. At very short distances, or equivalently, at very large momentum transfers, the effective coupling constant of the theory vanishes and the quarks behave as if they were free, that is, in accord with the scaling properties of the deep inelastic scattering experiments. This property of the theory was discovered through the analysis of the renormalization group equation for the Yang-Mills Lagrangian.⁷ Several heuristic explanations of the phenomenon exist, but none are convincing.⁸

⁷ David J Gross and Frank Wilczek, Phys. Rev. Lett., 30, 1343 (1973); H. David Politzer, Phys. Rev. Lett., 30, 1346 (1973).

⁸ The popular explanation of an antiscreening effect due to the radiation by the quarks of some of their charge in the form of gluons fails

The field theoretic description of the strong interaction requires the specification of a degree of freedom analogous to charge or flavor. Throughout the 1960's there was mounting evidence that the quarks had an internal degree of freedom which could take on three values. This extra degree of freedom, labeled color, explained such varied phenomena as the apparent violation of the relationship between spin and statistics in hadron spectroscopy, the missing factor of three in the calculation of the decay rate of the π^0 into two photons, and the large value of R, the ratio of hadron to muon production in e^+e^- annihilation experiments.

The last of these examples illustrates the way different strands converged. The quantity R, which to first order in QED is simply the sum of the squares of the electric charges over all the varieties of quarks, was also central to the acceptance of the quark model. One could see clearly the rise in R beyond the charm threshold indicating that a new degree of freedom was available. Later the anomalously large increase in R provided the first clue for the existence of the τ lepton.⁹

The name color is highly suggestive. It is a hidden degree of freedom; only color singlet states are found in nature. In the case of baryons one can visualize the three quarks, each of a different primary color, combining to form a white or colorless state. By choosing SU(3) with the three representing the three quark colors to be the Lie group in the Yang-Mills Lagrangian and by denoting the eight massless vector gauge bosons as gluons, the glue holding the hadron together, one arrives at quantum-chromodynamics (QCD), the leading candidate for a theo-

to take into account the flavor number dependence of the effect. A more suitable explanation, based on an analogy to magnetism, can be found in F. Wilczek, Ann. Rev. Nucl. and Part. Sci. 32, (to be published).

⁹ Martin Perl in Ann. Rev. of Nucl. and Part. Sci., Vol. 30, edited by J.D. Jackson et al. (Palo Alto: Annual Reviews Inc., 1980) p. 299.

ry describing the strong interaction.

There is a big difference between writing down a Lagrangian which describes unobserved, and possibly unobservable, quarks and making predictions that are experimentally verifiable, even given the expectation that asymptotic freedom will provide a domain where the coupling constant is small enough to make perturbation theory useful. It must also be kept in mind that much of the structure of the contemporary quark model view of hadron physics (including the idea of hadrons composed of valence quarks surrounded by an ever changing sea of quarks, antiquarks, and gluons) stands independent of QCD.

It is in this context, possessing a candidate strong interaction theory but with many questions about the theory and about the nature of hadrons still open, that we list specific reasons for investigating charm production using hadron beams.

Under the assumption that the fragmentation of a charm (or other heavy) quark into an observable hadron does little to alter the energy and momentum of that quark, the observation of charmed state production approximates the observation of interactions at the quark level. The validity of perturbative QCD predictions of strong interaction dynamics, as well as the validity of other models, should be testable based on measurements of charm production. These experiments should include both measurements of total charm production and of charm production as a function of such kinematic variables as center of mass energy, transverse momentum, and rapidity. In this sense measuring charm production is useful in the same way as are experiments which measure single particle production at large transverse momentum or those which measure the properties of QCD jets.

Understanding the spectroscopy of the charmed states is as important as measuring the rate of charm production. Spectroscopy is important both in determining whether all the states predicted by the SU(4) symmetry exist and in making quantitative tests of potential models based on perturbative QCD by measuring the transitions among the states. So far no hadronically produced charm state has ever been detected that has not been previously seen in an e^+e^- interaction. This is mainly a result of the high level of the hadronic background which overshadows charm production by a factor of order one thousand making it hard to detect a state unless the experimenter knows approximately where to look and designs the trigger to act as a filter for it. Nonetheless, experimenters have been using hadron beams with fixed targets¹⁰ to search for states that do not couple to the photon such as the η_c ($J^{PC}=0^{-+}$), and there are plans to take advantage of the ability of hadron storage rings to provide a finely tuned beam of variable energy to search for charmonium states in the near future.¹¹ If the recent measurements of large charm cross sections at the CERN ISR are convincingly confirmed, hadron beams may yet dominate charm spectroscopy.

There are other motivations which do not fit into the oversimplified scheme presented so far. It would be interesting to see whether the K^0 - \bar{K}^0 mixing scheme repeats itself in the D^0 - \bar{D}^0 , providing another laboratory in which to study CP symmetry and its violation.¹² Another suggestion is to exploit the equal semileptonic branching fraction of the

¹⁰ Alfred Mike Halling, Ph.D. thesis, Princeton University, 1982 (unpublished).

¹¹ G. Bassompierre, talk given at XVII Rencontre de Moriond, LAPP-EXP-82-02 (to be published).

¹² Limits on D^0 - \bar{D}^0 mixing have been reported by A. Bodek, *et al.*, U. Rochester report COO-3065-315 (to be published).

charm quark into electrons and muons as a possible source of high energy electron neutrinos for weak interaction experimentation.¹³

More prosaically, understanding the dynamics of charm production should help in discovering and measuring the production of heavier flavor states. Finally, the level of charm production must be understood because it is a background to other interactions. Of most concern at present is the expectation that the W and Z bosons will be discovered through their leptonic decays, and charm (along with beauty) is the principal uncalibrated competing source of high transverse momentum leptons.

1.2 MODELING HADRONIC CHARM PRODUCTION

Because the charm quark has a mass of about 1.5 GeV, a charmed state can only be observed following a collision at relatively high energy. The fundamental question which all theories of charm production must answer is whether the collision creates the charm quark and antiquark or whether they are already present in the sea and are liberated in the collision. It will be shown that these two possibilities imply different distributions in energy and momentum of the charmed quarks emerging from the interaction.

As stated in the last section, the detection of charmed hadrons approximates the detection of the emerging heavy quarks whose kinematic distributions can be predicted by the theory. Unfortunately, the complex structure of both the initial and final state hadrons has so far prevented calculations of charm production cross sections more precise than to within a factor of ten. In fact most models of charm production were created to explain experimental results, and agreement between ex-

¹³ Fermilab proposal 625, W.Y. Lee, spokesman.

periment and theory is generally a result of the tuning of the parameters of the theory. To see why this is the case it is instructive to outline within the framework of QCD how charm production cross sections are estimated.

Several assumptions must be made at the start. The momentum transfer in the charm producing or liberating interactions is high enough so that only the lowest order QCD Feynman diagrams need be considered. The heavy quarks resulting from the interaction will almost always evolve into a pair of hadrons one with charm +1 and the other with charm -1; a bound, hidden charm state, such as the J/ψ , is formed only when the invariant mass of the $c\bar{c}$ pair is below the threshold for DD production. In the fragmentation of the charm quark into hadrons, the interactions required to establish the color neutrality of the final state are dominated by interactions among low energy gluons which do not impart significant momentum to the heavy quarks. Taken together these assumptions are a more precise statement of the underlying belief that observing charmed hadrons is like observing charm quarks. They also imply that predictions can only be made of the total charm cross section and not of the cross sections for the production of particular states.

At a center of mass energy squared s , the total charm production cross section in a collision between hadron A and hadron B can be expressed as:

$$\sigma_{\text{CC}}(s) = \sum_{1,2} \iint dx_1 dx_2 \sigma_{1,2}(s') f^{1a}(x_1, Q^2) f^{2b}(x_2, Q^2) / (x_1 x_2) \quad (1.1)$$

The subscripts 1 and 2 refer to a quark or gluon from hadron A and B respectively. The summation is over all the distinct subprocesses con-

tributing to charm production. The f functions are the probability of finding within each hadron a quark or gluon with the fractional longitudinal momentum x when examined with a probe of momentum transfer Q^2 . $\sigma_{1,2}(s')$ is the square of the QCD matrix element for the subprocess where s' is a function of s , x_1 , and x_2 .

The lowest order QCD processes are illustrated in Figure 1, where q stands for any light (including strange) quark, g represents a gluon, and c denotes a charm quark. They describe both the creation of the charmed pair: $q\bar{q} \rightarrow c\bar{c}$ and $gg \rightarrow c\bar{c}$, and the excitation or liberation of the charm quark: $qc \rightarrow qc$ and $gc \rightarrow gc$.

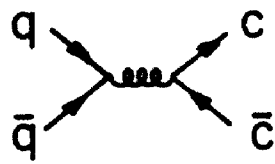
In the case of flavor creation $s' = x_1x_2s$ and the domain of integration is the region where $s' > (2m_c)^2$. Charmonium states are created principally in the subset of that region where $s' < (2m_D)^2$. For the flavor excitation diagrams the relationship between s' and the x_i 's is complicated by the massiveness of the interacting charm quark and may be taken to be $s' = x_1x_2s + m_c^2$.

Without doing any calculations we can extract from Equation (1.1) information on which mechanism dominates charm production. The earliest models¹⁴ ignored the matrix element and tried to describe charm production as a probe of the charmed sea, making estimates based on extrapolations of strangeness production. In terms of Equation (1.1), they concentrated on only f^c . Analysis of these parton density functions based on deep inelastic scattering experiments contradicted this explanation.¹⁵ The inferred charm structure functions were too small to account

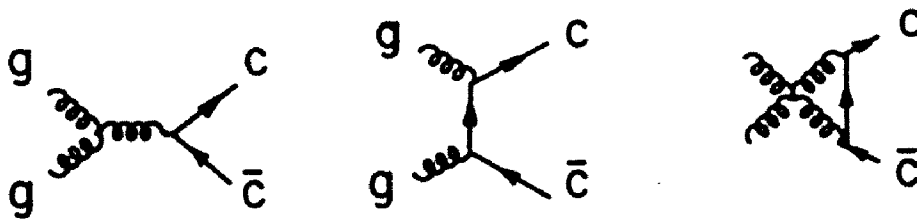
¹⁴ D. Sivers, Nucl. Phys. B106, 95 (1976). (1977); M. Bourquin and J.M. Gaillard, Nucl. Phys. B114, 334 (1976); A. Donnachie and P.V. Landshoff, Nucl. Phys. B112 233 (1976).

¹⁵ The structure functions were determined by A. Buras and K.J.F. Gaemers, Nucl. Phys. B132, 249 (1978); The application to charm was by

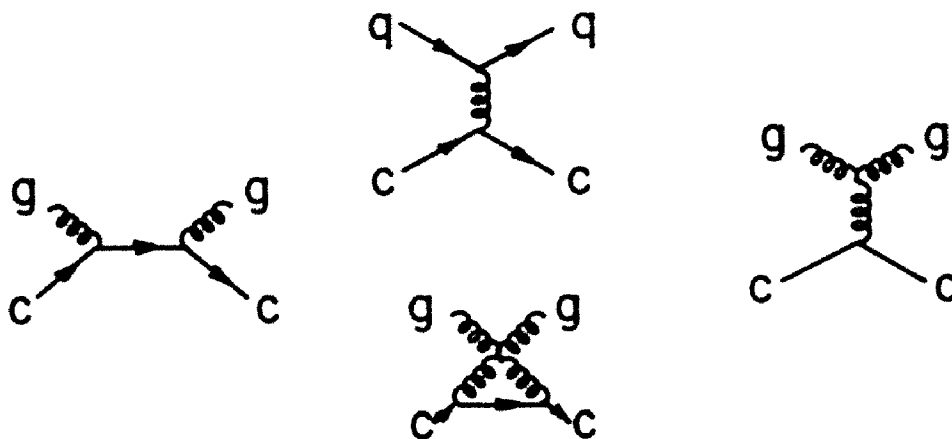
LOWEST ORDER QCD CHARM PRODUCTION PROCESSES



a) quark annihilation



b) gluon fusion



c) quark excitation

Figure 1: Lowest Order QCD Charm Production Processes

for J/ψ and prompt lepton production. This failure led theorists to concentrate on the flavor creation processes and forced the application of QCD.¹⁶

The next question was whether it was light quark annihilation, the QCD analog of the Drell Yan mechanism of lepton pair production in QED, or gluon-gluon fusion which dominated. Again, the answer could be determined without calculating the matrix elements. The observed angular distribution of muon pairs from J/ψ decay contradicts the model of J/ψ production dominated by light quark annihilation.¹⁷ It was also known that half the momentum of a proton was carried by the gluons. This led one group to the conclusion that gluon fusion was the dominant charm production mechanism in proton-nucleon interaction to the exclusion of the others, and that the dominance would increase with the beam energy. In anticipation of future charm measurements they presented the first calculation of the $gg \rightarrow c\bar{c}$ contribution to hadronic charm production.¹⁸

A more direct test of which mechanism dominates would be to compare the ratio of J/ψ production using antiproton or pion beams, which have valence antiquarks, with that using a proton beam. A simple analysis of J/ψ production¹⁹ at the SPS shows that with

B.L. Ioffe, Phys. Rev. Lett., 39, 1589 (1977); and by V.A. Novikov, et al., Annals of Physics, 105, 276 (1977).

¹⁶ One of the relatively early QCD papers, B.L. Combridge, Nucl. Phys. B151, 429 (1979); did stress the excitation diagrams, but since he used the Buras-Gaemers parameterizations, their relative contribution was not large at the energies of the contemporary charm searches.

¹⁷ B.L. Ioffe, op. cit., reference 15.

¹⁸ H.M. Georgi, et al., Annals of Physics, 114, 273 (1978).

¹⁹ J. Badier et al., in Proceedings of the XX International Conference on High Energy Physics, Madison, Wisconsin, 1980, edited by L. Durand and L.G. Pondrom (New York: American Institute of Physics, 1981)

$$R(x) = \frac{(d\sigma/dx)_p}{(d\sigma/dx)_p} = 2.0 \text{ at } x = 0$$

and using structure functions derived from the CDHS experiment, in proton-nucleon interactions gluon fusion accounts for 69 percent of the J/ψ production and in antiproton-nucleon interactions for 35 percent. Thus both production mechanisms contribute significantly. Even before this was made clear, many authors included both mechanisms in their calculations.²⁰

In order to appreciate the differences among the various cross section calculations, one needs to examine the terms in Equation (1.1) in more detail. The computation of the diagrams in Figure 1 are straightforward applications of the QCD Feynman rules, though the summations over the flavor and color indices make them more complicated than their QED counterparts.²¹ The uncertainties arise in choosing what values to use for Λ and n_f in the expression for the strong coupling constant

$$\alpha_s = 12\pi / \left[(32 - n_f) \log(Q^2 / \Lambda^2) \right]$$

and in the choice of the charm quark mass, m_c .

The parton density functions are more difficult to handle. Recall that as Q^2 increases, the effective coupling constant grows smaller, allowing the radiation of ever softer gluons and virtual quark anti-quark pairs, revealing successive layers of hadronic structure. The momentum

p.201.

²⁰ The earliest published calculation of the $q\bar{q} \rightarrow c\bar{c}$ matrix element is J. Babcock, D. Sivers, and S. Wolfram, Phys. Rev. D 18, 162 (1978). Other representative papers include C.E. Carlson and R. Suaya, Phys. Lett. 81B, 329 (1979); R. Winder and C. Michael, Nucl. Phys. B173, 59 (1980); and Y. Afek, C. Leroy, and B. Margolis, Phys. Rev. D 22, 86 (1981).

²¹ For a comprehensive review of QCD see W. Marciano and H. Pagels, Physics Reports, 36C, 137 (1978).

of the hadrons must be partitioned among the ever growing number of partons, subject only to the constraint of total momentum conservation:

$$\frac{d}{dQ^2} \int dx x \left[\sum_i f^i(x, Q^2) \right] = 0.$$

QCD predicts the evolution of the parton densities as Q^2 increases once they are known at some Q_0^2 , but their values as functions of x must be parameterized on the basis of experiments.

The two sorts of experiments from which this information is extracted are deep inelastic lepton-nucleon scattering and (Drell-Yan) lepton pair production in hadron-hadron collisions. Deep inelastic scattering with neutrinos probes the quarks in a nucleon with the weak current; scattering with electrons or muons or measuring lepton pair production in hadronic collisions probes the quarks with the electromagnetic current. By measuring the kinematic distributions of the leptons, one can infer those of the quarks with which they interacted. In either case the gluons are invisible to the probing interaction, and their distribution is assumed to be the complement of what is observed.

In sorting out how much each quark contributes to the total momentum, more assumptions must be made. For a nonstrange, noncharmed hadron, the valence quarks are at any Q^2 all assigned the same momentum fraction. The valence quarks are what is referred to as intrinsic components of the hadrons. That means as Q^2 goes to 0, all the f^i 's vanish except for those representing the valence quarks. Most charm production calculations treat the valence quarks in accord with the traditional eight-fold way, for example the proton is assigned u and d with $\int f^u(x, 0) dx = 2/3$ and $\int f^d(x, 0) dx = 1/3$.

One exception to this consensus is the group proposing the notion of intrinsic charm.²² In order to explain the observation of unexpectedly large charm production cross sections at the CERN ISR with the charmed particles carrying large fractions of the longitudinal momentum, they consider the proton at $Q^2 = 0$ to be a superposition of states such as $|uud\rangle$, $|uudg\rangle$, $|uudd\bar{d}\rangle$, with a component in $|uudc\bar{c}\rangle$ of order two percent. This model, with its very low effective threshold in Q^2 , for charm evolution, has consequences beyond charm production in hadron-hadron interactions. It has been applied to explain the anomalously small scale breaking in recent results in μ -N deep inelastic scattering results of the European Muon Collaboration.²³ It is, however, unsuccessful in explaining the total dimuon cross section measured in the same experiment.²⁴

The quarks in the sea are known as the extrinsic quarks. At very high Q^2 we expect the quark sea to be symmetric in $SU(N)$ where N is the number of flavors. In modeling their momentum distribution, the main complication is in determining at what Q^2 the $SU(N)$ flavor symmetry breaks down. Obviously for Q^2 less than $(2m_p)^2$ there will be no charm quarks in the sea, and the situation is similar for both strangeness and the heavy flavors beyond charm. Those calculations which stress the charm excitation diagrams and which do not rely on intrinsic charm are very sensitive to the way $f^c(x, Q^2)$ turns on. The extrinsic quarks are expected to have only a virtual existence, and therefore have a fractional longitudinal momentum peaking near $x = 0$. The same holds true

²² S.J. Brodsky, P. Hoyer, C. Peterson, and N. Sakai, Phys. Lett. 93B, 451 (1980).

²³ D.P. Roy, Phys. Rev. Lett. 47, 213 (1981).

²⁴ J.J. Aubert *et al.* (European Muon Collaboration) CERN-EP/81-161, 1981 (to be published).

for the hard gluons which convert into charm-anticharm pairs. This is what leads most calculations to predict central production.

One model that challenges this assumption is known as the extrinsic charm model²⁵ which was also invented to explain the ISR data. This model supposes that at $Q^2 = (2m_c)^2$ when the charm quark starts to appear in the sea, the constraint that the constituents remain bound within the hadron implies that the charm anti-charm pairs travel with the same velocity as the valence quarks. Because of their large mass, these quarks carry most of the momentum of the hadron. The charm quarks will then fragment into hadrons at relatively large x . As Q^2 continues to grow, more constituents will be able to share the momentum, and the peak of the fractional longitudinal momentum distribution of the charm quarks will eventually approach $x = 0$. That is, central production will dominate near threshold and at very high energies, but in an intermediate region forward production will dominate.

The most recent calculations use, in addition to the density functions parameterized from experimental data, detailed QCD calculations of their evolution and of the initial and final state interactions using Monte Carlo techniques.²⁶ The initial motivation for this work was to test the extrinsic charm hypothesis, but the techniques are much more widely applicable.

The theoretical understanding of hadronic charm production can be summarized as follows. Present techniques are limited to rough estimates of the total charm production cross section. Individual charmed

²⁵ V. Barger, F. Halzen, and W.Y. Keung, Phys. Rev. D 24, 1428 (1981).

²⁶ R. Odorico, University of Bologna Report IFUB 82/3, 1982 (to be published); P. Mazzanti and S. Wada, University of Bologna Report 82/9, 1982 (to be published).

states cannot be handled separately. QCD charm creation mechanisms are sufficient to explain bound and open charm production at SPS and FNAL energies (excepting the results of one experiment to be described in the next section). Flavor excitation processes are necessary to explain the reported increase in cross section at ISR energies. Future work in this subject must take into more careful account the mechanisms by which a single quark becomes a hadron.

1.3 THE EXPERIMENTAL SITUATION

Although the cross section for the production of open charm is much greater than that of the bound charm states, detecting open charm has been much more difficult. Unlike the J/ψ with its easily observed decays into oppositely charged lepton pairs, decays of open charm states produce hadrons which blend into the large combinatorial background. Six years after the discovery of open charm in e^+e^- interactions,²⁷ the picture of hadronic charm production is still fragmentary.

Three basic experimental techniques are employed. They are measuring the rate of prompt single lepton production in hadron-hadron collisions, visually observing the tracks of particles with lifetimes of several tenths of picoseconds in a bubble chamber, streamer chamber, emulsion, or silicon device, and searching for enhancements in invariant mass distributions of the expected decay products of states containing a charm quark. The contribution of each of these types of our experiments to the current understanding is outlined below.²⁸

²⁷ For a review see Gerson Goldhaber and James E. Wiss in Ann. Rev. of Nucl. and Part. Sci., Vol. 30, edited by J.D. Jackson et al. (Palo Alto: Annual Reviews Inc., 1980) p. 337.

²⁸ I have relied heavily on the following set of reviews: Clemens A. Heusch in Proceedings of Summer Institute on Particle Physics, SLAC, 1981, edited by Anne Mosher (Stanford: SLAC, 1982) p. 195; Francis

Prompt lepton experiments measure charm by detecting the leptons produced in the weak decay of charmed hadrons. At best they only provide indirect information on the charm cross section, for there is no way of telling from what state a particular lepton was emitted or even if its origin was from a charmed parent.

Of most interest are the recent results of several prompt lepton experiments of the beam dump variety. In these experiments a proton or pion beam is focused or dumped on a target that is dense enough and thick enough that the bulk of the hadrons produced in the beam-target interactions will be absorbed within the target. This way most of the leptons that emerge from the target will themselves be the products of decays of short lived states produced in the beam-target interactions, that is they will be produced promptly and not be the decay products of longer lived pions and kaons. Two methods are used to subtract the non-prompt background. The rate of lepton production from pion, kaon, and vector meson decay, multiplied by the acceptance of the experiment for those leptons, is calculated and subtracted from the total detected rate. The other method is to run the experiment with a target of varying density and to determine the prompt lepton rate by extrapolating the measurements to correspond to a target of infinite density and zero thickness. When using the extrapolation method, the production of vector mesons, which are extremely short lived, must still be estimated and subtracted from the total. The agreement between the two subtraction

Muller in Proceedings of the IV Warsaw Symposium on Elementary Particle Physics, edited by Z. Ajduk and K. Doroba (Warsaw: 1981) p. 141; S.L. Olsen, talk given at Second Conference on Forward Collider Physics, Madison Wisconsin, U. of Rochester Report C00 3065 324, 1981 (to be published); and D. Treille in Proceedings of the International Symposium on Lepton and Photon Interactions at High Energies, Bonn, 1981, edited by W. Pfeil (Bonn: University of Bonn, 1981) p. 750.

methods is generally reasonable, but in either case the systematic uncertainties can be comparable to the size of the signal.

When analyzing these experiments, all of the prompt single leptons remaining after the background subtraction are assumed to come from charm. Although the semileptonic branching ratios of the different charmed particles as measured in e^+e^- machines vary greatly, most notably in the charged versus neutral D mesons, and although the relative production rates in hadron beams of the different states have not been measured, an average branching fraction of total charm to leptons of eight percent is commonly used in inferring the charm cross section.

At the Super Proton Synchrotron (SPS) at CERN, three such experiments sit in tandem. They are, starting closest to the dump, the BEBC bubble chamber,²⁹ the CDHS³⁰ iron toroid calorimeter, and the CHARM³¹ fine grain marble calorimeter. These experiments can all run simultaneously. They detect neutrinos produced in a copper dump about 800 meters upstream of the first detector. The results of these experiments are shown in Table 1 taken from the review by Treille. These experiments all seem to favor a central production mechanism for charm with a total cross section for 400 GeV/c incident protons of 10 to 20 microbarns.

Two outstanding problems in the interpretation of these experiments remain. The small anti-neutrino signal (actually consistent with zero in the CDHS experiment) would not be expected if the signal was dominated by symmetric, associated DD production. Also, all three of these experiments give a $n_{\bar{\nu}_\mu}/n_{\nu_\mu}$ ratio of less than unity in contradiction to the

²⁹ Big European Bubble Chamber: Aachen-Bonn-CERN-IC London-Oxford-Saclay Collaboration.

³⁰ CERN, Dortmund, Heidelberg, Saclay, Collaboration.

³¹ CERN-Hamburg-Amsterdam-Rome Moscow Collaboration.

TABLE 1
CERN Beam Dump Results

$\sigma(pp \rightarrow DDX)$
for $E (d\sigma/dp^2) \sim (1 - |x|)^4 \exp(-2p_t)$,
a .08 branching fraction, and a linear A dependence

CHARM	BEBC	CDHS
$18 \pm 6 \mu\text{b}$	$17 \pm 4 \mu\text{b}$	$\sim 10 \mu\text{b}$
with $\gamma_e/\bar{\gamma}_e = 1$		with $\frac{\gamma_e}{\bar{\gamma}_e} = \frac{\gamma_\mu}{\bar{\gamma}_\mu} = 2.3$

equal semileptonic branching fractions to electron and muons of the charm quark.

At Fermilab the CCFRS³² experiment estimates the charm cross section by measuring prompt single muons. This experiment used 350 GeV/c protons and 278 GeV/c pions. They see no evidence for the diffractive production of charm or for intrinsic charm at anywhere near the one percent level predicted by its proponents.³³ Based on a central production model they find a total cross section of

$$\sigma(c\bar{c}) = 22 \pm 9 \mu\text{barns/nucleon}$$

and $\sigma(D\bar{D}) = 16 \pm 4 \mu\text{barns/nucleon}$.

Preliminary results from Fermilab E613,³⁴ an experiment measuring prompt neutrinos from the interaction of 400 GeV/c protons on tungsten find

$$\sigma(D\bar{D}) = 17.2 \pm 2.2(\text{stat.}) \pm 3.4(\text{sys}) \mu\text{barns.}$$

³² Cal. Tech., Chicago, Fermilab, Rochester, Stanford Collaboration.

³³ A. Bodek *et al.*, U. of Rochester Report C00 3065 307, 1982 (to be published).

³⁴ R.C. Ball *et al.*, U. of Massachusetts Report UM HE 81-48, 1981 (to be published).

Unlike CDHS, they find an antineutrino flux 2.9 standard deviations from zero and a $\bar{\nu}/\nu$ ratio of $.8 \pm .35$.

Broadly speaking, the results from Fermilab are in agreement with the earlier results from CERN both in terms of total cross section and production mechanism. One other positive result is from Serpukhov.³⁵ Interpreting the data using the same assumptions as the CERN experiments,³⁶ they measure a cross section

$$\sigma(DD) = 7.5 \pm 6 \text{ } \mu\text{barns/nucleon}$$

for 70 GeV/c protons. No positive prompt muon signals have been found at lower energies.³⁷

Measuring the decay length is at present the only way of determining the lifetimes of short lived particles, and it is this task that the visual techniques have principally addressed. Vertex observation techniques must be able to resolve tracks at the level of tens of microns in order to pick out the decays of charmed particles which have lifetimes of order 10^{-13} seconds.³⁸

The major drawback in using such devices to measure total charm cross sections is that because path length is the only means of selecting charm candidates, the sample is biased toward longer lived events. The low beam intensities necessary for clean, easily readable vertex pictures means that such experiments have relatively slow data collection rates. The lack of particle identification and the invisibility of neu-

³⁵ A.E. Asratyan *et al.*, Phys. Lett. 79B, 497 (1978).

³⁶ W. Geist, talk given at EPS International Conference on High Energy Physics, Geneva, 1979, CERN/EP 79-78 (1979).

³⁷ John LeSocco in HEP-80, Madison, p. 252.

³⁸ These techniques are reviewed along with predictions of future developments in G. Bellini *et al.*, Physics Reports 83C, 1 (1982).

trials within the detector makes it difficult to determine the identity of the parent state. Nonetheless, when one of these devices is coupled with an electronic spectrometer to create what is called a hybrid system, a more complete event reconstruction is possible than in any other sort of high energy physics experiment.

One example of the utility of this marriage is the small bubble chamber LEBC coupled with the European Hybrid Spectrometer. Based on exposures to both protons and pions at a momentum of 360 GeV/c, they measure a cross section in their kinematic region of acceptance of

$$\sigma(D^\pm)_{x>0} = 12.5 \pm 5 \mu\text{barn}$$

where the event pattern follows a central production mechanism.³⁹

The conceptually most straightforward, but practically most difficult technique is bump hunting: looking for enhancements in invariant mass distributions of the expected decay products of charmed states. It seems that in order for this type of experiment to succeed, there must be an extra requirement in the trigger beyond what is needed to detect the particles in the mass plot. It can be the requirement of an extra lepton in the trigger which is assumed to come from the partner particle in an associated production mechanism, or it can be the exploitation of some other kinematic feature of the system being studied.

So far no direct open charm signal has been observed at AGS energies. The most stringent upper limit has been set at the Brookhaven Multiparticle Spectrometer in an experiment using a 16 GeV/c π^- beam incident on a hydrogen target.⁴⁰ They report an upper limit at 95 percent confidence

³⁹ Quoted from Treille, these results were submitted to the EPS International Conference on High Energy Physics, Lisbon, 1981.

⁴⁰ S.V. Chung *et al.*, Phys. Rev. Lett. 48, 785 (1982).

level of 2.4 nanobarns/nucleon cross section for the inclusive production of D^{*-} . For the exclusive process

$$\pi^- p \rightarrow D^{*-} \Lambda_c^+$$

their upper limit is 1.3 nanobarns/nucleon. This result corresponds to a total charm cross section of 600 microbarns. The absence of a signal at this sensitivity is not surprising if one assumes that the ratio of bound to open charm production is only weakly dependent on energy, for the J/ψ production cross section⁴¹ rises three orders of magnitude between center of mass energies 6 GeV and 20 GeV.

Aside from the Princeton-Saclay-Torino-BNL collaboration whose work will be described in this thesis, two groups have reported measurements of hadronic charm production in fixed target experiments. A group using the Chicago Cyclotron Magnet Facility at Fermilab has reported a signal for the observation of charged D mesons.⁴² A 217 GeV/c negative pion beam was incident on a hydrogen target. The trigger required the detection of a proton recoiling against a system of mass between 3.0 and 6.5 GeV headed forward through the spectrometer and of a single muon which was supposed to have come from the semileptonic decay of associatedly produced D mesons. They found about 50 events above the background in the $K^+\pi^-\pi^- + K^-\pi^+\pi^+$ invariant mass distributions with the distribution in Feynman x peaking around $x = 0.4$, consistent with a diffractive model of charm production. Based on such a model they report

$$\sigma(D^+D^-) = 6-10 \pm 4 \text{ } \mu\text{barns/nucleon.}$$

⁴¹ J.G. Branson, *et al.*, Phys. Rev. Lett. 38, 1331 (1977).

⁴² L.J. Koester *et al.* in HEP-80, Madison, p.190.

This experiment is relatively insensitive to neutral D mesons because of their low semileptonic branching fraction. That means the reported result does not include the contribution of $D^0\bar{D}^0$, D^+D^0 , and D^0D^- pairs. Including all these combinations yields a charm production cross section of about 40 μbarns , in poor agreement with both the beam dump consensus and the other bump hunts.

The ACCMOR collaboration⁴³ used a large aperture magnetic spectrometer at the CERN SPS. There was an unseparated 175 and 250 GeV/c π^- beam incident on a beryllium target. The trigger required an electron which, as in the last experiment described, was assumed to come from a semileptonic D decay, and the spectrometer was designed to reconstruct the decay of its partner. The trigger was designed so that it suppressed the signal by about a factor of 10 (the average semileptonic branching fraction) while suppressing the background by a factor of 100. They observed an enhancement when looking for D^0 's resulting from the decay

$D^{*+} \rightarrow D^0 \pi^+$, $D^0 \rightarrow K^- \pi^+$ (and its complex conjugate interaction).⁴⁴

A hint of a signal at the D^0 was also observed in the uncut $K \pi$ distributions. Assuming a central production mechanism they infer a cross section of

$$\sigma(D^{*+}+X) + \sigma(D^{*-}+X) = 9-10 \pm 3 \mu\text{barns/nucleon},$$

and a $\sigma(DD) = 13-18 \pm 5 \mu\text{barns/nucleon}$.

⁴³ Amsterdam, Bristol, CERN, Cracow, Munich, Rutherford. C. Daum *et al.*, paper contributed to EPS International Conference on High Energy Physics, Lisbon, 1981.

⁴⁴ The details of this method of analysis will be described in connection with our experiment.

Four groups working at the CERN Intersecting Storage Rings have reported observations of charmed states as enhancements in invariant mass distributions.⁴⁵ Although the results of the various experiments vary widely, with that of no single experiment being overwhelming in terms of statistical significance of the signal or of mass or width definition, a consensus is emerging that the total open charm cross section is of the order of a millibarn. That corresponds to a rise in cross section over the fixed target experiments of a factor of fifty with a rise in center of mass energy of a factor of three. Such a steep increase is not expected so far from the charm anti-charm quark pair production threshold and is unparalleled in the bound charm cross section which starts to plateau at around $s^{1/2} = 30$ GeV. Another striking feature of the data is the copious production of charmed baryons principally in the forward (large x_p) direction in addition to the expected centrally produced DD pairs. It was both the size and x distribution of the charmed particles that motivated the intrinsic charm model.

There is cause, however, for skepticism in accepting these measurements at face value. Cross section estimates for total charm based on observations over limited kinematic regions are highly model dependent. More pertinent to this set of experiments is how tricky calculations of sensitivity can become when cuts that have no strong physical motivation a priori are applied to the data solely with the intent of enhancing the signal. Two examples should illustrate the point.

The CCHK experiment in searching for the decay

⁴⁵ They are the Aachen-CERN-Harvard-Munich-Northwestern-Riverside Collaboration, the UCLA-Saclay Collaboration, the CERN-College de France-Heidelberg-Karlsruhe Collaboration, and the Bologna-CERN-Frascati Collaboration. The most complete summary of their results is contained in the review by Housch.

$$D^+ \rightarrow K^- \pi^+ \pi^+$$

introduced a requirement that the $K^- \pi^+$ have a mass consistent with that of the $K^*(890)$.⁴⁶ Only after that out did an enhancement appear, yet the Dalitz plot for D^+ decay is flat.⁴⁷ Measured branching fractions notwithstanding, in calculating the cross section the experimenters assumed that there is a 60 percent K^{*0} contribution to D^+ decay. A completely flat Dalitz plot would suggest that the enhancement was fortuitous; a small but real component, k , in K^{*0} would imply a cross section larger by a factor of $.6/k$.

More recently the BCF collaboration measured DD^0 pairs at the Split Field Magnet facility.⁴⁸ The D was tagged through its decay

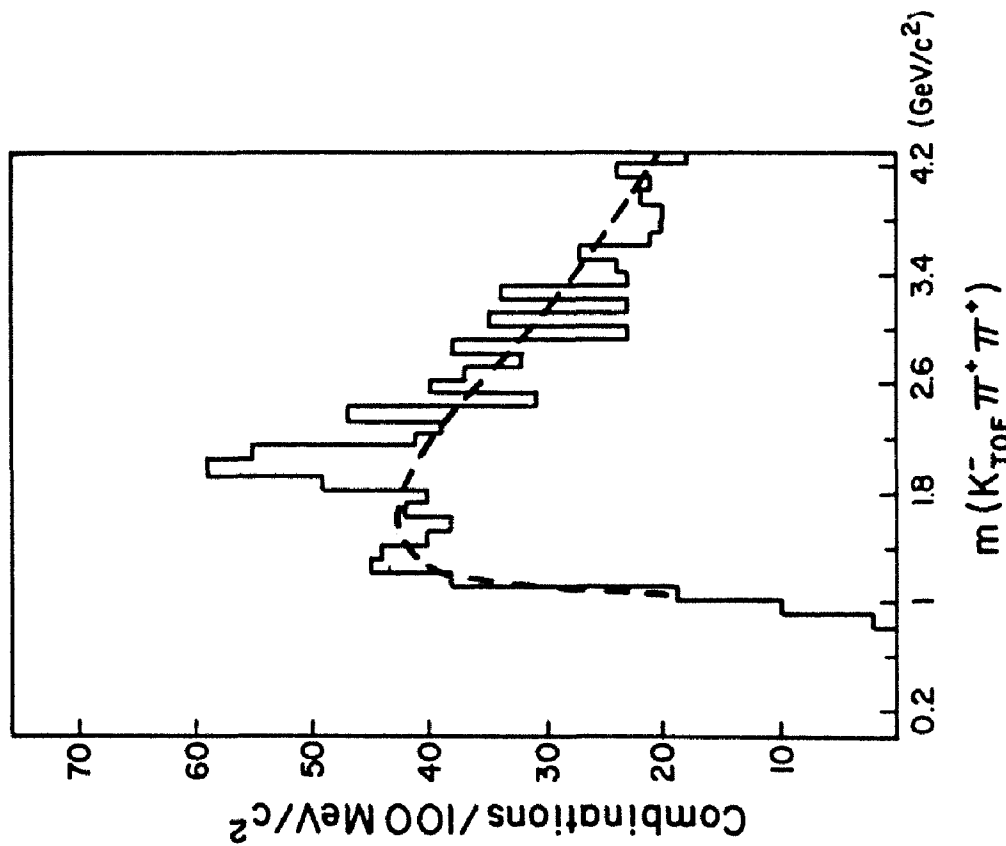
$$D \rightarrow e^- K^+ + \text{anything.}$$

The value used for this branching fraction of 4.3 percent has never been measured, and its estimation involved averaging over several channels. The $K^- \pi^+$ invariant mass distribution was studied. Because all hadron identification was done by time of flight, a cut had to be made on x_{F} of the pion to avoid contamination from fast forward "leading" protons. The original mass distribution shows a peak near the D^0 mass. It was subsequently enhanced beyond the five standard deviation level by the imposition of a transverse momentum cut $p_{\text{T}}(K^- \pi^+) > 0.7 \text{ GeV}/c$. (See Figure 2.)

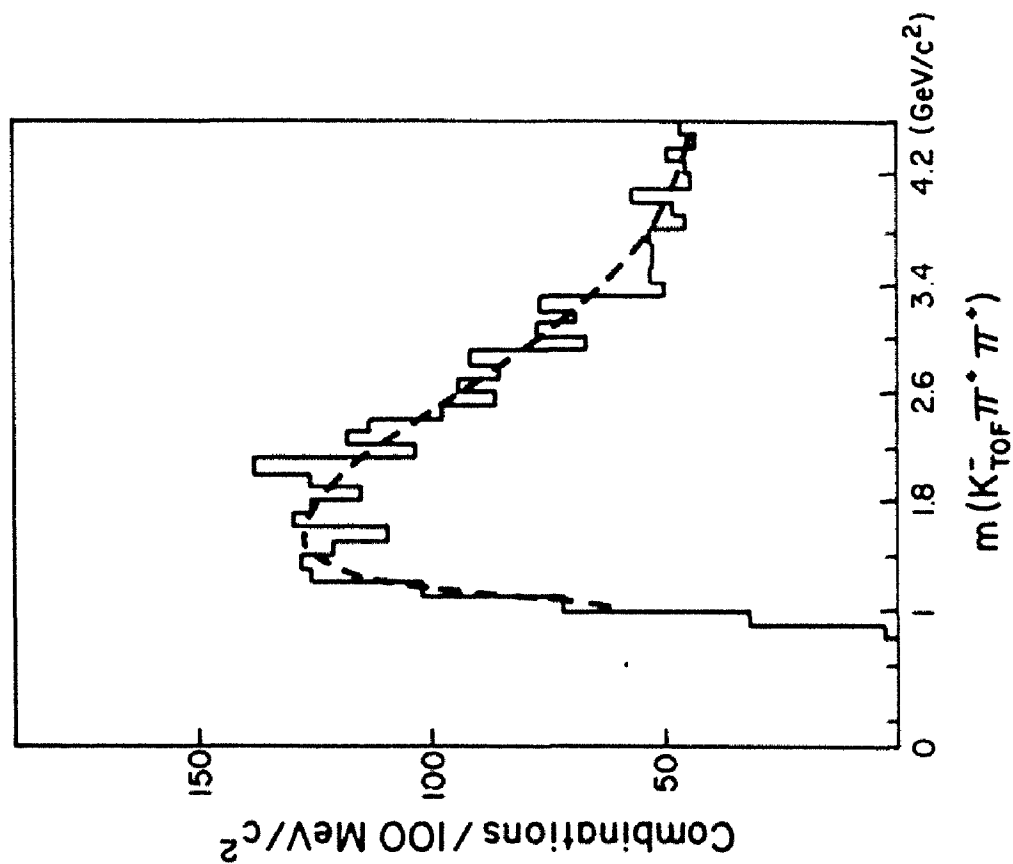
⁴⁶ W. M. Geist in Proceedings of Summer Institute on Particle Physics: Quantum Chromodynamics, SLAC, 1979, edited by Anne Mosher (Stanford: SLAC, 1980) p. 314.

⁴⁷ M. S. Witherell in Proceedings of the Sixth International Conference on Experimental Meson Spectroscopy, BNL, 1980, edited by S.U. Chung and S.J. Lindenbaum (New York: American Institute of Physics, 1981) p. 285.

⁴⁸ M. Basile, et al., CERN-EP/81-73 (to be published).



(b) with p_t cut



(a) without p_t cut

Figure 2: BCF Collaboration Mass Plots

Here, although the presence of the signal is clear, the effect of all the cuts, especially the final one, on the sensitivity is quite hard to estimate.

Another source of confusion arises in comparing these charm cross sections with the results of ISR prompt lepton experiments. Several measurements of the e/π ratio at a p_t of order 1 GeV give a result of about 1 to 2×10^{-4} .⁴⁹ Attributing all of these electrons to charm yields a total charm production of order 100 microbarns. That is, the prompt electron experiments imply a cross section at least an order of magnitude smaller than the mass peak experiments measure. A final complication in the interpretation of these experiments is the possibility that some of the reported charm signals are in fact excited hyperon states which have the same decay signatures as charmed particles.

The need for further work in reliably determining the size and shape of all heavy flavor production is underscored by the controversy surrounding the reported observation of a beautiful baryon.⁵⁰ The BCF collaboration claims the observation, while the ACDHPW collaboration also working at the Split Field Magnet using basically the same apparatus report a null result. The two groups have been analyzing each other's data hoping to find the source of the discrepancy.⁵¹ What has been learned from this exercise so far is that scientific enterprise can still leave room for partisanship.

⁴⁹ P. Perez *et al.* Phys. Lett. 112B, 260 (1982); M. Basile *et al.*, CERN-EP/81-92, 1981 (to be published); F.W. Busser *et al.*, Nucl. Phys. B113, 189 (1976).

⁵⁰ A. Zichichi, CERN EP/82-30, 1982 (to be published).

⁵¹ M. Basile *et al.*, CERN-EP/81-150, 1981 (to be published); D. Drijard *et al.*, CERN-EP/82-31, 1982.

1.4 THIS EXPERIMENT

The experiment described in this thesis was designed to measure charm production by observing the interactions

$$\pi^- N \rightarrow D^{*+} X, D^{*+} \rightarrow D^0 \pi^+, D^0 \rightarrow K^- \pi^+ \text{ and}$$

$$\pi^- N \rightarrow D^{*-} X, D^{*-} \rightarrow \bar{D}^0 \pi^-, \bar{D}^0 \rightarrow K^+ \pi^- .$$

The D^{*+} and the D^0 have charm +1 with valence quarks $c\bar{d}$ and $c\bar{u}$ respectively. The rationale for choosing this interaction was to exploit the small mass difference, $145.3 \pm .4$ MeV, between the D^{*+} and the D^0 . In the zero momentum frame of reference there is only 5.7 MeV of kinetic energy available in the D^0 decay. When boosted back to the lab frame the pion momentum is relatively low:

$$p_\pi \simeq (m_\pi/m_D) p_D .$$

The measured branching fraction for this decay mode is 60 percent. Requiring a slow pion in the trigger in coincidence with a $K \pi$ pair is therefore a promising way of suppressing the background relative to the signal. The small mass difference also implies that once beyond threshold the excited vector states will be produced as copiously as the pseudoscalar ground states, and even more so if the relative production rates follow $2J+1$ weighting.

The experiment took place at the Fermi National Accelerator Laboratory with participants from Princeton University, CEN Saclay, INFN Torino, and Brookhaven National Laboratory. Two sets of data were taken, the first in summer-fall 1979 with a beam momentum of 200 GeV/c, the other in December, 1980 at 250 GeV/c. The results of the 200 GeV/c running, which have already been reported,⁵² are shown in Figure 3. With a total integrated flux of 9×10^{12} pions and assuming a central production

⁵² V.L. Fitch, et al. Phys. Rev. Lett. 46, 761 (1981).

mechanism

$$E \frac{d^3\sigma}{dx dp_t^2} = A(1 - |x|)^2 \exp(1.1 p_t^2)$$

we found a cross section

$$\sigma(D^*) = 1/2 [\sigma(D^{*+}) + \sigma(D^{*-})] = 4.2 \pm 1.4 \text{ } \mu\text{barns.}$$

The corresponding differential cross sections, the calculation of which is not model dependent, are

$$d\sigma/dy = 1.6 \pm 0.5 \text{ } \mu\text{barn}$$

$$\text{and } d\sigma/dx = 1.1 \pm 0.4 \text{ } \mu\text{barn.}$$

The results of the 250 GeV/c running will be presented following a description of the apparatus and the analysis procedures.

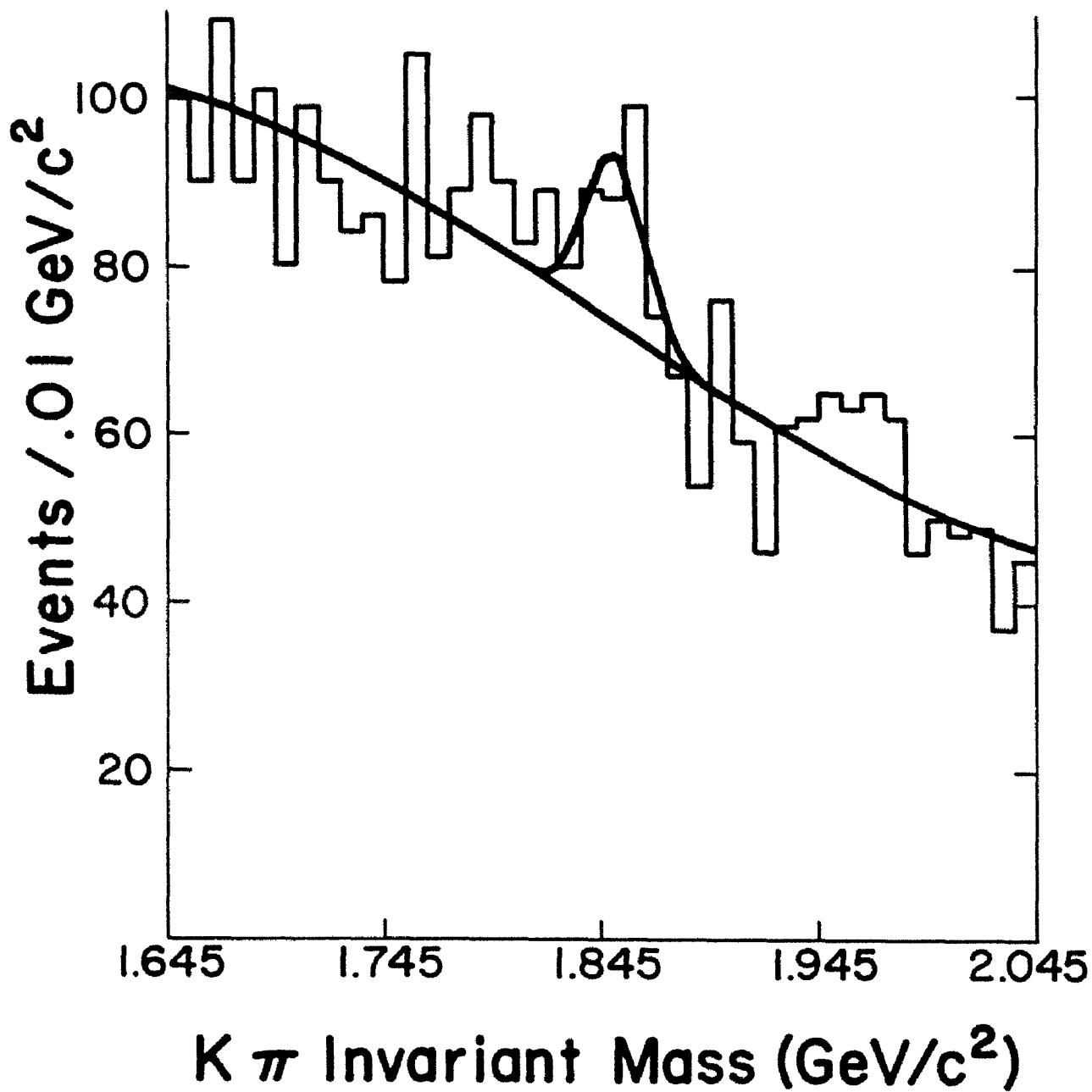
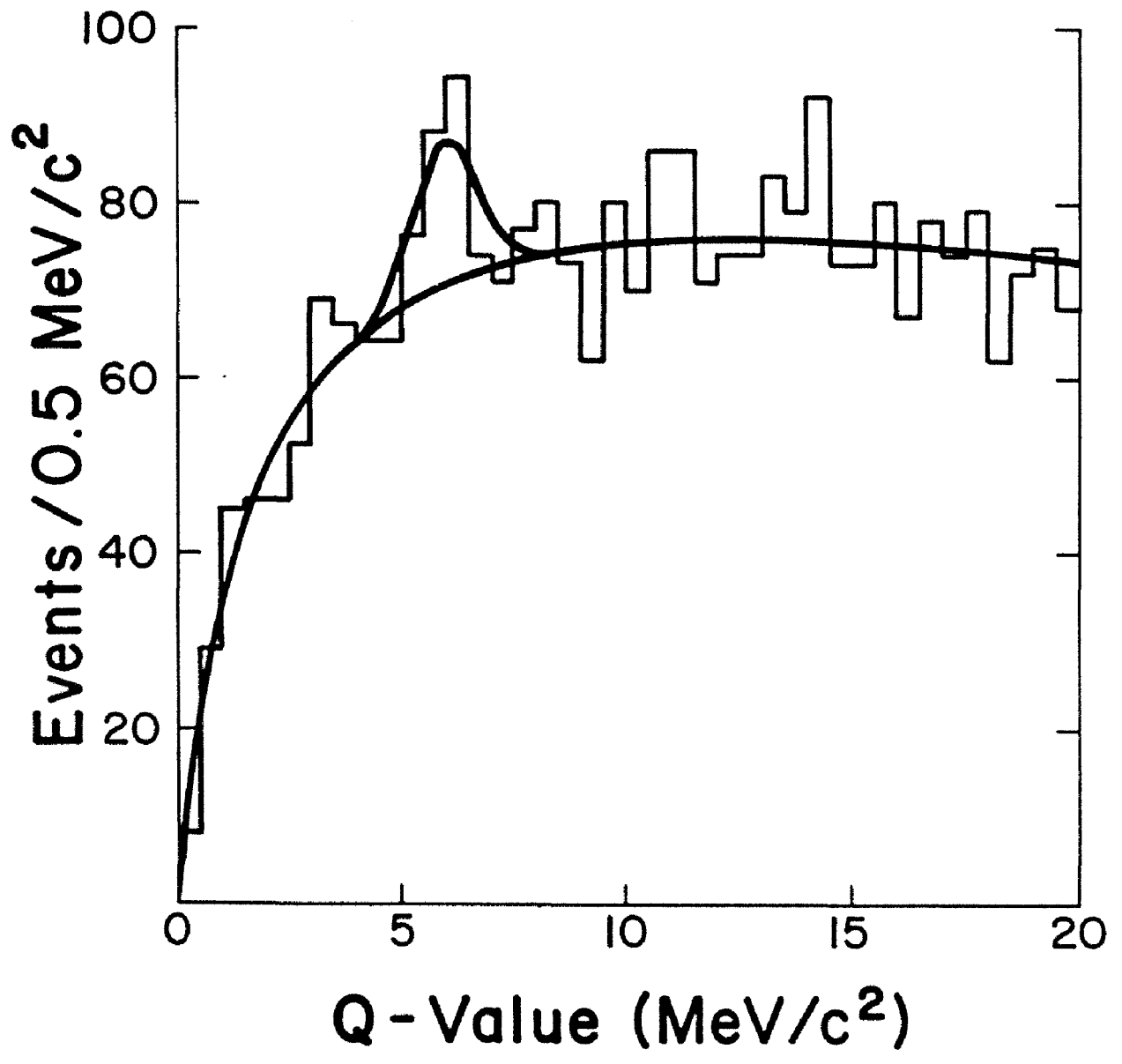


Figure 3: Mass Plots from the 200 GeV/c Run



Chapter II APPARATUS

2.1 OVERVIEW OF THE SPECTROMETER

The four-arm Princeton-Saclay spectrometer was designed to detect all three products of the $D^* \rightarrow \pi^+ D^0$, $D^* \rightarrow K^- \pi^+$ (and its charge conjugate) interaction, with maximum acceptance near Feynman $x = 0$. Between the 200 GeV/c running period and the 250 GeV/c running period several modifications were made to the apparatus. The aim of the modifications was twofold: to increase the rate at which data could be taken and to improve the mass resolution.⁵³ The various components of the apparatus, with an emphasis on the modifications introduced for the second run, will be described following an overview of the spectrometer.

The layout of the apparatus is shown in Figure 4. Just downstream of the segmented beryllium target, a wide aperture magnet, which had previously been named Henry Higgins, delivers 420 MeV/c momentum in the vertical direction. Particles of 1 to 3 GeV/c momentum, such as the cascade pion from the D^* decay, are bent up or down into one of the two slow pion spectrometer arms. The π and K from the D^* decay are detected in the double arm forward spectrometer. All four arms used plastic scintillator hodoscopes for triggering and drift chambers for tracking. Each forward arm was further equipped with two Cerenkov counters for particle identification, and a BM109 magnet with a transverse momentum kick of approximately 650 MeV/c, for momentum analysis. Downstream of the last set of drift chambers was a muon filter which consisted of

⁵³ For a description of details of the apparatus not described here see Steven S. Sherman, Ph.D. thesis, Princeton University, 1980 (unpublished).

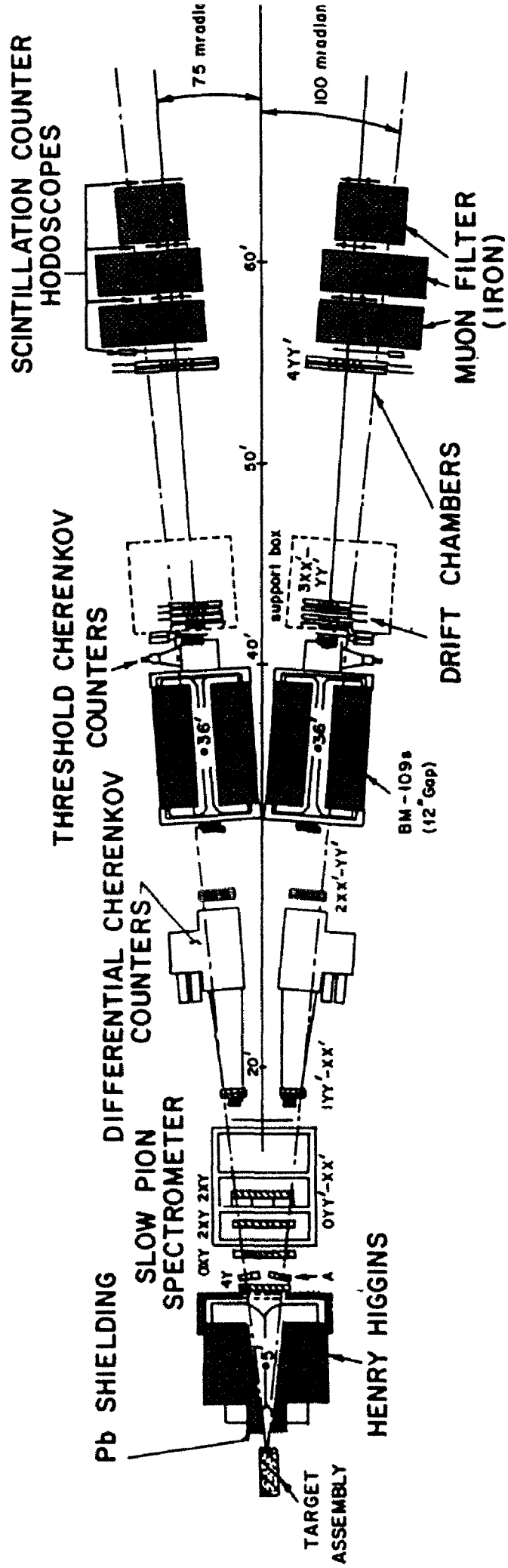
three 3 foot segments of steel interlaced with hodoscopes. Detection of muon pairs enabled us to use the J/ψ as a calibration signal for both beam flux and mass scale.

In the hope that the charm production cross section rises faster with energy than does the hadronic background, we elected to repeat the experiment at 250 GeV/c, the highest beam momentum at which we could be supplied with enough incident beam flux to saturate our data taking capability. For an incident pion beam momentum of 250 GeV/c, the opening angle for a D^0 decay occurring perpendicular to the beam axis in its center of mass frame of reference is 161 milliradians with the pion traveling at an angle of 86 milliradians to the beam. The two fast arms had an opening angle of 150 milliradians symmetric about the beam axis. Having the opening angle of the spectrometer smaller than the decay opening angle makes the acceptance of the spectrometer peak slightly forward of $x = 0$. This was done deliberately, because it also served to boost the average momentum of an accepted product of a D^0 decay from 11 to 12 GeV thereby increasing the fraction of events in which a definite particle identification could be made.

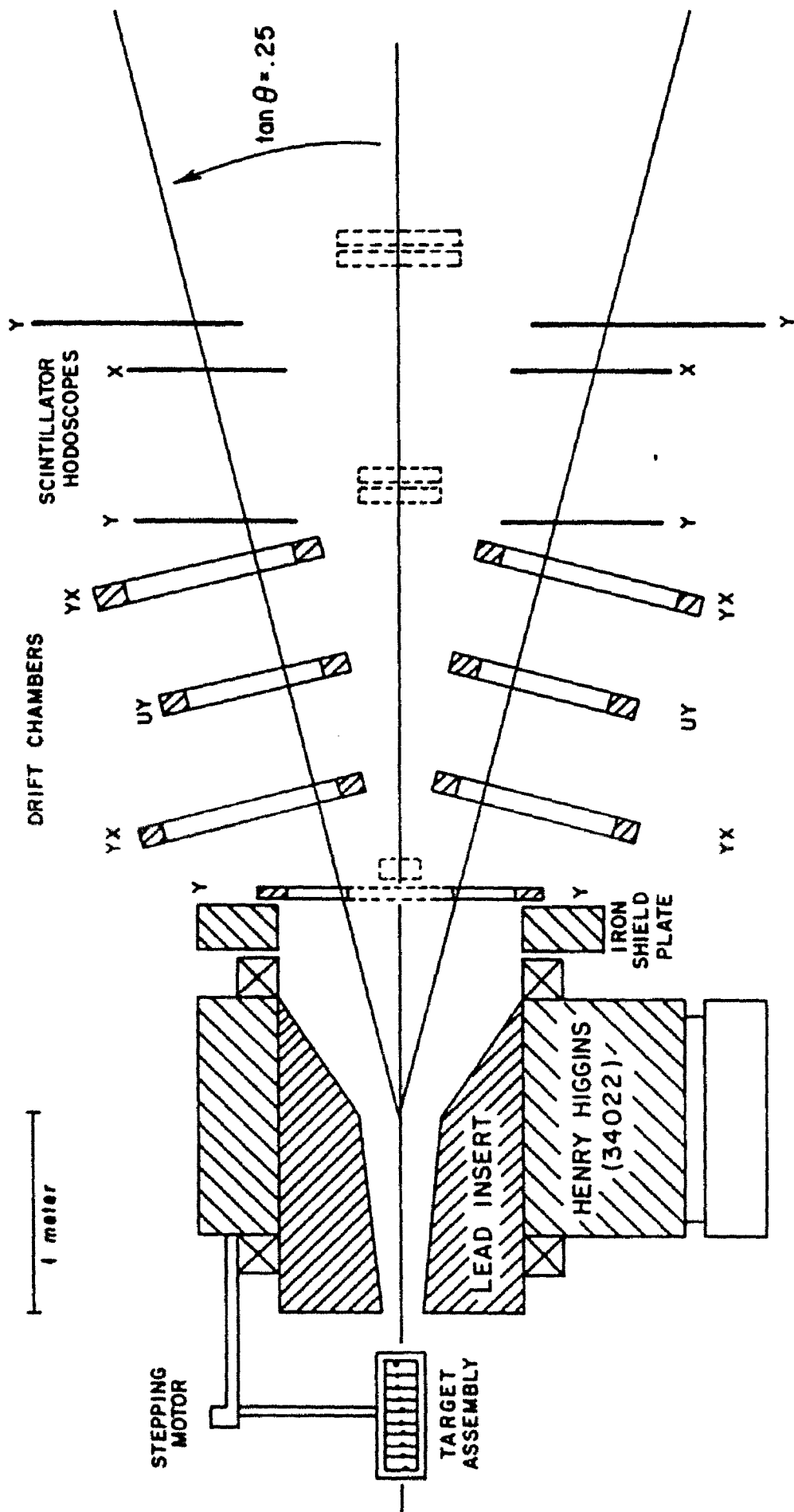
In order to calculate the geometric acceptance of the apparatus, it was simulated by a Monte Carlo program with the D^0 being generated according to the distribution:⁵⁴

$$\frac{d^3N}{dx dp_t^2} \propto (1 - |x|)^3 \exp(1.1 p_t^2)$$

⁵⁴ The x dependence assumes central production in accord with a simple power law. The p_t dependence, when expressed in terms $d\sigma/dp_t^2 \propto \exp(-\beta p_t^2)$, gives a value for $\beta = 1.9$, corresponding to the p_t dependence of J/ψ production as measured in reference 41.



(a) Forward Spectrometer Arms



(b) Slow Pion Spectrometer

Figure 4: Layout of the Spectrometers

The acceptance of the fast arms as a function of these variables is shown in Figure 5. Note that over the narrow range of our acceptance, there is actually negligible difference between a $(1-|x|)^3$ distribution and one that is flat, so that the model dependence is easily factored out of our acceptance and cross section calculations.

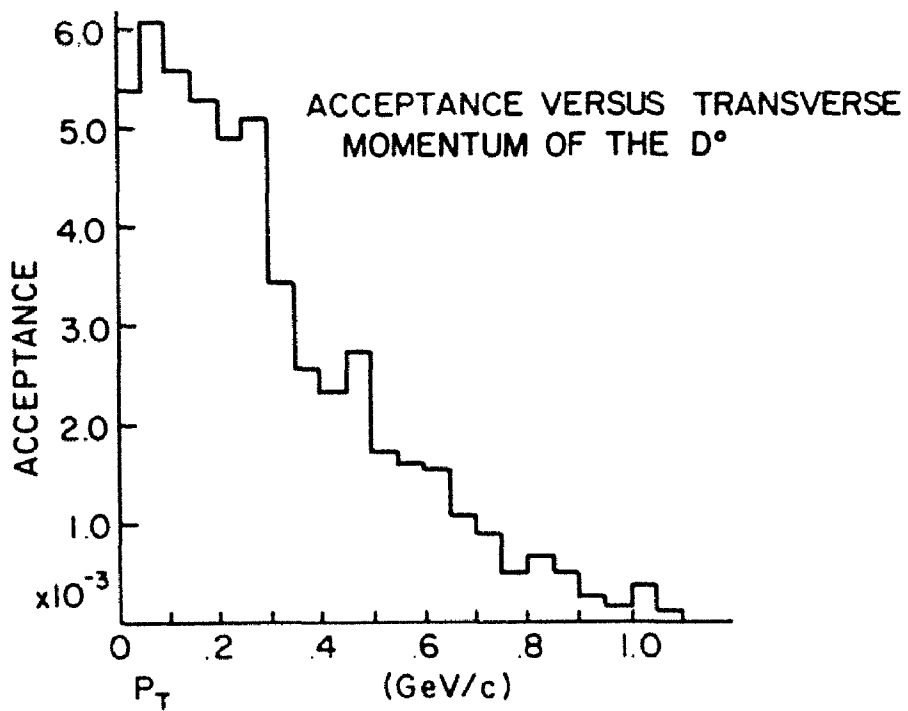
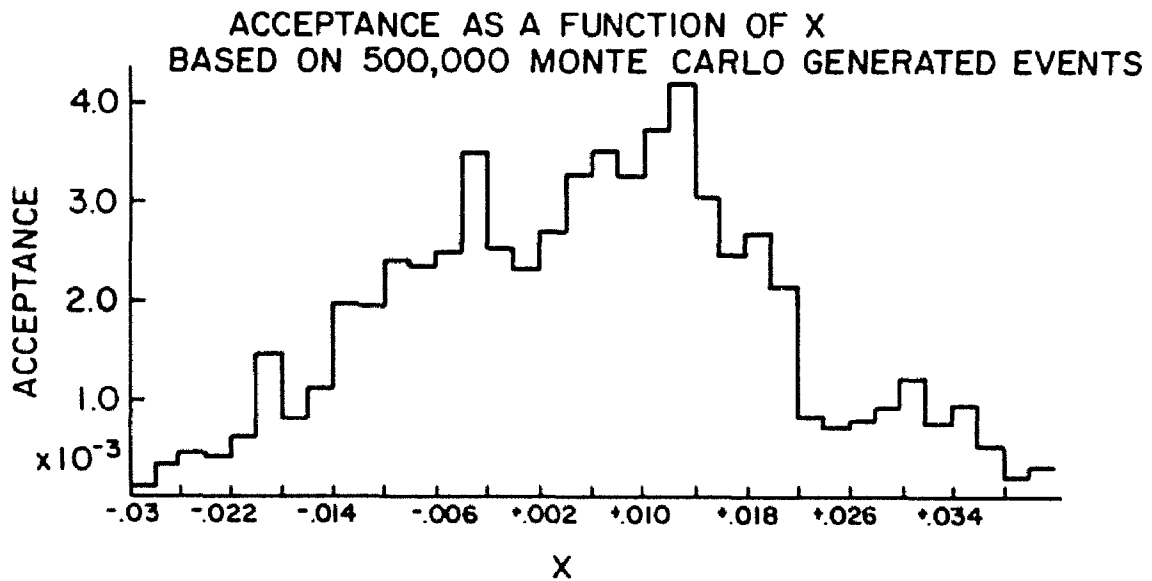


Figure 5: Geometric Acceptance of the Spectrometers

2.2 BEAM

The experiment was run in the high intensity laboratory of the Fermilab Proton-West beam line. The beam was an unseparated negatively charged beam of 250 GeV/c momentum, with a composition of 96 percent pions, 3.6 percent kaons, and 0.4 percent antiprotons.⁵⁵ The beam particles were not identified in this experiment and were all considered to be pions. The beam was produced by the interaction of 400 GeV protons, extracted from the main ring, with a one foot long beryllium target. A secondary emission monitor (SEM) placed upstream of the production target measured the primary proton intensity, and an ionization chamber just upstream of our spectrometer monitored the pion beam intensity. To achieve our desired flux of 1.1×10^8 pions per spill, we required 2.5×10^{12} protons. The ratio of pions to incident protons was highly sensitive to the targeting of the primary beam.

To a large extent we were able to compensate for fluctuations in proton intensity by varying the aperture of the momentum slit through which the pion beam was focused just after its first analyzing bend. The full opening corresponds to a momentum bite of ± 10 percent. On the average we ran with the momentum slit open to 75 percent of the full 3 inch aperture.

After passing through the momentum slit, the beam was transported to the experimental hall and focused on our target.⁵⁶ The beam tune was designed to minimize the horizontal spot width, but to leave the vertical spot wide enough so that each piece of the segmented target would inter-

⁵⁵ Nikos Giorkaris, Ph.D. thesis, University of Chicago, 1981 (unpublished). I interpolated between values in his table 3. No group, in fact, has directly measured the composition of this beam.

⁵⁶ Design of the beam line is described in B. Cox *et al.*, "P-West High Intensity Secondary Beam Area Design Report," March, 1977.

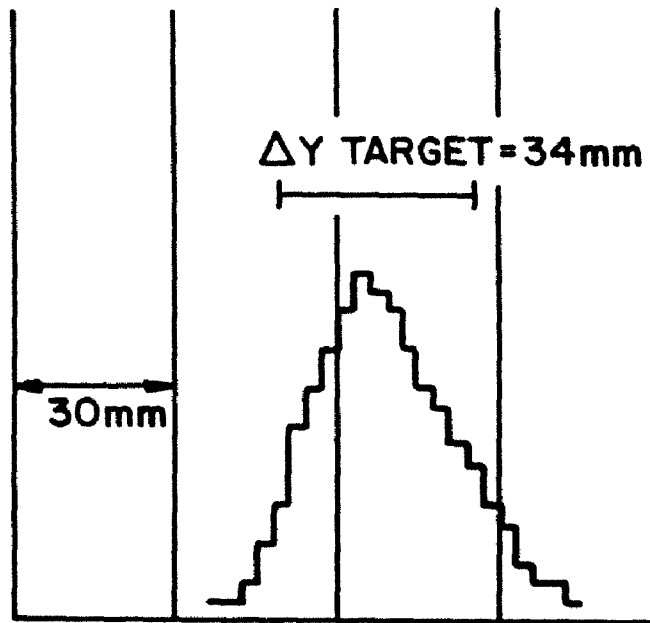
cept a significant amount of beam. The full width at half maximum at the target was 18 and 32 millimeters in the horizontal and vertical respectively. Figure 6 shows the beam profile at the final segmented wire chamber. The defocusing in the vertical represented a loss of about 15 percent in targeting efficiency.

Of critical importance to the performance of our apparatus was the time structure of the beam which deviated greatly from the ideal of a uniform intensity over the one second of slow spill. Because the synchrotron accelerates protons in pulsed bunches, the particles appear in one nanosecond wide "buckets" separated by 18.6 nanosecond intervals. Occasionally a bucket would contain several times its average share of particles causing an instantaneous burst in the number of pions interacting in our target, during which our drift chambers would be swamped with particles and our trigger had to be disabled.

The main source of intensity fluctuations was not these individual superbuckets, but rather a structure in the spill at the fundamental and first few harmonics of 60 Hz due to pickup from alternating current powered devices both in the main ring and along our beam line. This modulation, easily visible in the photograph in Figure 7, caused intensity fluctuations that mimicked the superbuckets, but which were insensitive to the techniques developed by the main ring operators to distribute evenly the particles among the buckets. The figure also shows the commonly occurring intensity spike at the beginning of extraction. To avoid the problems that accompany such an intensity burst, we delayed opening the spill gate that enabled the trigger until 6 milliseconds after extraction had commenced.

BEAM PROFILE

VERTICAL SPOT



HORIZONTAL SPOT

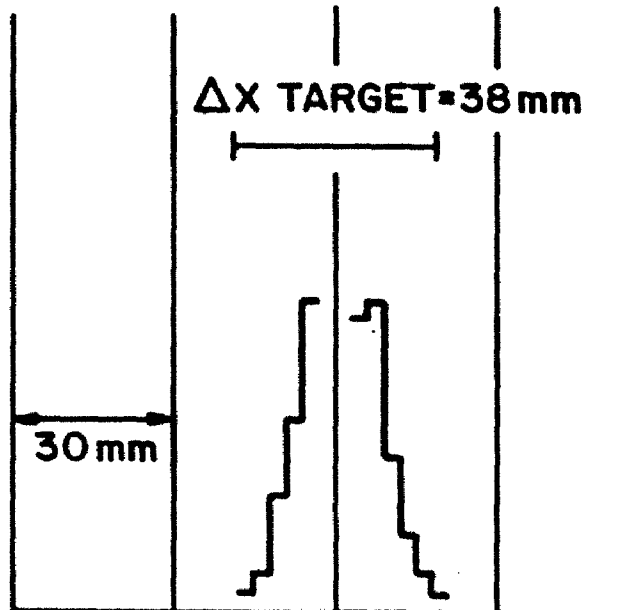
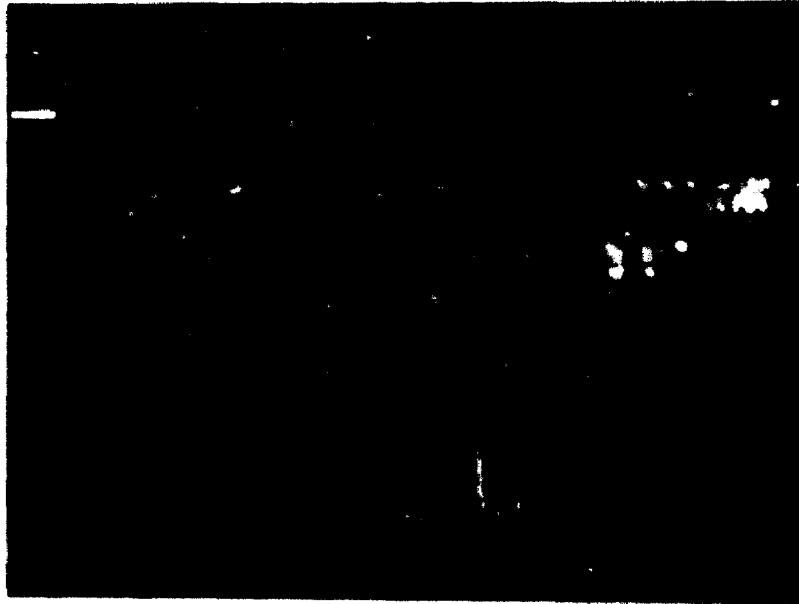


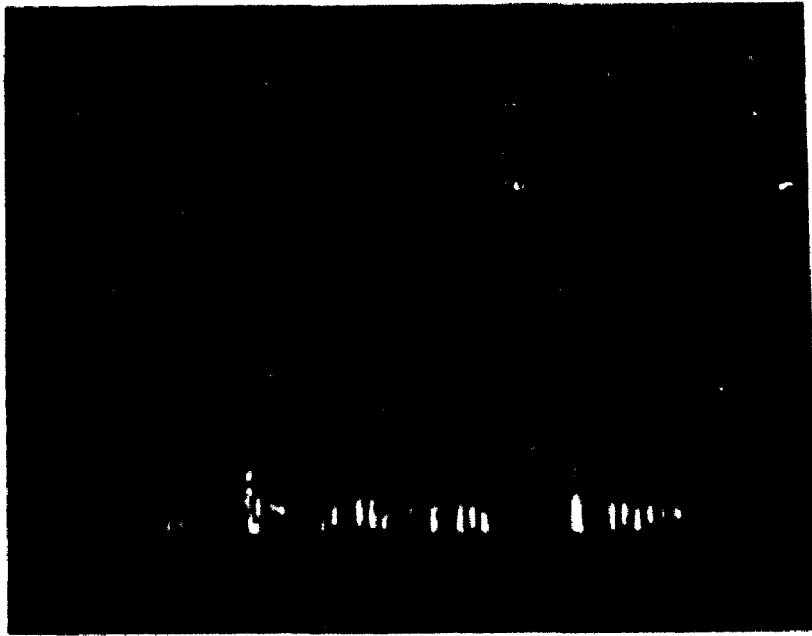
Figure 6: Beam Profile at Target

SIGNALS FROM THE BEAM CERENKOV COUNTER

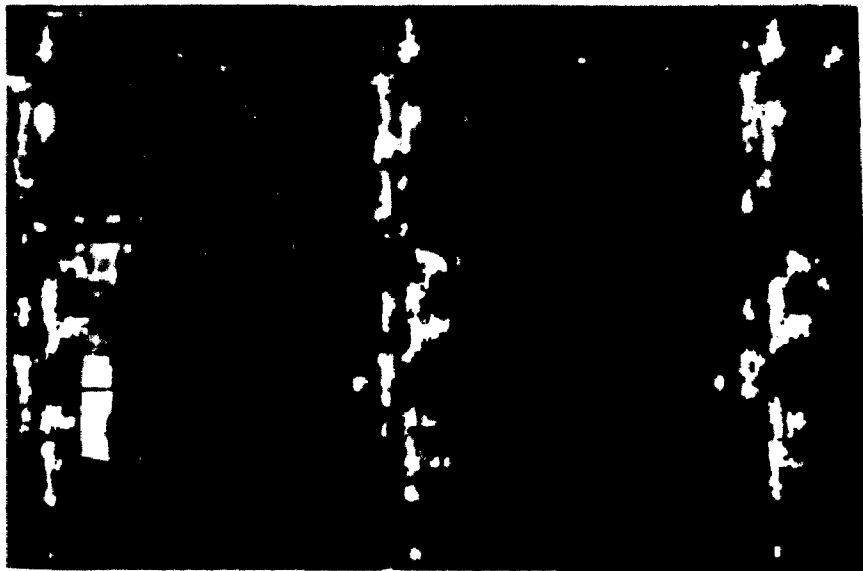
1 second full sweep



a) Uneven Distribution throughout Spill



b) 60 Hz Modulation



c) Intensity Burst at Beginning of Spill

Figure 7: Time Structure of the Beam Spill

One aspect of the beam that was never well understood was the large component of particles of a few GeV energy. Our muon singles rate ruled out their being mainly due to muon halo, and there was not enough matter between the end of the beam pipe and the spectrometer to attribute them to interactions in our experimental hall. We tentatively concluded that the low energy particles originated with the beam scraping in the region of the momentum slit. The net result of these particles was that 20 percent of the triggers in the forward spectrometer arms (when Cerenkov counters were excluded from the trigger) and 50 percent of the triggers in the slow pion spectrometer were not due to beam-target interactions.

2.3 TARGET

To enhance the precision in determining the vertex of an interaction we used a segmented target. Ten pieces of beryllium were arranged in a staircase pattern, but with every step well separated along the beam from its neighbors. The target pieces were held in place by strands of nylon twine attached to their outer edges, adding a negligible amount of interacting matter. The assembly was mounted within a six inch diameter sheet aluminum tube. Except along the top and bottom where the material was needed to support the nylon and three rings for mechanical stability, the aluminum was cut away so that the targets would be visible for the initial survey and for inspection throughout the run.

Each piece of beryllium extended .45 inches (.031 nuclear absorption, .032 radiation lengths) along the beam axis, was .14 inches high and 1.5 inches wide. The centers were separated by three inches along the beam line, and the top face of each segment was coplaner with the bottom face of its upstream neighbor. The target assembly is shown in Figure 8.

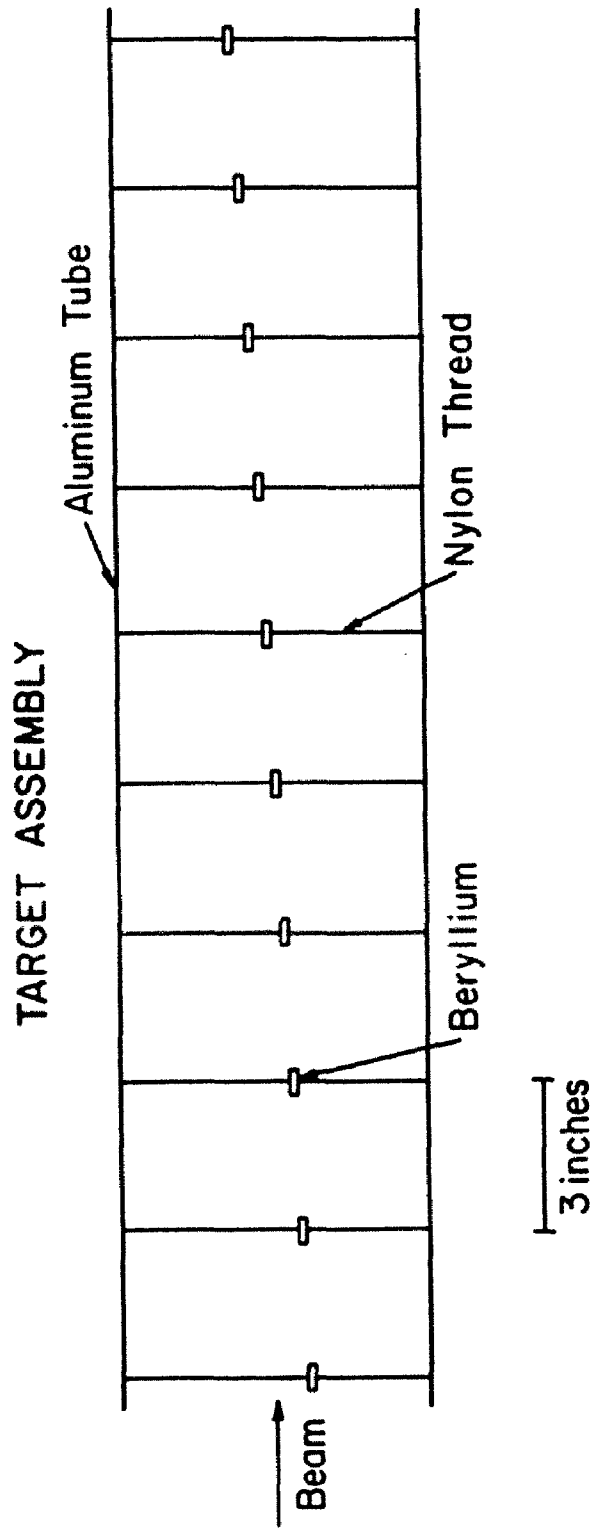


Figure 8: Target Assembly

The principal advantage of this scheme over having the equivalent amount of material in a single block is the increased ability to decide whether all members of a set of tracks have come from the same interaction. If the non-bending plane tracks in the two fast arms intersected at a z value within the target assembly, the event was assigned to a target. Further cuts were made on the bending plane track projections to the assigned target. Figure 9 shows how well the fast non-bending plane tracks found the target.

Owing to the short lever arm and the large number of triggers caused by particles not coming from interactions that took place in the target, projections of tracks in the slow pion spectrometer arms, even when taken in pairs, fail to pick out the target pieces. Nonetheless, using the vertex as determined from the fast arms as a reference for projections, the segmented target has a positive effect on resolution in the slow arms and in choosing which tracks to reject.

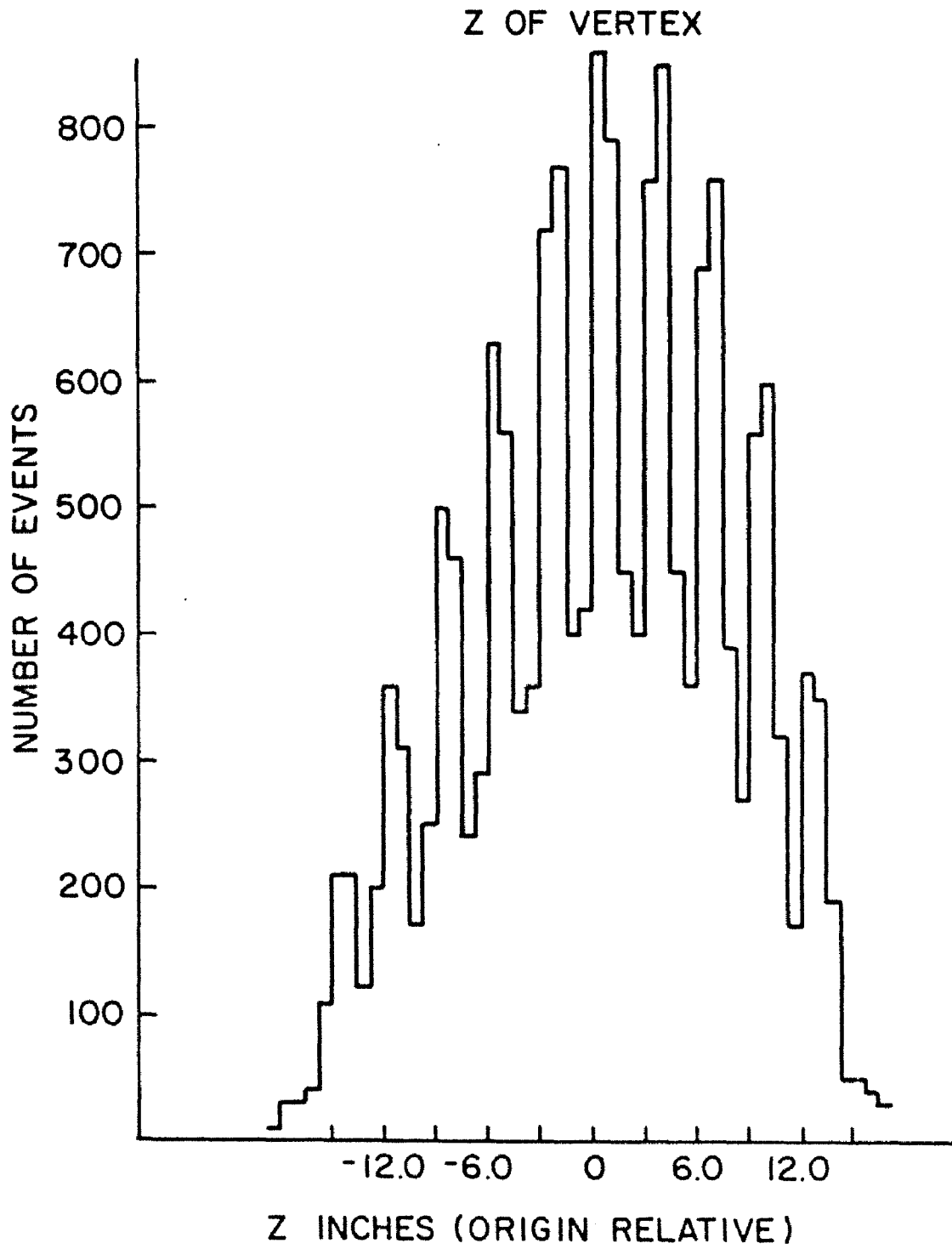


Figure 9: Z of Fast Arm Vertex

2.4 TRIGGER AND MASS MATRIX

The fast trigger logic selected, from among the millions of interactions that took place in the target every spill, a maximum of ninety-six events to be recorded on magnetic tape. With a few exceptions for diagnostic purposes, only those combinations of signals from the scintillator hodoscopes and threshold Cerenkov counters that satisfied all the requirements for being either a D^* or a J/ψ were chosen.⁵⁷ Such a restrictive trigger is necessary to gather data on exclusive channels of small cross section if one wishes to analyze them within a reasonable amount of time. Otherwise the sample would be flooded with uninteresting events. An alternative would have been to have had a multi-stage trigger with some sort of programmed trigger processor filtering the events. We chose not to take that route, because the relatively modest number of coincidence elements in our apparatus was within the range of reliable commercial and custom made, hard wired NIM logic modules.

The trigger, shown in Figure 10, is best understood as the coincidence of several subtriggers. These include the L*R (left and right) trigger, the slow pion trigger, the sign selection trigger, and the mass matrix trigger. Of equal importance to the trigger elements are the several veto elements which were integrated into the trigger logic.

A single fast arm coincidence was the registering of a signal from a counter in each of the FI, BO, BI, and BII hodoscopes. The tilted FII hodoscopes, used in matching x and y tracks, was not required. The L*R trigger was the logical product of the two fast arms along with three vetoes. The first of these, which actually entered in the left arm, was a veto on a signal corresponding to 28 photoelectrons or roughly six

⁵⁷ The lambda sample was biased. Proton - slow pion events had to have an extra pion in the remaining fast arm.

particles in the beam Cerenkov counter within one rf bucket. This veto on high instantaneous flux cut the trigger rate on the average by about ten percent. The second veto was on high multiplicity in either of the fast arms and was generated by six or more hits (three or more particles) in a BI hodoscope. A study made with this condition removed showed a 20 percent increase in trigger rate. The third veto was a one millisecond pulse generated by the previous main trigger. This prompt event dead time was inserted in order to suppress the trigger until the CAMAC system could begin to read the event and generate its own veto. Owing to the importance of these vetos, all of the complete triggers, whether for data or for calibration tapes, had L*R as one of its components.

The slow pion subtrigger required a counter signal in all three hodoscopes of an up or down arm. The two y hodoscopes⁵⁸ in each slow arm were configured with the back plane having wider counters than the front, overlapping each other in a way such that any good track from the magnet aperture would pass through the counter with the same index number on both hodoscopes. This hit matching was a trigger requirement. The intent of the x hodoscope, added especially for the second run, was to restrict the size of the accepted solid angle. The extra requirement cut the trigger rate by about 25 percent, while, according to a Monte Carlo study, it cut the D⁺ acceptance by eight percent. Information on all the hodoscopes is presented in Table 2.

⁵⁸ We use a right handed coordinate system. Y refers to the vertical axis which in this experiment is the bending plane. The horizontal (non-bending) plane is x, and the beam axis is z.

TABLE 2

Scintillator Hodoscopes

	number of elements	element size (inches)	arm coordinate (from magnet)		photomultiplier tube
			z (inches)	y (inches)	
<u>Fast arms</u>					
FIX	6	1x20	-205	0	RCA 8575
FIIX	10 + 2 ends	1x20.25	-55	0	RCA 8575
BOX	8	1.5x30	69	0	EMI 9813KB
BIY	15	3x13	71	0	RCA 8575
BIIY	24	4.5x17	197	0	RCA 8575
Muon I	2	12x48	231	0	RCA 6655
Muon II	2	12x48	262	0	RCA 6655
Muon III	2	12x48	293	0	RCA 6655
<u>Slow arms</u>					
Up(Dn)IY	8	(1.97,2.95,2.95,3.98 3.98,3.98,3.98,4.92) x 22.8	117	(-)35.3	AMP XP2020
Up(Dn)IIY	8	(4.53,5.91,5.91,7.29 7.29,7.29,7.88,9.85) x 22.8	157	(-)46.2	AMP XP2020
Up(Dn)IIIX	4	4.92x31.5	149	(-)37.9	AMP XP2020

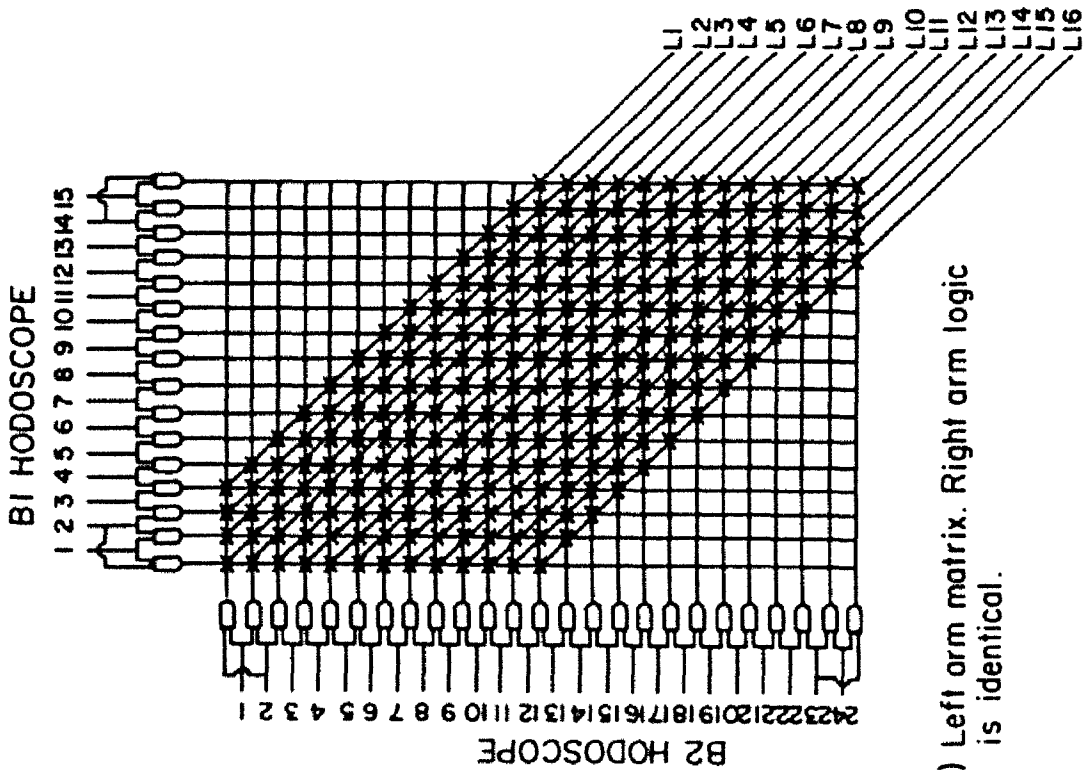
Because we wished to use the direct Cerenkov counter signals for off-line pulse height analysis, the low level of a passive 10:1 split of the output of the phototubes was used in the trigger. Before the attenuation, the gain on the phototubes was set at 25 millivolts per photoelectron. The attenuated signals were reamplified by a factor of ten and the two tubes in the threshold Cerenkov counters in each fast arm were summed. The sum was discriminated at 45 millivolts to provide the C_T and C_1 signals.

The two muon trigger demanded a hit in each of the three banks of counters, thereby requiring the particles to traverse 18 absorption lengths of steel. In addition both L^*R and $C_T^*C_1$ were required.

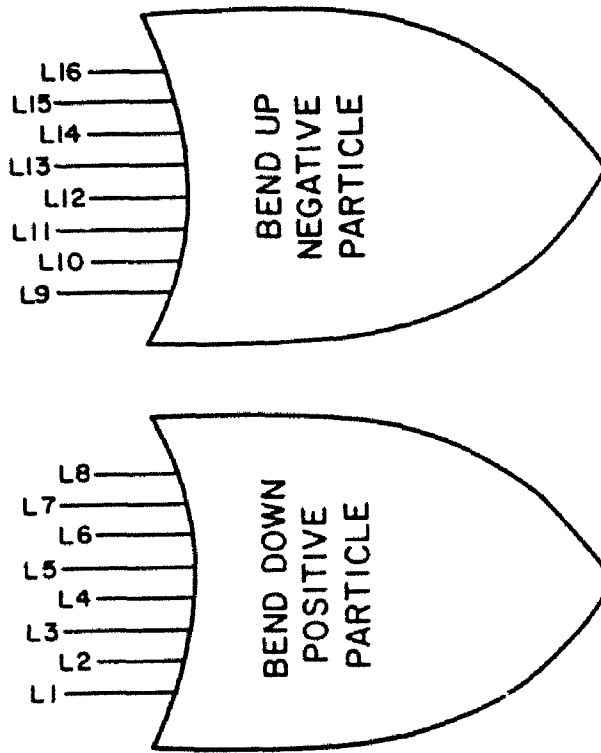
The mass matrix module, built to our specifications for this run, served two functions. It provided a signal reporting whether a particle in a fast arm was positively or negatively charged, and it correlated the momenta of the tracks in the two fast arms so as to reject low mass pairs.

Figure 11 shows the logic of the mass selection. The module received as inputs signals from the 15 overlapping BI counters and 24 overlapping BII counters. These signals were translated to 16 and 25 possible channels corresponding to an equivalent set of non-overlapping counters of half the original width. BI - BII hit pairs representing momenta greater than 3.5 GeV/c were assigned a number from one to sixteen based on how strongly the particles were bent by the BM109 magnet. An inclusive logical sum of pairs numbered one through eight provided the output signifying a down bend or positive particle. Nine through sixteen were "or"ed for the negative particles. Note that rejection on low fast arm momentum is implicit in sign selection.

MASS MATRIX LOGIC



a) Left arm matrix. Right arm logic is identical.



b) Sign selection

Figure 11: Mass Matrix Logic

The paired signals also served as the indices of a 16 by 16 array. A single output signal, representing a desired right left momentum correlation, was generated by any combination of any number of coincidences requested by means of 256 switches mounted on the front panel of the unit. The choice of desired coincidences, indicated in Figure 12, was determined by a comparison of D^* and inclusive pion events in the Monte Carlo simulation.

A D^* trigger with no requirement that the momentum in the two fast arms be correlated was formed by the coincidence of L^*R , slow pion, C_R+C_1 , and $\sim(C_R^*C_1)$. The sign selection subtrigger was constructed by requiring the sign of a particle in a fast arm with the threshold Cerenkov counter on to be the same as the trigger sign in the slow arm. The final D^* trigger was the coincidence of D^* without momentum correlations, the mass matrix, and proper sign selection.

The actual data taking trigger was an "or" of the D^* trigger, the two muon trigger, and the D^* trigger without the mass matrix prescaled by a factor of 96. The momentum uncorrelated triggers accounted for eight percent of the events written on the primary tapes, but only four percent of the fully reconstructed events. When these mass matrix off events were filtered off-line, and those not satisfying the sign selection requirement were discarded, it was determined that the effect of the two arm correlation in the mass matrix was an additional 25 percent suppression of the trigger rate at low masses. The two body mass spectra with and without the matrix requirement are shown in Figure 13.

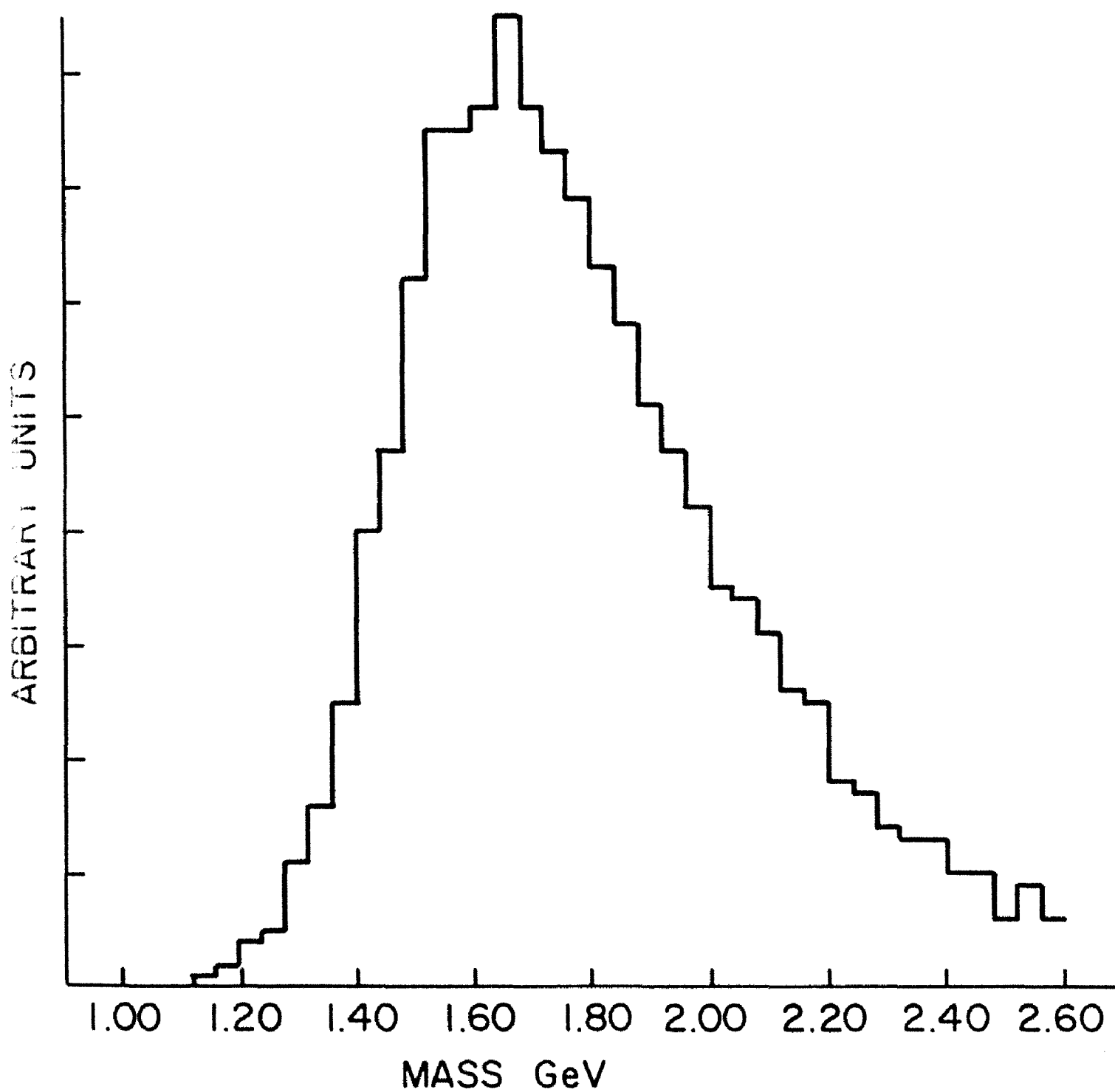
MASS MATRIX CHOICE OF TWO ARM COINCIDENCES

Right Arm

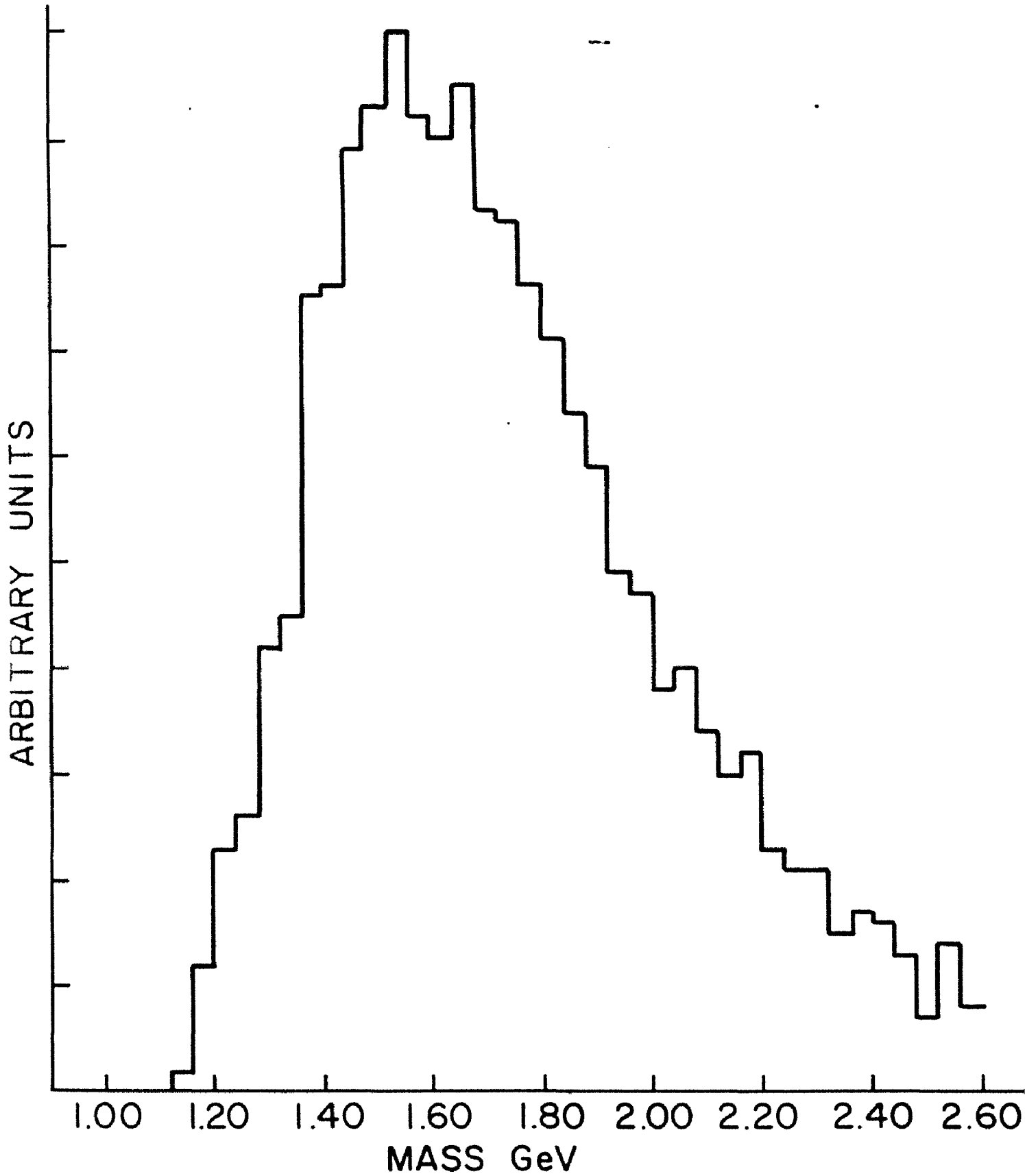
	R1	R2	R3	R4	R5	R6	R7	R8	R9	R10	R11	R12	R13	R14	R15	R16
L1																
L2								✓	✓							
L3							✓	✓	✓							
L4						✓	✓	✓								
L5					✓	✓	✓	✓								
L6				✓	✓	✓	✓									
L7			✓	✓	✓	✓										
L8			✓	✓										✓	✓	
L9												✓	✓	✓	✓	
L10											✓	✓	✓	✓		
L11										✓	✓	✓	✓			
L12										✓	✓	✓				
L13									✓	✓	✓					
L14									✓	✓						
L15																
L16																

Figure 12: Choice of Two Arm Coincidences

π K MASS SPECTRUM WITH MASS MATRIX



π K MASS SPECTRUM WITH SIGN SELECTION
SUM OF MATRIX ON & OFF



π K MASS SPECTRUM WITH SIGN SELECTION
MASS MATRIX OFF

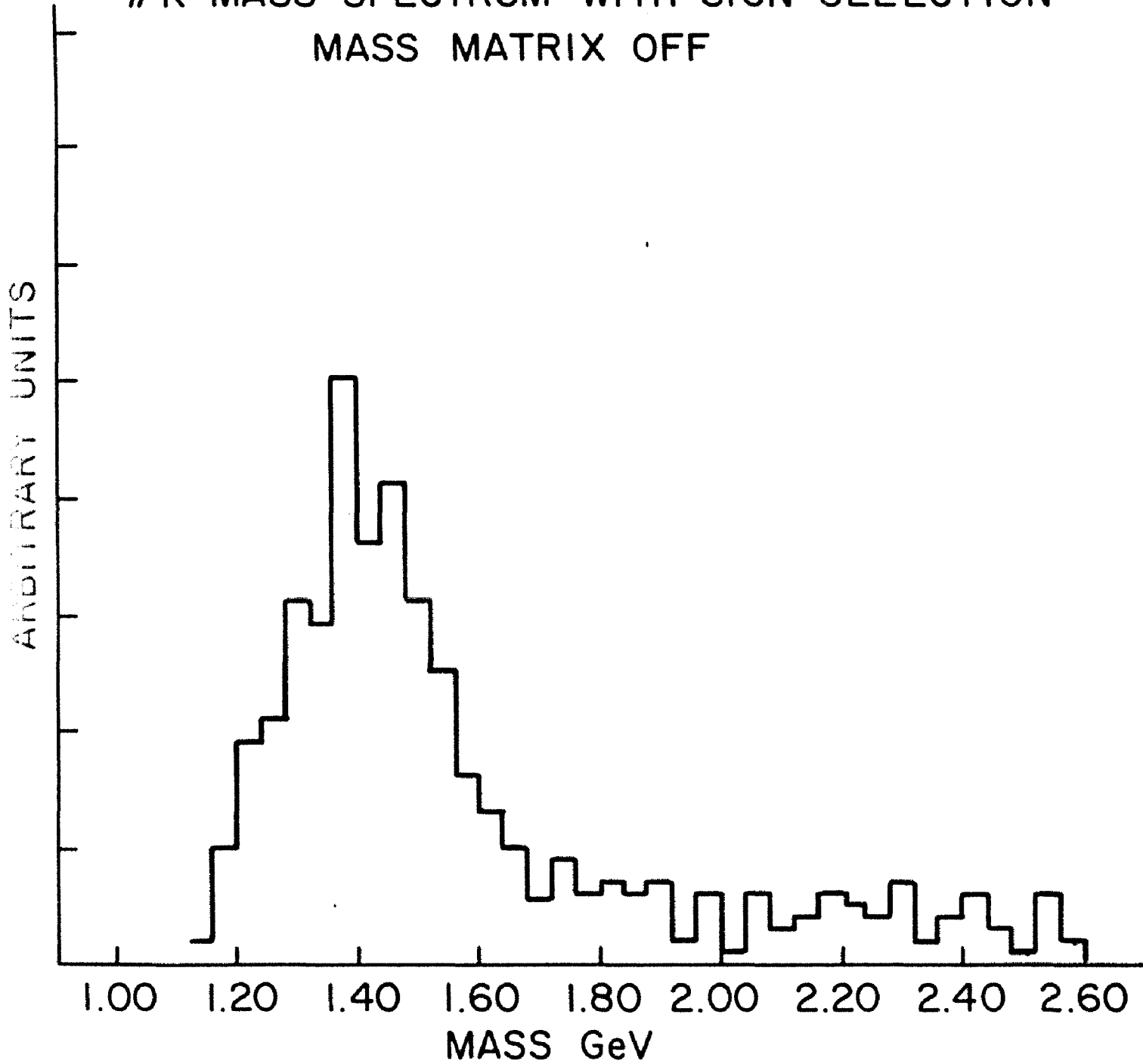


Figure 13: π - K Mass Spectra

2.5 DRIFT CHAMBERS

In a multi-arm spectrometer the measurement of particle trajectories serves two distinct functions. These are determining the magnitude of the momentum of each particle from its bend in a magnetic field and, equally important, determining the actual direction of the tracks as they emerge from the interaction so that a precise calculation of the invariant mass of the initial state can be made. For the second run the apparatus was modified primarily for the latter purpose: in each of the four arms an extra drift chamber was added just downstream of the Henry Higgins magnet aperture.

In the slow pion spectrometer arms the new chambers were actually two sets of wires mounted within one frame that surrounded the magnet exit. The chamber is depicted in Figure 14. Each active zone consisted of a single plane of twelve sense wires mounted horizontally so as to measure the vertical position of the tracks. The extra plane brought the total number of bending plane measurements to four and increased the lever arm from 118 centimeters to 171 centimeters. The geometry of the drift cell and the processing of the signals from this chamber were identical with those of the other slow arm chambers.⁵⁹

There were three measurements of track position in the non-bending plane including one in a chamber whose wires were pitched at 7 degrees from the vertical to facilitate the matching of tracks in the bending and non-bending planes. Except for the front chamber which was mounted on the magnet flux return shield plate, the slow arm drift chambers were

⁵⁹ P. Perez, thèse D. 3^e Cycle, Université Paris-Sud, 1978 (unpublished).

CHAMBER 3 UP-DOWN

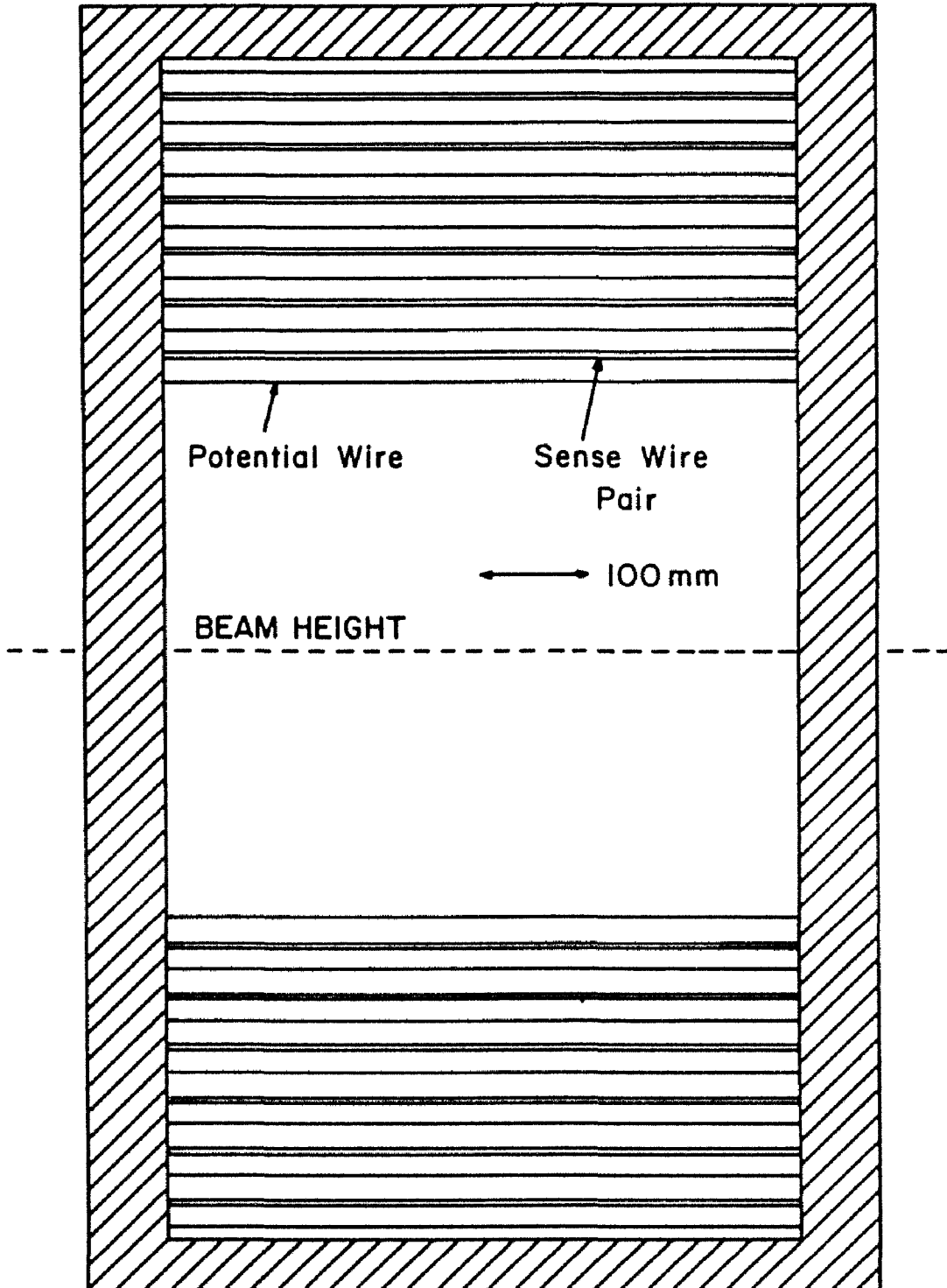


Figure 14: First Slow Arm Drift Chamber

mounted normal to the spectrometer arm axis, that is, at an angle of .25 radians to the beam. That way the path of the particles through the arm would be normal on the average to the electric field in the drift cell.

There were a total of sixteen planes of sense wires in each fast arm. Ten of these, of which five were downstream of the BM109 analyzing magnet, measured track positions in the bending plane. Only two planes of x position measurement were downstream of the magnet. Table 3 summarizes the drift chamber information.

The chambers added to the forward arms were five plane packages, two staggered planes in both the vertical and horizontal and one plane of sense wires pitched 11 degrees from the horizontal. Figure 15 shows design of the drift cells of these chambers. Like the other fast arm chambers their frames comprised several layers of G10, but in these chambers extra care was taken to keep that part of the frame nearest the beam as narrow as possible. To accommodate the high rates at the front end of the spectrometer, the cell widths were reduced by half compared with their nearest downstream neighbors. The sense wires were .5 inches apart in the x planes and 1.0 inch apart in the y and tilted u plane. The smaller cell size had no effect on the chambers' intrinsic resolution, because saturation drift velocity is independent of cell size, and time measurement precision was limited by the electronics. Also, in contrast with the other fast arm chambers, these chambers made use of field shaping wires to form a graded potential. With the small cell dimension transverse to the beam, it was thought that had the cell boundaries been grounded (as was the case for the larger chambers) there would be too little space for the uniform field crucial for efficient electron

TABLE 3
Drift Chamber Characteristics

	number of drift cells	cell width	active area width	height	arm coordinate (from magnet)
(dimensions in inches)					
<u>Fast arms</u>					
AX	15	.5	4	8	-321
AU	8	1	4	8	-319
AY	15	1	4	8	-319
OX	11	1	6	12	-255
OY	11	2	6	12	-252
1X	8	2	9	16	-212
1Y	15	2	9	16	-209
2X	19	1	10	22	-93
2Y	39	2	10	22	-91
3X	11	2	12	38	80
3Y	37	2	14	38	85
3'Y	16	2	16	32	89.5
4Y	55	2	18	56	190
(dimensions in centimeters)					
<u>Slow arms</u>					
OY	11	4.8		52.8	167
OX	9	4.8	43.2		170
1Y	14	4.8		67.2	226
1X	10	4.8	48.0		229
2X	12	4.8	57.6		286
2Y	17	4.8		81.6	288
3Y	6	4.8		28.8	111

capture to develop. That these chambers did serve their purpose in improving the vertex determination is shown in Figure 16 which contrasts events where the added chambers are present in the track fit with those where they are ignored.

The amplifiers on these chambers were identical to those on the other fast arm chambers, but owing to mechanical constraints, instead of having the signal from the sense wire immediately connected to the preamplifier chip, it was separated from the preamp by two feet of coaxial cable. Despite imperfect impedance matching, this caused no problems.

As a consequence of the small size of the chambers and the proximity to one another of conductors held at high voltage, these chambers were subject to sparking which burned out many of the preamplifier circuits. We had some success in relieving this problem by installing a pair of diodes between ground and the input to the preamplifiers. The diodes would conduct away large pulses likely to damage the integrated circuits. Nonetheless, we usually ran with about five out of the eighty channels in these chambers missing.

The emitter coupled logic (ECL) signals from all of the drift chamber amplifiers were processed using Lecroy 2770A drift chamber encoders, with a common stop signal provided by the trigger. The encoder gives a digital output corresponding to the drift time for the last hit before the common stop. The average slope is about 3 nanoseconds per count, but each channel had to be calibrated individually. We used a gas mixture of 50 percent argon 50 percent ethane by volume. The measured drift velocity was 0.00529 centimeter per nanosecond.⁶⁰ When calibrating the digitizers using well timed pulser generated signals we found the

⁶⁰ A.D. Montag, "Drift Velocity Calibration", 1978 (unpublished).

SCHEMATIC SIDE VIEW OF CHAMBER A PACKAGE

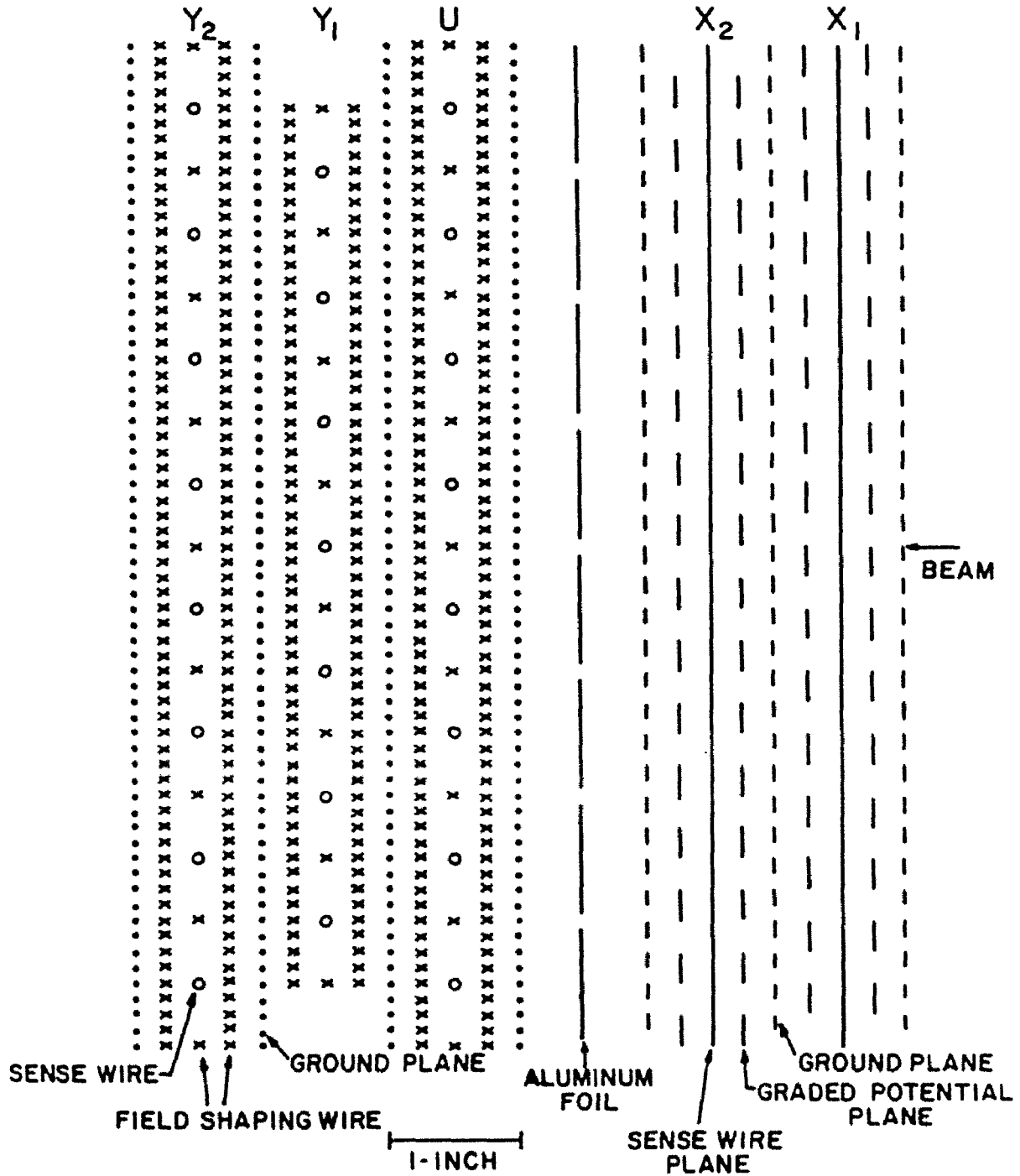


Figure 15: First Fast Arm Drift Chamber

$Y_{RIGHT} - Y_{LEFT}$ AT THE TARGET

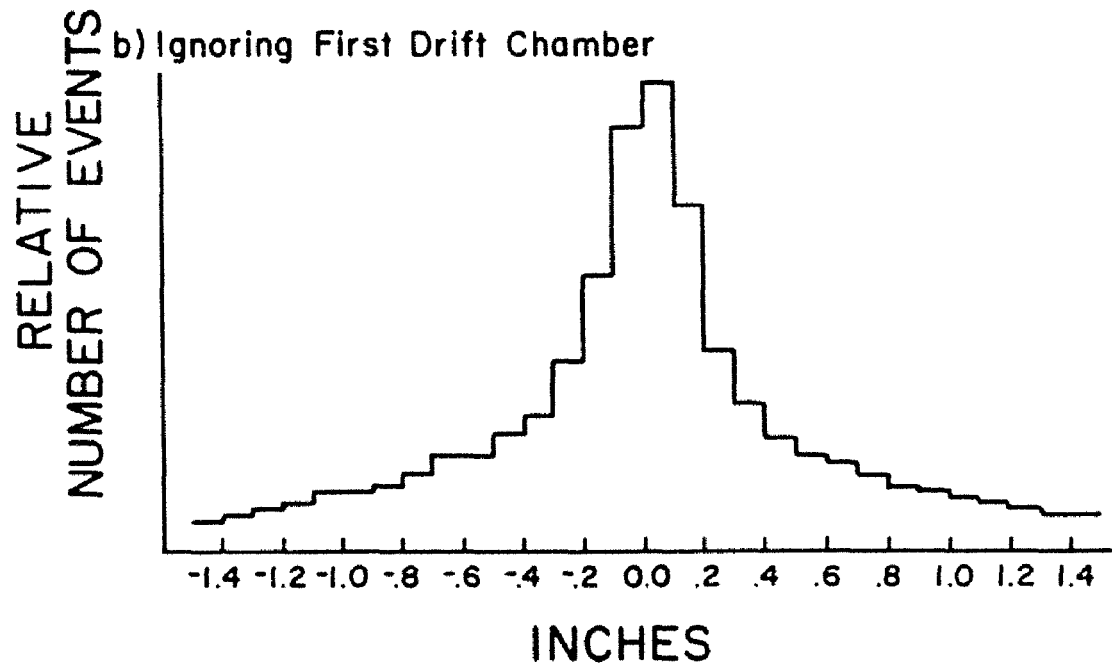
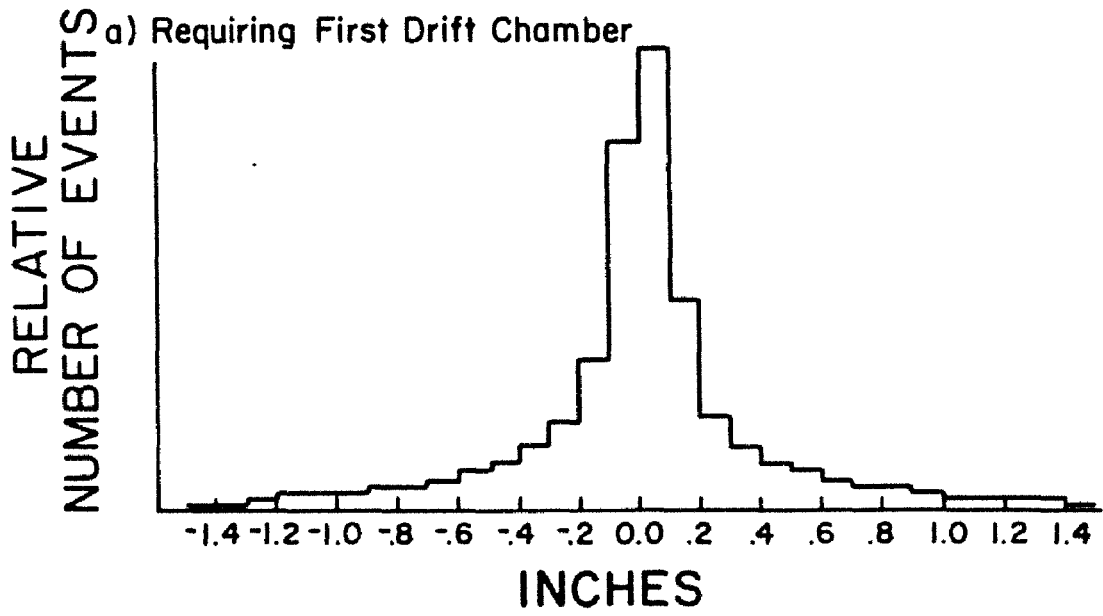


Figure 16: Y Vertex in Fast Arms

measurements repeatable to ± 1 count, corresponding to .016 centimeters.

2.6 CERENKOV COUNTERS

The identity of a particle passing through a fast arm of the spectrometer was determined on the basis of information from two Cerenkov counters. One, filled with carbon dioxide at atmospheric pressure, was used to identify pions. It operated in a purely threshold mode. The other, filled with isobutane also at atmospheric pressure, served principally to separate kaons from protons. Relevant properties of the two gases are shown in Table 4. The isobutane counter had the additional feature of having the Cerenkov light ring projected on a rosette shaped mask, dividing the light into an inner and outer signal, thus allowing the counter to be operated in a differential mode.

TABLE 4
Gases Used in E650 Cerenkov Counters

	N	Threshold Momentum (GeV/c)		
		Pions	Kaons	Protons
Isobutane	1.000128	2.76	9.75	18.54
CO ₂	1.000410	4.87	17.24	32.76

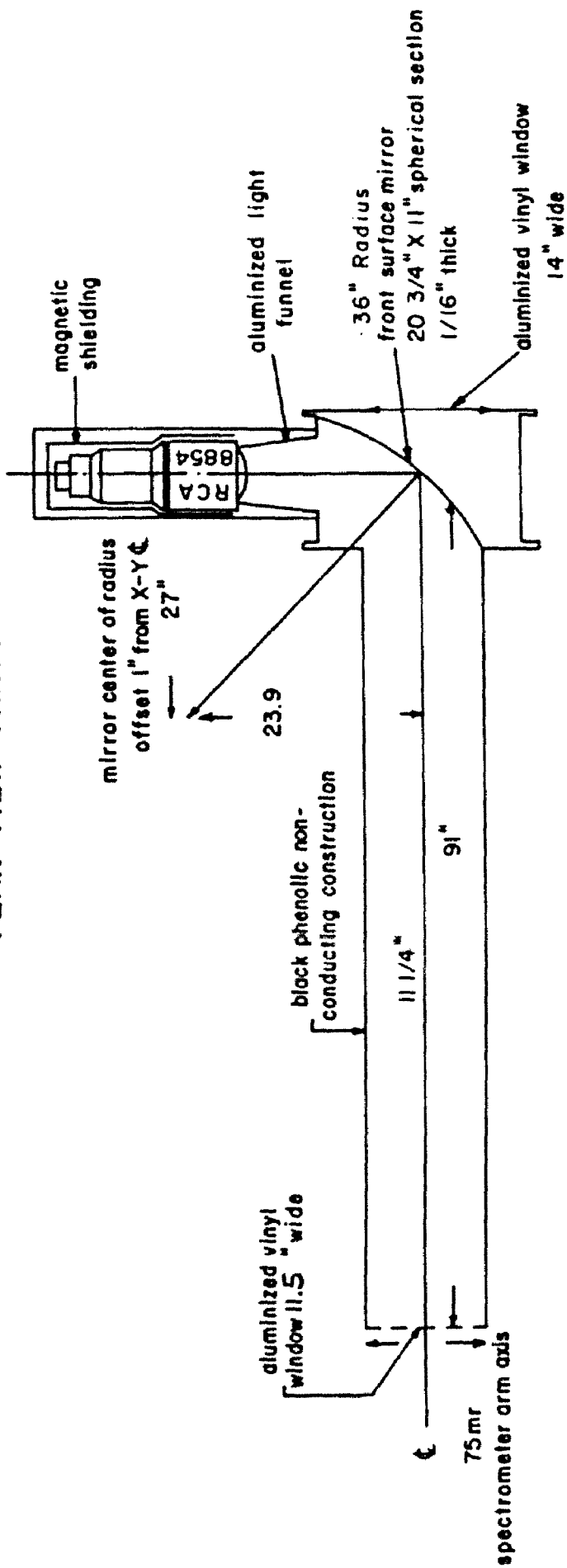
Although the selected combination of gases allows for the identification of pions over the entire range of accepted momenta, for the ten percent of reconstructed tracks with momenta below the Cerenkov threshold for kaons in isobutane, protons and kaons remained indistinguishable. When searching for a D^* signal they were all considered to be kaons; when looking for lambdas they were treated as protons.

Each of the Cerenkov counters was divided at beam height into independent, identical, upper and lower optical cells. Each threshold cell had one RCA 8854 photomultiplier tube, and each differential cell had two. Details of the construction of a cell of each counter are shown in Figure 17. For a track passing sufficiently far away from the cell boundary, it was only necessary to examine light from one cell. This ameliorated to some extent the problem of light contamination from particles that passed through the Cerenkov counter, but were not accepted by the whole spectrometer. Under the right circumstances it also allowed for an unambiguous identification of particles when there were two tracks in an arm. For tracks passing near the cell boundaries, the useful signals were the sums of the light from the cell pairs.

Signals from the threshold Cerenkov counter were part of the trigger logic, but the actual particle identification was performed off line. The high signal from a 10:1 passive split from each phototube was sent to a Lecroy 2249 analog to digital converter. It was on this digital information that the analysis was performed.

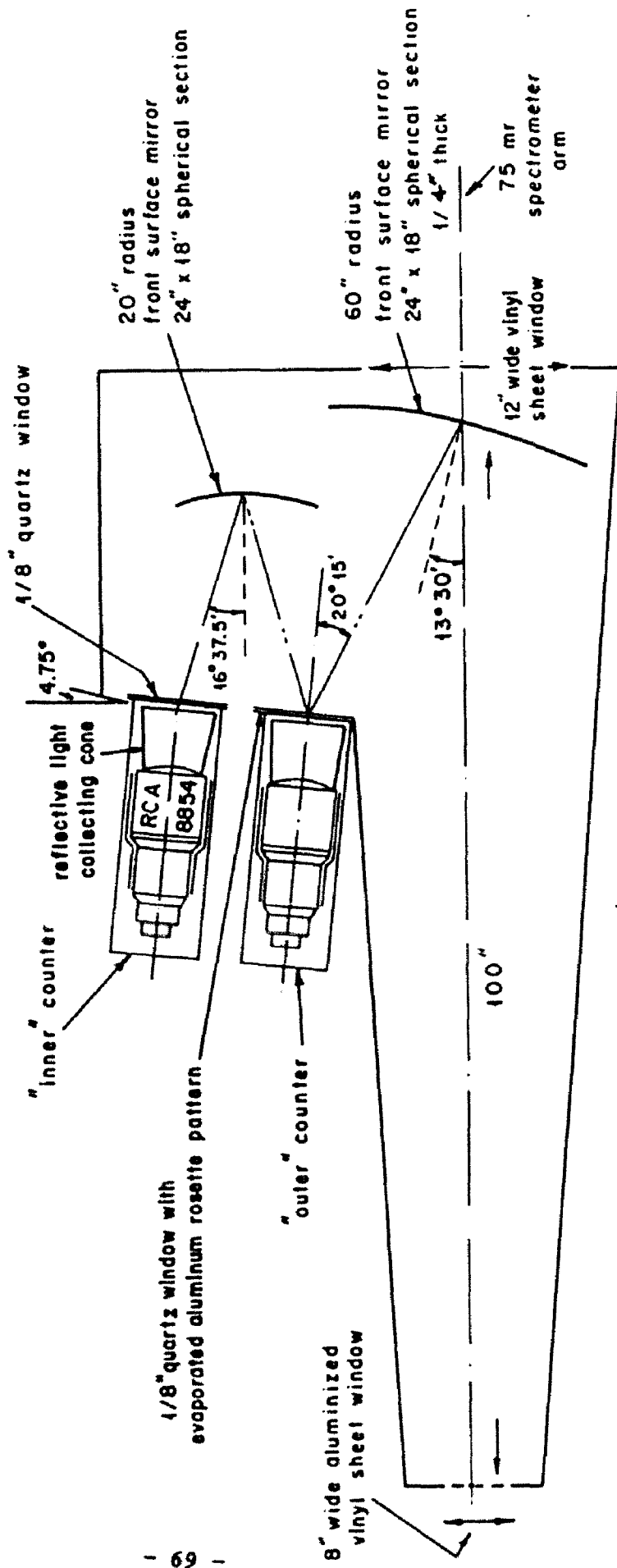
E567/302 THRESHOLD CERENKOV COUNTER

PLAN VIEW THROUGH MIRROR CENTER



E567/302 DIFFERENTIAL CERENKOV COUNTER

PLAN VIEW



E567/650 DIFFERENTIAL CERENKOV COUNTER
ROSETTE WINDOW

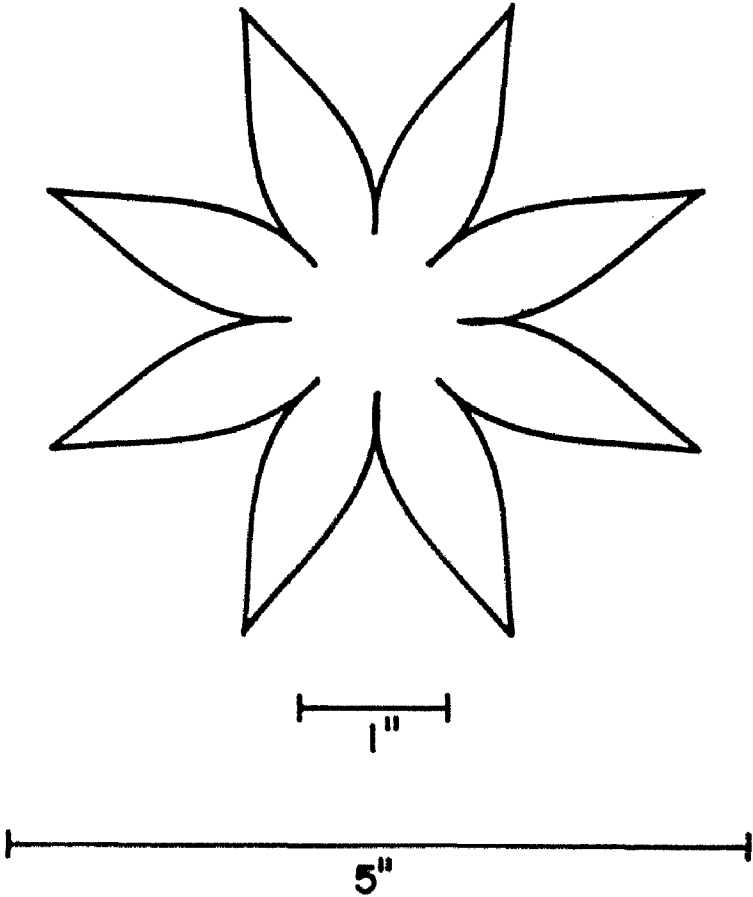


Figure 17: Cerenkov Counters

2.7 DATA ACQUISITION AND ON-LINE MONITORING

The data acquisition system, initiated by a signal from the trigger logic, was standard CAMAC. Table 5 shows the format of each event. The 16 bit words were written in a buffer memory of 32,000 word capacity that permitted registering a maximum of 96 events per beam spill. Reading out the data took 2.5 milliseconds on the average, resulting in a trigger induced deadtime of about 20 percent. At the end of each spill, or when the buffer was full, the entire contents were dumped to magnetic tape in the form of eight 4000 word records.

TABLE 5
Primary Event Format

Data	Number of words
Fixed words	4
Pattern words	14
TDC's	72
ADC's	96
Scalers	24
Drift chamber encoders	10-952

Half of the memory was installed specifically for the second run. In the 200 GeV/c run only 48 events could be recorded per spill, and we ran at the lowest intensity that would saturate this trigger rate. Doubling the memory allowed us to record 96 events per beam spill. Because the average number of particles traversing the spectrometer per trigger increased with beam intensity, a beam intensity sufficiently high to result in 96 triggers caused more particles to pass through the apparatus than the track reconstruction program could efficiently handle. The beam intensity at which we chose to run was therefore limited not by the

rate at which we could record events, as had previously been the case, but by our ability to reconstruct them.

An HP2116B computer, operating in parallel with the data acquisition system, read the data in the first record of each spill. The on-line program could thereby monitor the status of every component spill by spill. This monitoring was critical, because certain pieces of equipment, such as the drift chamber encoders and the differential Cerenkov counters, had failure modes to which the trigger rate and other continuously scaled quantities were insensitive.

Chapter III

EVENT RECONSTRUCTION

3.1 DRIFT CHAMBER ALIGNMENT

Track reconstruction begins with the translation of the time information from the drift chamber encoders to track positions. To accomplish this one must know the physical location of every sense wire and the relationship between the digital timing signal and drift distance for every channel. To first order this information can be derived from a survey of the drift chamber positions and from a calibration of the electronics by pulsing the drift chamber digitizers with signals of known but varying delay. Both the survey coordinates and the timing constants can then be tuned to finer precision by making small shifts to minimize the fit residuals of tracks from data taken with the analyzing magnets off. In the present experiment, these procedures met with complications that resulted in significant delays in the analysis. Different problems dominated in the different arms.

The geometric alignment of the forward spectrometer arms was a straightforward exercise. Several sets of values from several sets of position measurements had to be reconciled. The main complication was that some of the apparatus had been moved between surveys. The solution relied simply on giving greater weight to measurements that were most confidently reproduced: positions of easily accessible chambers with visible wires. At this initial stage the stress was on the internal consistency of the coordinates within an arm. Overall arm shifts were dealt with later.

Throughout the running period there were drifts in the timing calibration in several of the drift chambers, causing deviations of as much as .05 inches from zero in the centroid of plots of the measured track position minus the fitted position. The gas mixing system (shared with and independently monitored by another experiment) was reliable to better than half a percent variation in relative concentration, and the drift chamber high voltages were kept well above drift velocity saturation. We concluded that the problem originated within the drift chamber encoders, which were known to be sensitive to the CAMAC crate temperature and power supply voltage variations.

The staggered cell construction of the fast arm chambers allowed us to compensate for this on a chamber by chamber basis. For each chamber a parameter T^1+T^2 was defined. This number was equal to the sum of the TDC values of the two hits in a chamber from a single charged particle traveling exactly perpendicular to the sense wire plane. It also equalled the number of counts in twice the cell drift distance. The distance of a hit from a wire in units of the cell width is $2T_{hit}/T^1+T^2$. By adjusting T^1+T^2 by amounts of about $2(T_{hit}-T_{fit})/(T^1+T^2)$, $\langle T_{hit}-T_{fit} \rangle$ could be kept near zero. We were unable to compensate for calibration drifting in the single plane slow arm chambers, but luckily the encoders associated with those chambers were among the more stable ones.

The task of aligning the chambers in the slow pion spectrometer was quite difficult. The chambers had opaque windows, meaning that wire positions had to be calculated using their distances from measured points on the chamber frames. Distances within chambers were inferred from design drawings. Tilting the chambers to make the drift planes normal to

the arm axes introduced additional measurement uncertainties by eliminating convenient right angles.

Since the spectrometer was designed to have the collimator within Henry Higgins block the direct line between the target and the active region in the chambers, a tape with the magnet off was written with a .5 inch cubic aluminum target mounted in the center of the magnet. This tape was used primarily to insure that the two slow pion arms pointed to the same vertex. The individual arm alignment was done using normal data which tended to be cleaner and allowed a determination of how small position changes affected the actual reconstruction efficiency.

The techniques used in aligning the slow pion chambers are described in detail in reference 59. The alignment was first performed on the three downstream chambers which had been in use during the first run. That solution was then used to point back to the chamber mounted on the downstream shield plate of the magnet.

Hall probe measurements of the Henry Higgins magnetic field indicated that a significant fraction of the field integral was in the space downstream of the first slow arm chamber. The shift of a hit in the first chamber was estimated to be about $.08/p(\text{GeV}/c)$ inches. In aligning the chambers in the slow pion arms one quantity that was tuned was T_0 , the y intercept of the time versus drift distance line plotted for each wire. This adjustment, motivated by a distrust of the original pulser derived digitizer calibration, was equivalent to a wire by wire position adjustment involving changes in several T_0 's in the first chamber by as much as ten counts. Because the angle, momentum, and hit wire in the front chamber were closely correlated, the effect of tuning T_0 on data taken

with the magnet on was to automatically introduce the momentum correction. Figure 18 shows the hit-fit values for the front chamber as a function of wire number, angle, and momentum. Because of higher average momentum and the chambers' being further downstream of Henry Higgins, the effect of the fringe field on the first fast arm chambers was negligible.

HIT-FIT vs. SLOPE OF TRACK FOR FIRST UP ARM CHAMBER

SLOPE OF TRACK IN UP ARM	.15	1	1	4	3	9	12	5	5	4	4	3	7	5	2	2	1	1			1
	.17	2	3	4	4	7	10	14	9	16	32	38	25	21	34	19	12	2	3	4	1
	.19	2	7	16	26	27	26	24	21	24	34	39	36	17	9	3	2	4	1		2
	.21	2	1	9	10	13	16	29	37	50	40	32	13	7	4	7	1	4	1	2	1
	.23	4	2	1	2	3	16	23	47	90	63	50	28	15	3	8	1	2		3	2
	.25	1	2	3	2	6	12	15	38	64	74	56	26	17	17	10	6	3	5	2	1
	.27	1		3	1	6	8	10	21	53	59	65	29	26	35	24	6	4	2	2	3
	.29	1	4	1	3	3	2	10	22	43	78	78	36	32	18	8	9	4	2	3	3
	.31	2	1		1	3	6	13	25	54	47	39	33	26	16	10	8	2	3		
	.33	1	2		2	2	9	4	24	24	39	39	31	33	17	12	4	6	2		2
	.35		1	1	3	1	2	7	12	23	32	35	28	30	18	10	5	2	1	2	1
	.37		3	1		1	5	8	9	17	24	26	28	21	20	13	5	5	1	3	
	.39					2	3	6	4	7	8	21	23	13	11	6	6	3	5	1	
	.41			1				2	1	2	5	2	7	3	6	1	5	2	2	1	
.43	1			1		1	3	1	1	5	7	3	4	2	1	2	2	1			
		.35	.28	.21	.14	.07	0.	.07	.14	.21	.28										

MEASURED HIT POSITION-FIT TRACK POSITION cm

HIT-FIT vs. WIRE FOR FIRST UP ARM CHAMBER

WIRE NUMBER	1	3	3	6	8	13	19	21	51	79	167	175	138	126	38	14	10	16	13	3	10
	2	7	1	2	7	7	34	68	78	108	168	117	41	14	11	7	4	6	6	2	7
	3	1	2	3	1	4	5	13	45	120	186	105	42	17	10	7	7	5	6	3	2
	4	2	2	3	4	1	2	2	14	44	100	107	84	45	16	11	2	3	2	2	1
	5	1	3	2		4	4	5	24	63	115	107	41	18	4	3	4	3	1		
	6	1		4	1	3		2	3	25	61	78	45	33	15	6		3	3	1	1
	7			2	3	2	3	2	6	26	42	45	33	8	3	2			1		2
	8			2		1		3	12	23	30	39	15	7	3	1	3				
	9				1	1	2	7	14	11	10	6	4								1
	10			1					1		1		1	2	2						
		.6	.54	.48	.42	.36	.30	.24	.18	.12	.06	0.	.06	.12	.18	.24	.30	.36	.42	.48	.54

MEASURED HIT POSITION-FIT TRACK POSITION cm

HIT-FIT FOR FIRST DRIFT CHAMBER UP ARM

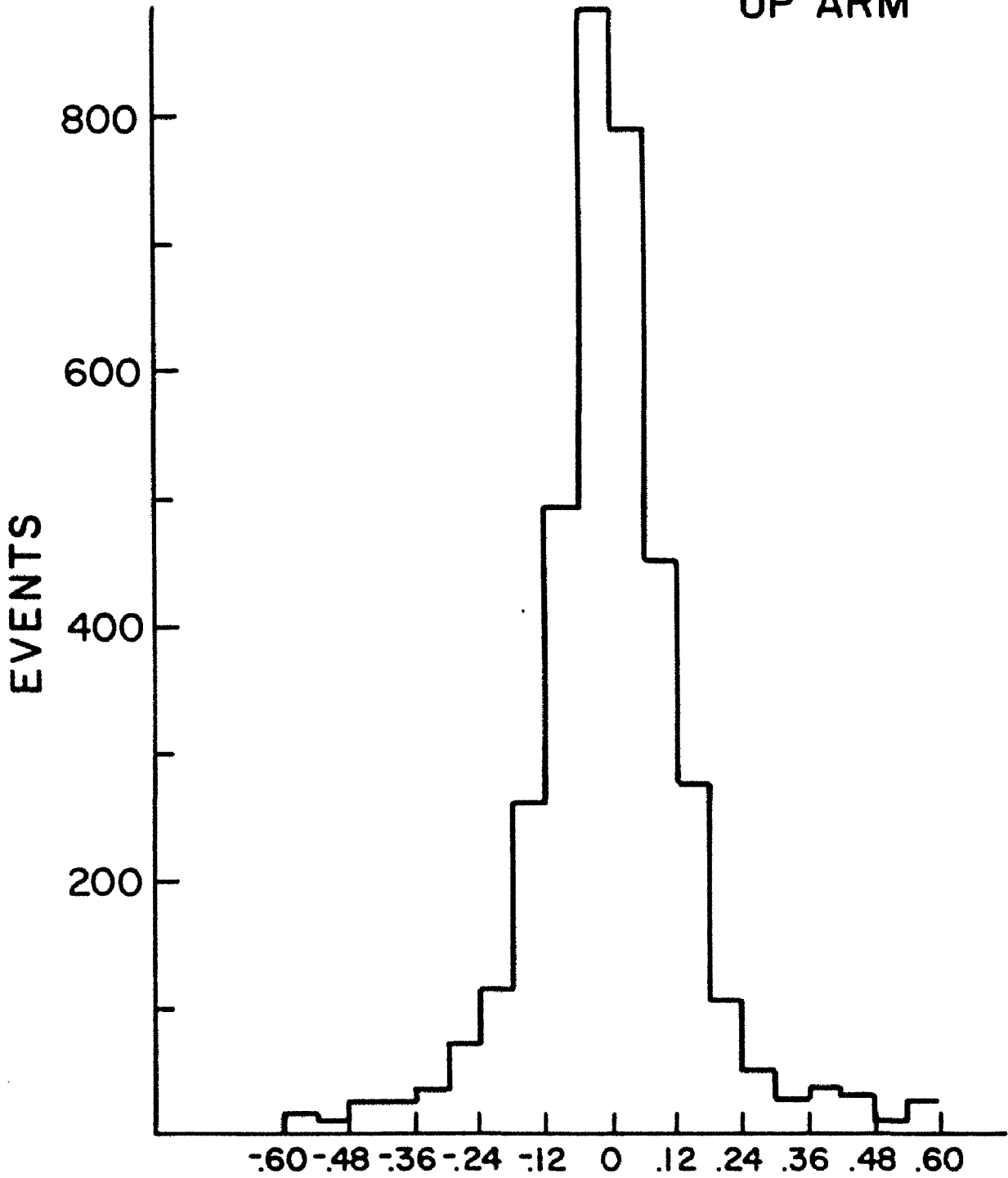


Figure 18: Hit - Fit in the Front Slow Arm Chamber

3.2 TRACK RECONSTRUCTION

The computer program used to reconstruct tracks continued its evolution from AGS Experiment 694 and Fermilab Experiment 567 with most of the changes taking place in the slow pion reconstruction routines. Figure 19 is a schematic flow chart showing how the program operated.

The tracks in the fast arms were found according to the following scheme. The bending and non-bending planes were handled separately. Combinations of scintillator counters registering signals that lay along straight lines were taken to define "trails". Only trails passing through the magnets and pointing to the target were considered. The width of the trail at each drift chamber plane was determined from the counter widths and the wire spacing in the chambers. Every pair of signals (called a "line" by the program) or single hit (when only one of the pair of sense wires registered) from each chamber was then assigned to one or more trails. Chamber signals not falling within trails were ignored. Starting from the downstream end of the spectrometer the lines and single points within a trail were scanned to see if they could be connected to form a track that stayed within the trail. Every extra line or point added to the track narrowed the window for subsequent searches.

In practice the search procedure was complicated, being governed by a set of 36 septuplets which were sets of search contingency index parameters. The index referred to different locations in the computer code. Each of the septuplets, which were ordered in decreasing likelihood of containing a pattern of hits corresponding to a track, was tried in turn until two tracks in each plane were found or until all the possibilities had been exhausted. To summarize: in the fast arms trails were searched for lines and points to form tracks.

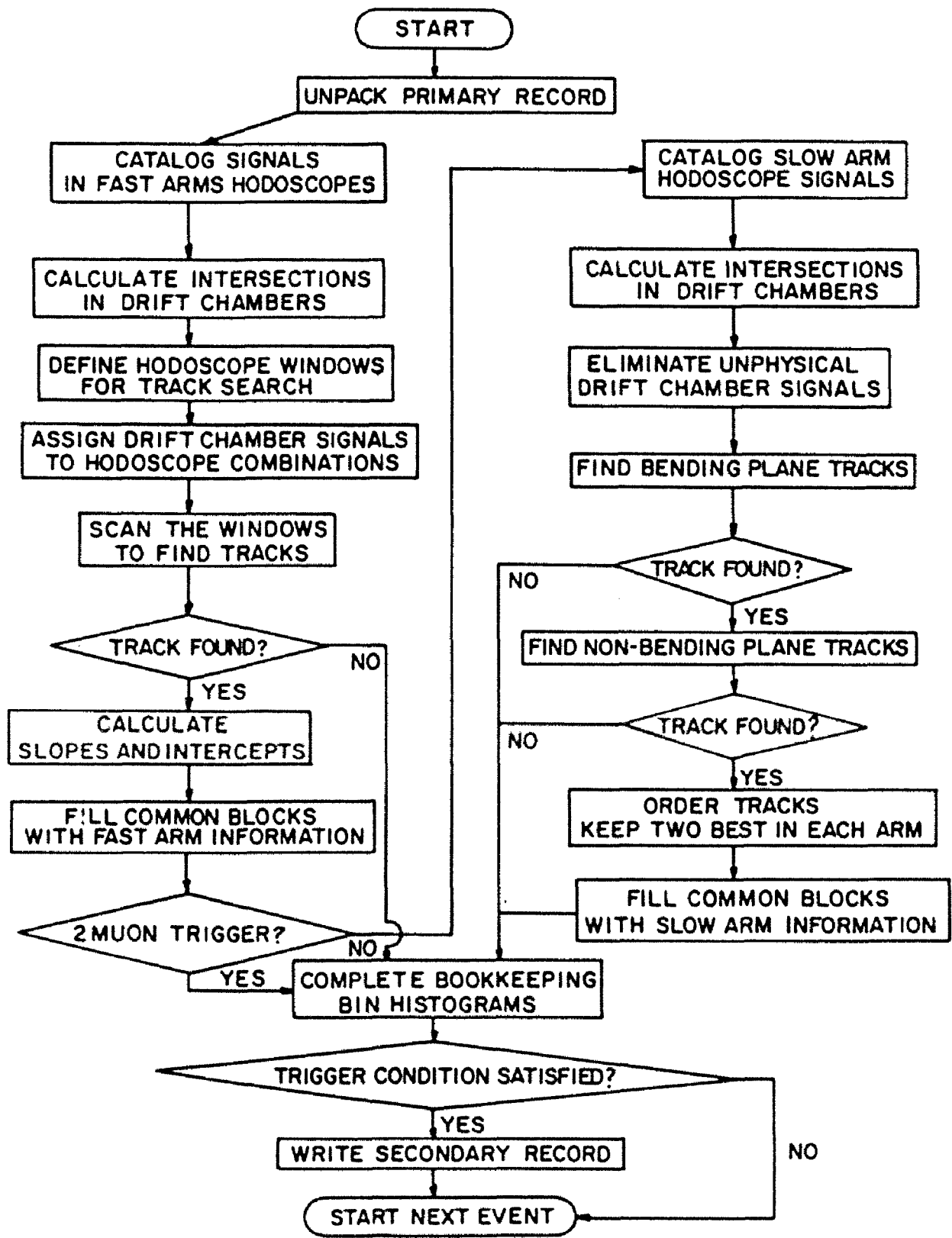


Figure 19: Track Reconstruction Program Flow Chart

At the initial reconstruction stage, the track using signals from the greater number of sense wires in the bending plane was paired with the track with the greater number of signals in the non-bending plane. The information from the tilted plane of the front chamber was not used. The definition of a good reconstructed track was one using signals from two sense wires in the non-bending plane and three in the bending plane, including one in the furthest downstream chamber 4Y and one upstream of the BM109 analyzing magnet. The average best fast arm track had signals from eight non-bending plane wires and ten bending plane wires.

In the slow pion spectrometer the trigger condition of paired counters in the bending plane immediately defined the paths of the particles. As there were only seven sense wire planes per arm, the reconstruction algorithm was comparatively simple. Pairs of signals in the first and last chambers where wire hits were registered were examined to see whether the line they defined was within the path defined by the counter pair, pointed to the center of Henry Higgins, and avoided the collimator. The signals in the intermediate chambers were scanned to see if they fell along these lines. Four-point tracks were accumulated first, then three-point tracks, until either ten tracks were found or all the signal combinations had been tried.

The process was then repeated in the non-bending plane with the additional complication that the point where the particle path intersected the chamber in the middle, tilted plane chamber, was calculated with the aid of information from a bending plane track. That is, a non-bending track was sought to correspond with each bending plane track. Only if no two-point or three-point tracks were found using the middle sense

wire plane did the program record a two-point track omitting that plane. Before the final fit was made the intersection positions were corrected by the cosine of the angle between the track and the electric field. Lastly the paired, fitted tracks were ordered by number of sense wire signals used and goodness of fit, and the two best tracks in each arm that contained a proper combination of counter signals were kept.

In this experiment the reconstruction efficiency was inversely related to the intensity of the particle flux through the drift chambers. This was because for each trigger only one passing particle per sense wire, the one whose ion trail reached the sense wire last, could be registered. Therefore extra particles passing through the drift chambers could have the effect of erasing important information. The chambers in the slow pion spectrometer being among the furthest upstream were most susceptible to the ill effects of high intensity, and the ability to reconstruct tracks in the slow arms became the limiting factor in the beam intensity we could take.

Under optimum conditions, the reconstruction efficiency in the slow pion spectrometer arms was about 70 percent. The quantity we wished to maximize, however, was the number of reconstructable tracks written per unit time, and not the reconstructable fraction. This made it to our advantage to run the experiment at a beam intensity that resulted in a particle flux through the drift chambers that was past the peak in our slow arm reconstruction efficiency. At our average running intensity of 1.1×10^8 pions per pulse, slow pion reconstruction was about 54 percent efficient and fast arm track reconstruction was about 71 percent efficient.

The data sample for this experiment consisted of about 5.8 million events written on about 220 reels of tape each 2400 feet long at a density of 800 bpi. For convenience in tape handling, most of the primary tapes were condensed to 6250 cpi tapes, four or five to the reel. The first pass at analyzing the data was simply to reconstruct the tracks. If an event had a track in each arm requested by the trigger (three arms for a D^* , two for a J/ψ) the primary analysis program would write on disk a data summary record. Table 6 gives the format of a data summary record. The data summary disk files were collected onto data summary tapes (DST's) of which there were 17 containing 915,726 events. All subsequent analysis was performed on the DST's or on filtrations thereof, with the event format and content remaining unchanged. That is, although several of the quantities in the data summary record were altered in the secondary analysis, all of the filtration programs whether for muon trigger events, lambda candidate events, or mass matrix off events, stored and wrote out the information as it appeared on the DST so that filtering programs did act as projection operators.

TABLE 6
Data Summary Tape Format

Quantity	Number of words	Bits Per Word
Fixed words	4	16
Pattern words	14	16
ADC(53-56,61-72)	16	16
Scalers	24	16
Words in /GOOD/	1	16
Number of tracks	1	16
Track parameters	104 x no. of tracks	25
Hits per track	68	5
Counters hit	16	16
Pulse heights	16	16
Momentum	8	24
Polarity	8	5
Track index	32	5
Magnet polarity	4	5
Maximum number of bits per event = 25,124		

3.3 PARTICLE IDENTIFICATION

The first step in the particle identification procedure was the normalization of the pulse height distributions of the different phototubes to compensate for the variations in average amplitude that occurred throughout the experiment. To set the base line, pedestals were subtracted from the ADC signal from each phototube of the Cerenkov counters. The pedestals were determined from the average amplitudes on tapes written with the beam off and a pulser initiated trigger. The pedestals were quite stable with the only significant shift being due to a decrease in the width of the ADC input gate made about a third of the way into the run. The wide gate had been contaminating the charge integration with overshoot.

Other factors, which did not affect the pedestals, caused major variations in the average pulse height. These included several voltage

changes to various tubes and the burn out and subsequent replacement of two bases. As a result, each ADC reading had to be multiplied by a gain factor which was a function of run number. The gain factor was determined by plotting a sample of high momentum pions where the pulse height could be expected to have saturated. Samples were plotted for every run preceding and following a voltage change or a power down, and also at intervals of less than ten runs (roughly one day) in regions of expected stability. Each threshold counter tube was rescaled to saturate at 140 counts, and each differential counter tube at 50 counts. Figures 20 and 21 show a typical pion pulse height distribution and the variations in average which took place.

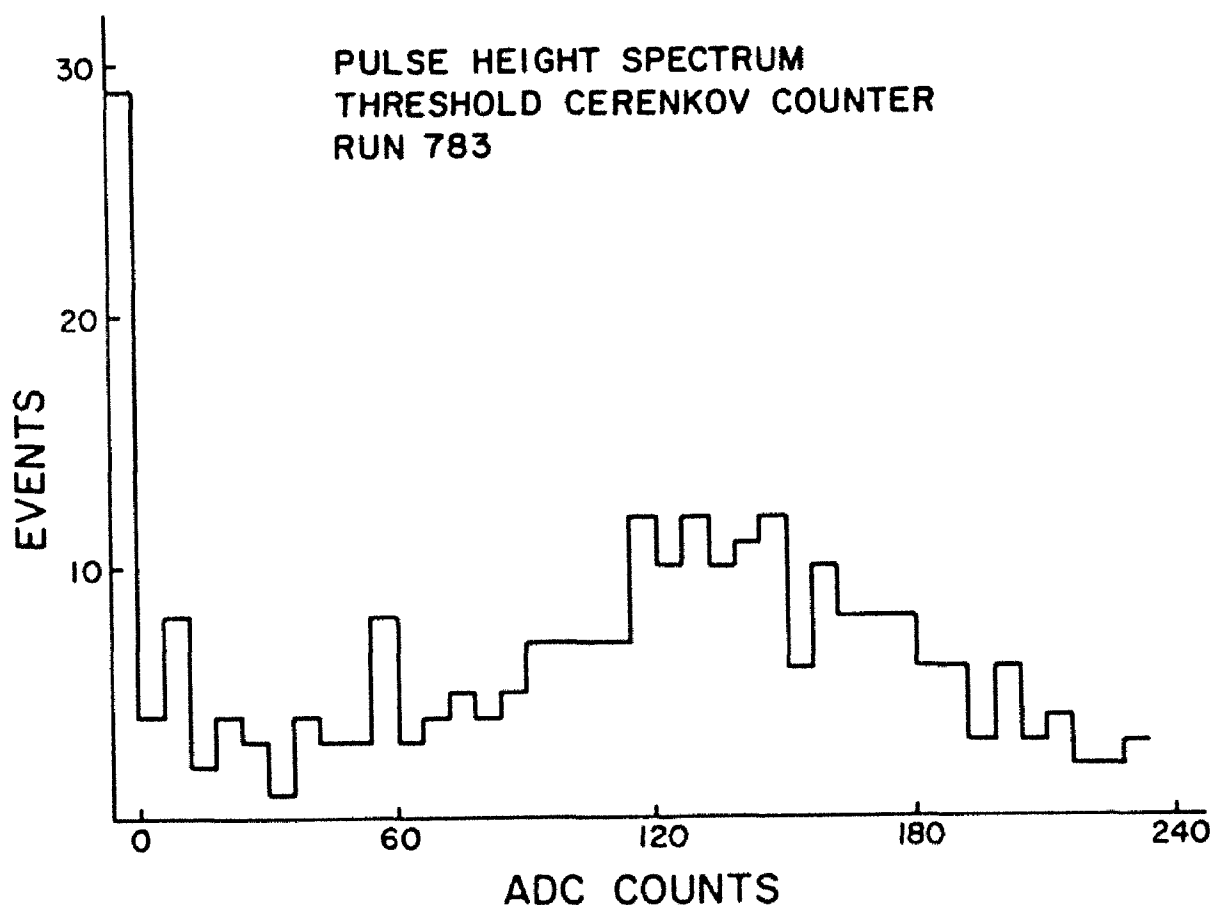


Figure 20: Pulse Height Spectrum in Threshold Cerenkov Counter

UNCORRECTED PULSE HEIGHT FOR PIONS
IN DIFFERENTIAL CERENKOV COUNTER

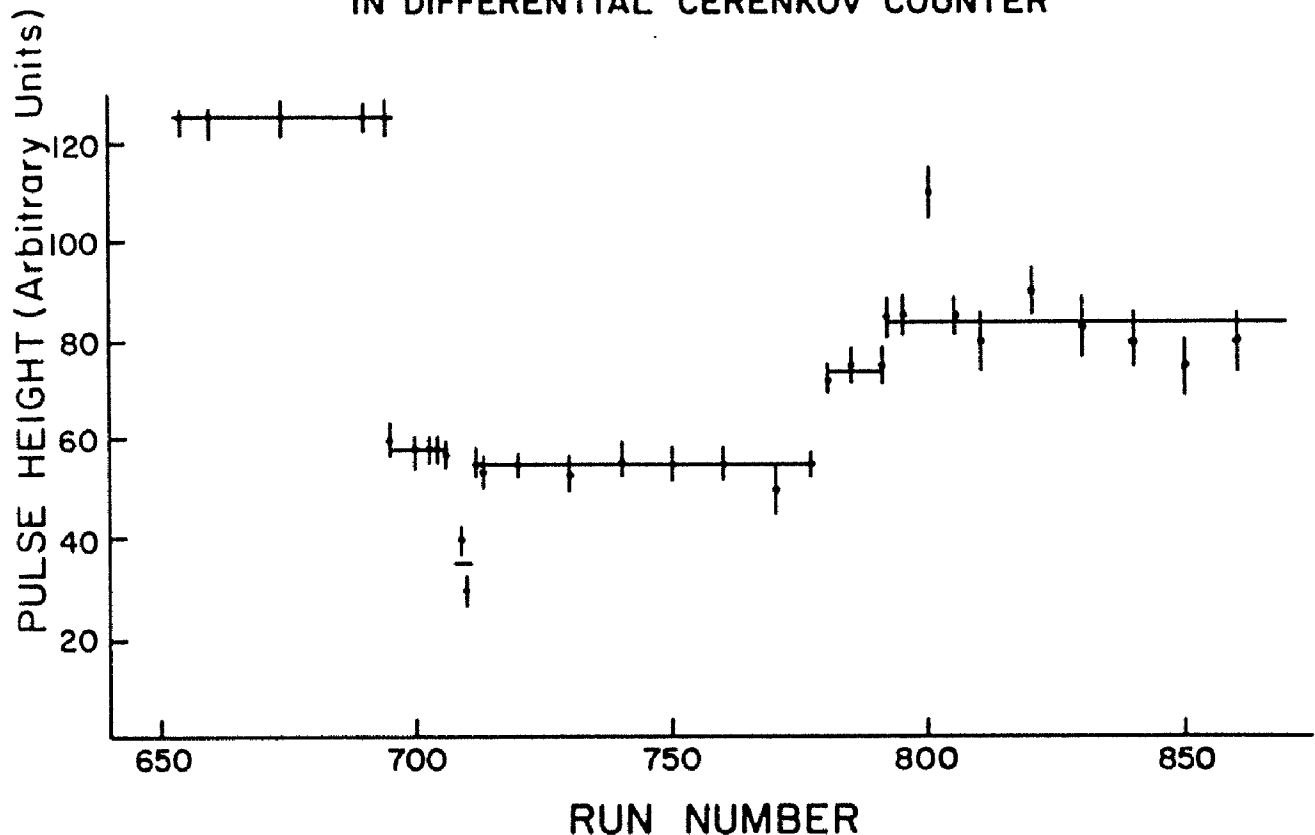


Figure 21: Variation in Phototube Calibration

Using the normalized signals, consistent plots of average pulse height versus momentum for each particle type could be made. Figure 22 shows such a plot for the CO₂ counter. Also shown is the threshold value used in identifying pions.

Figure 23 shows the pulse height versus momentum for kaons in the differential counter. Note that as the momentum increases from threshold, and with it the Cerenkov angle, the amount of light reaching the inner tube rises quickly and saturates, while the signal in the outer tube continues to rise far beyond the momentum threshold. A study of the performance of this counter⁶¹ using data from our previous experiment

⁶¹ R. Cester, V.L. Fitch, A. Montag, S. Sherman, R.C. Webb, M.S. Witherell, "Results on the Performance of a Broad Band Focusing Cerenkov Counter", IEEE Transactions on Nuclear Science. Vol. NS-28,1981,p425.

PIONS IN THE THRESHOLD CERENKOV COUNTER

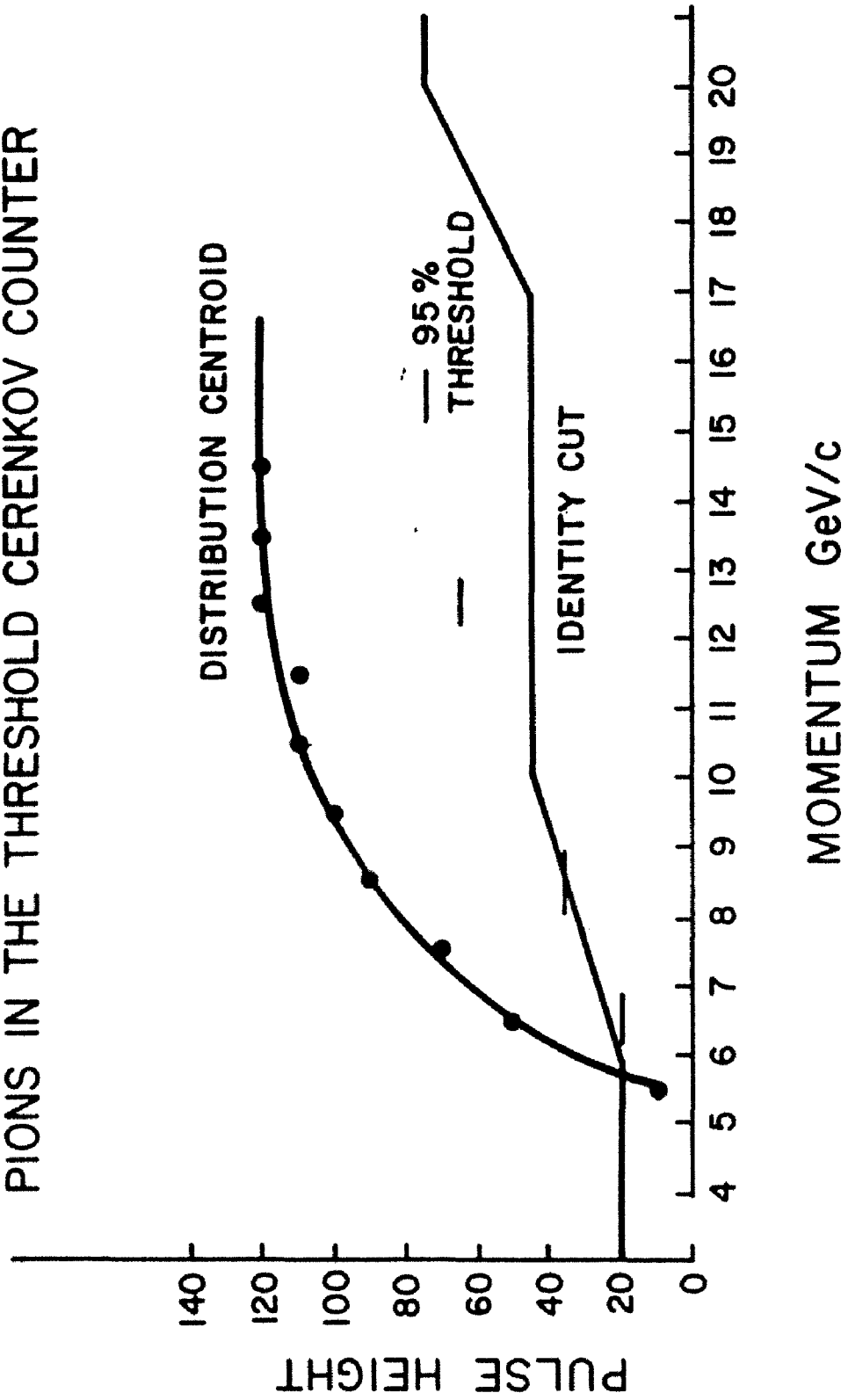


Figure 22: Excitation Curve for Threshold Cerenkov Counter

concluded that near the momentum threshold the most practical quantity to use in particle identification is the sum of the inner and outer signals, that is to use the counter in the threshold mode, as had been done previously. Well above the momentum threshold, however, where the signal from the inner tube has saturated, using the outer tube alone gives a greater sensitivity to particle velocity.

In our experiment the presence of the CO₂ counter made use of the differential information superfluous in the separation of pions and kaons. Nonetheless, the differential information was used as a check on the threshold counter in the analysis program. The differential information made its principal contribution in tagging kaons that were of higher momentum than the proton Cerenkov threshold (18.5 GeV/c) in isobutane. As illustrated in Figure 24 taken from the analysis performed in the preparation of reference 61, this extended our confidence in kaon identification from 20 GeV/c to over 25 GeV/c.

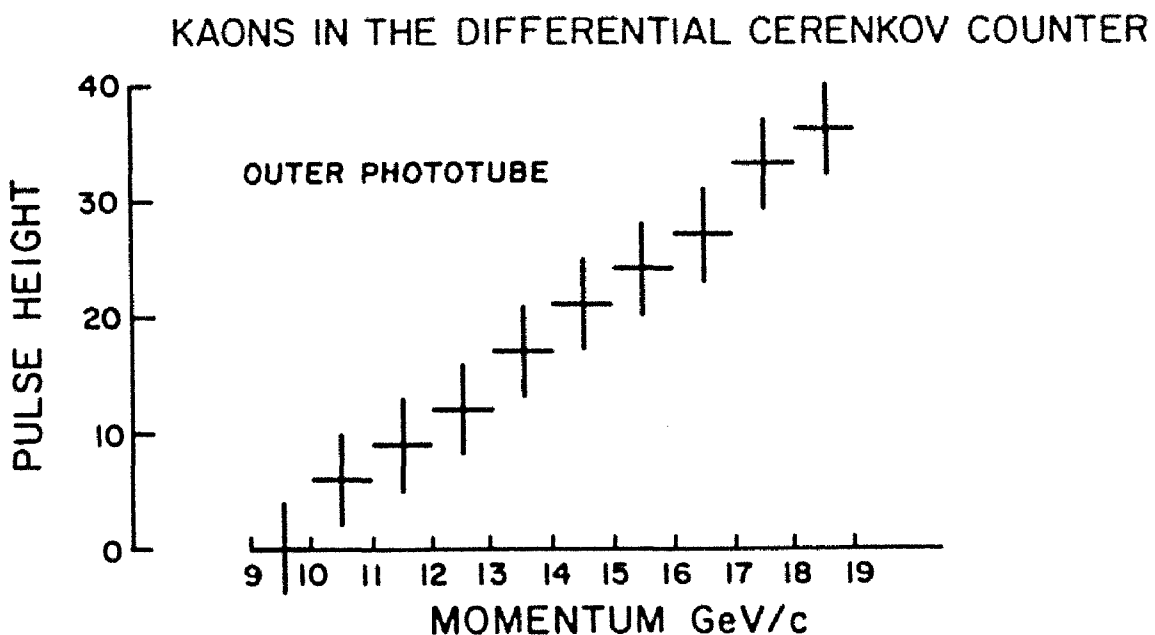
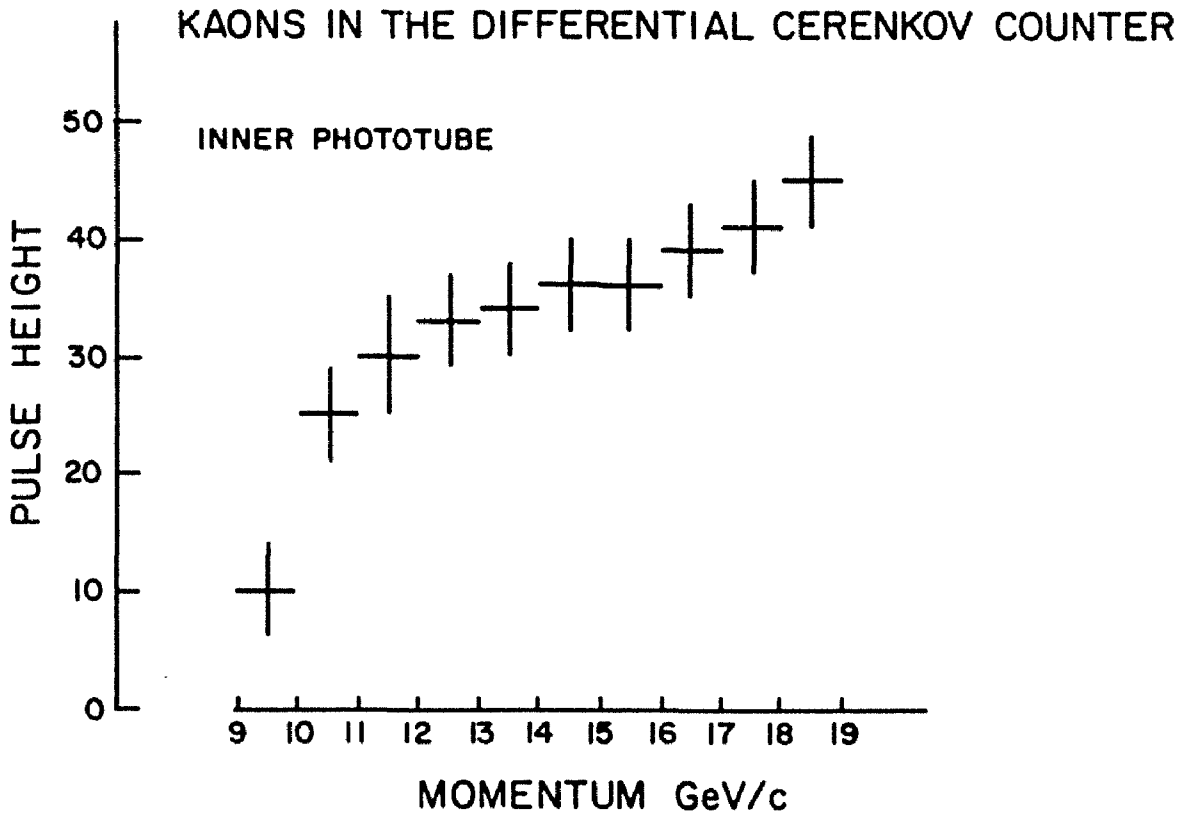


Figure 23: Kaons in the Differential Cerenkov Counter

Fraction of Protons that are Misidentified as Kaons when the Kaon Threshold is set to Catch 90% of the Kaons:

PROTON FEED THROUGH

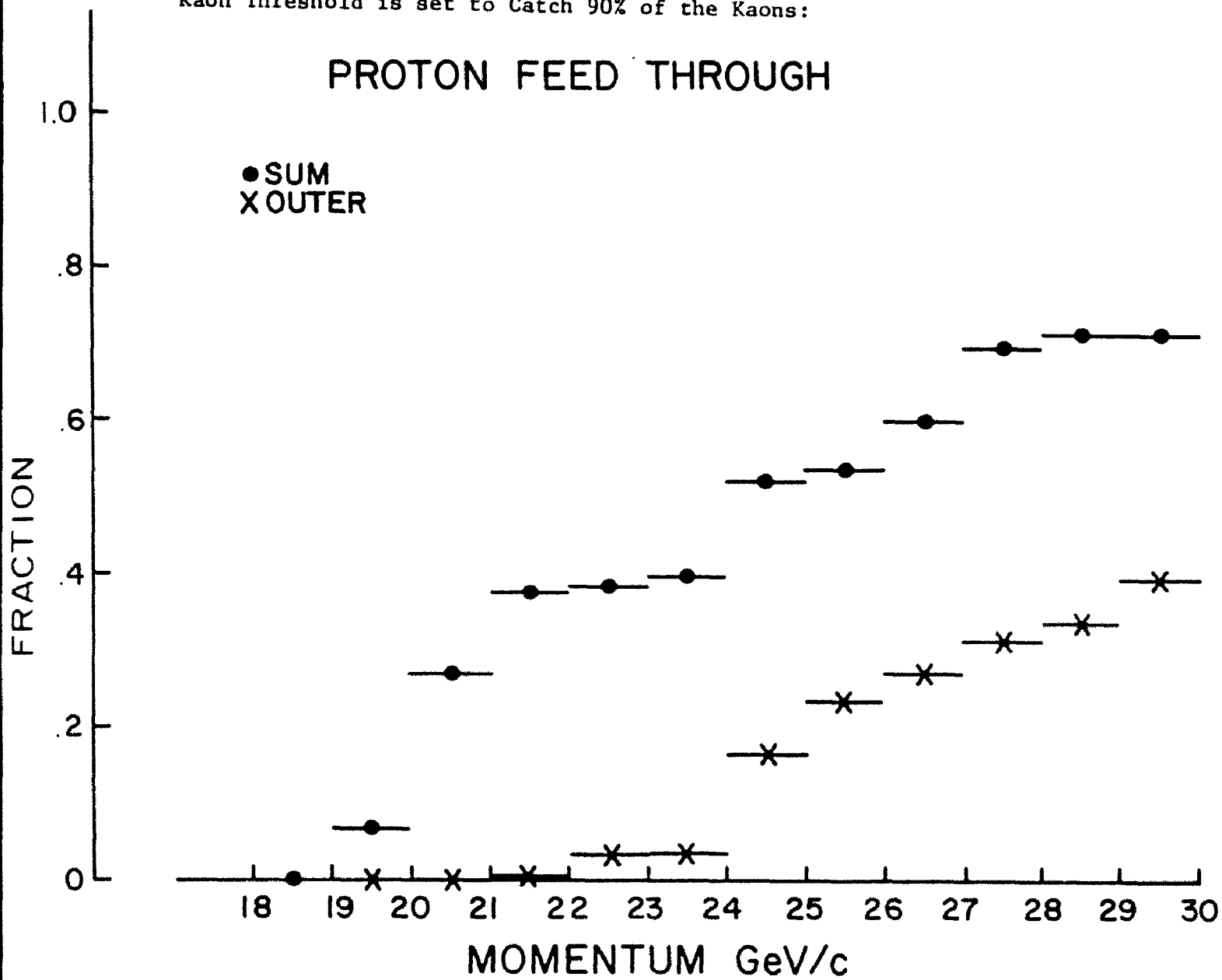


Figure 24: Proton Feed-Through in the Differential Cerenkov Counter

3.4 FAST ARMS MOMENTUM AND MASS CALCULATION

Beginning with the right arm, the secondary analysis program made use of the tilted FII hodoscope, which was not in the trigger, to check the matching of the bending plane with the non-bending plane tracks for events having more than one reconstructed track in an arm. Of the 2 percent of events having two tracks, 24 percent required reordering. The number of hits in the bending plane determined the track priority. In all subsequent analysis only the first track in an arm was used.

The y slopes as transmitted from the primary program were used to calculate the bend center in the BM109. This was done by constructing the circle whose tangents at the ends of the magnet field matched the before and after magnet bend plane slopes, and finding the intersection of the two tangents. A small correction was made in the x track slope to fix the relative arm alignment so that both fast arms would point back to the same z vertex value.

The momentum was calculated using a value for the field integral that depended on the position of the track inside the magnet. The field integrals and correction functions are presented in Table 7. The values used in fitting the corrections were based on measurements made using a 20 foot flip coil before the run of the last experiment. The overall asymmetry in the right and left fields was determined immediately after the present running period, with magnets in place and at the nominal running current, using a hand made ten foot flip coil which gave repeatable results to within .4 percent. The mass at the J/ψ peak provided a further check on the magnitude of the sum of the two fields.

At this stage the particle was identified by means of the algorithm described in Section 3 above. For the low momentum, ambiguous, non-pion

TABLE 7
Magnetic Field Parameters

	Henry Higgins	BM109	
		Left	Right
$\int B dl$ (GeV/c)	.420	.643	.652
BM109 position correction = $.5 [C(x_1, y_1) + C(x_0, y_0)]$			
$C(x, y) = 1 - B \cosh(y/A) \cos(x/A)$			
		Right	Left
A		2.294	2.020
B		$.8 \times 10^{-3}$	$.333 \times 10^{-3}$

events both identity choices were recorded, and the decision was made which to keep when the pair masses were accumulated into histogram bins.

Next, the track was projected through the Henry Higgins magnet. The calculated change in the y slope was made to take place 1.6 inches upstream of the geometric center of the magnet in conformity with plots of the magnetic field. The shift is due to the absence of iron shielding for flux return at the upstream end of the magnet. The kink in the y track also led to a small correction in the x track slope. The whole process was then repeated for the left arm.

The fast spectrometer analysis continued with the determination of the z value of the intersection of the two non-bending plane tracks. The z of the vertex of the event was defined to be the z at the center of the target piece closest to the two track intersection. The x and y values of the vertex were defined to be the averages of the two values from each arm, with a small extra weight given to tracks having signals in the furthest upstream drift chambers.

The slopes and intercepts of the non-bending plane tracks were then recalculated using the original particle intersections with the chamber planes but subject to the additional constraint that the tracks in the two arms meet at the defined z vertex. The errors due to ignoring the Henry Higgins magnet in this refit were measured to be a few tenths of an MeV in the two body mass in the J/ψ region.

The y tracks were left as they were, thereby providing two variables for vertex cuts:

$$D_{yrl} = Y_{ztgr} - Y_{ztgl}$$

and
$$Y_{tg} = Y_{rl} - Y_{targ}$$

where Y_{targ} is the y value at the center of the assigned target piece. Requiring the absolute value of D_{yrl} to be less than .5 inches and the absolute value of Y_{tg} to be less than .25 inches eliminated 54 percent of the events on a DST, but retained an estimated 77 percent of events originating from single vertex interactions.

The x and y slopes were used to calculate the three direction cosines for each particle. Using the direction cosines, momentum magnitude, and rest mass, a Lorentz four-vector for each particle was constructed. In the slow arms a four-vector was also constructed, but every track was assumed to come from a pion. The two and three body masses were calculated by the appropriate addition and squaring of these vectors.

3.5 MOMENTUM AND ANGLES IN THE SLOW ARMS

Because the fast spectrometer arms could point back to the target with greater accuracy than could the chambers in the slow pion spectrometer, the vertex used in the calculation of the momentum and angles in the slow arms was found in the forward spectrometer portion of the anal-

ysis. The geometrical constructions that mated this vertex with the track found downstream of the Henry Higgins magnet were complicated by the extension of the target well into the upstream fringe field making the total field integral, or equivalently the transverse momentum kick, dependent on the target piece in which the interaction occurred. To a lesser extent the field integral also was dependent on the path of the particle downstream of the magnet center. That is, the total field integral a particle experienced also depended on its momentum. These vertex and momentum dependent corrections were incorporated, of necessity, by performing the slow arm calculations iteratively.⁶²

The calculations began by taking the slope of the track in the non-bending plane and in the bending plane downstream of the magnet from the fits to the drift chamber signals as provided by the track reconstruction program. The first modification was a shift in the non-bend intercept at the geometric center of Henry Higgins, which was the origin of the coordinate system for the slow pion track reconstruction, that was introduced in order to align the slow arms with the fast arms.

The track reconstruction program provided no useful value for the y slope upstream of the bend in the magnet. What it did provide was the value of x and y at the track bend kink point crudely taking into account the shift in the midpoint of the field integral due to the bowing of the magnetic field lines at the downstream end of the magnet. The secondary analysis program defined the prebend slope to be the slope of the line defined by the bend center and by the vertex as found in the fast arms.

⁶² The high momentum of the particles in the fast arm made these effects negligible there.

The two bending plane slopes were then used to recalculate the bend center by the same method of matching a circle to two tangents that was used in the fast arms, with an additional shift upstream in z of 1.3 inches corresponding to the average deviation of the magnetic field integral center from the magnet's geometric center for tracks in the slow arms. The new z and the corresponding y, found using the measured downstream slope, were used to recalculate the prebend y slope. The first iteration ended with the computation of a provisional momentum using the slopes as just described and the average value of the transverse momentum kick.

By tracing hypothetical tracks of known momentum through a map of the magnetic field of Henry Higgins made using a Hall probe, the values of z at the track kink and the total transverse momentum kick were parameterized as functions of the z value at the vertex and the slow particle momentum. The values of the fast arm vertex and the provisional momentum were put into this function, and the final prebend slope was calculated.

A correction was also applied to the slope in the non-bending plane to account for the focusing effect induced by the fringe field of the magnet. The correction was:

$$\Delta\theta_x = (P_{HR}/P_{\pi})^2 \theta_x (1 + 30)/l_{off}$$

where θ_x is the uncorrected x slope, 1+30 is the distance in inches from the target to the kink point in the non-bend plane, and l_{off} is the effective length of the magnetic field. The correction was applied so that the new slope would always be at a greater angle from the beam than the original.

The corrected slope was projected from the kink point back to the x of the vertex, and the difference between that x value and the x from the fast arms was used as the vertex cut variable. Cutting at a difference of 0.5 inches preserved about 85 percent of the good events.

The track was also projected to a point 90 inches downstream of the magnet center, roughly at the middle set of the tilted slow arm chambers. The official slope in the non-bending plane in the slow arms was defined to be that of the line passing through the fast arm vertex and that projected point. This definition represented a compromise between the measured slope and the borrowed vertex. This new θ_x , along with the final prebend y slope, the original measured post bend y slope, and the calculated transverse momentum kick were at last used to calculate the slow particle momentum and the direction cosines used in constructing the slow pion Lorentz four-vector.

The Q value for each event was calculated by subtracting the mass of a pion and the two body mass from the fast arms from the three body mass. Use of the measured two body mass, rather than the D^0 mass helped to maximize the orthogonality of the Q value and fast arm mass measurements.

Studies of the effects of the event dependent set of corrections show an average change in the x slope of about 2 milliradians and a change in the slow pion momentum of the order of 2 percent. In each case the deviation corresponds to a change in the result of the Q value calculation of events in the region of the D^0 of about 0.5 MeV, an amount comparable to the total uncertainty in the Q value resolution.

3.6 Q VALUE RESOLUTION

The error in the measurement of the Q value for the D^0 decay is dominated by the uncertainties in the slow pion arms. This is a result of both the strong dependence of Q on the kinematics of the slow pion alone and the greater precision of momentum and angle measurements in the forward spectrometer which is due to the longer lever arms.

The quantities actually measured in the slow arms are the bending and non-bending plane slopes of the tracks downstream of the magnet. The momentum is determined as a function of these slopes and is therefore not an independent variable for the purposes of error estimation. Two other independent parameters which must be accounted for are the error in the angle induced by multiple scattering in the target and the uncertainty in the field of the magnet due to drifts in the current.

By taking the appropriate derivatives, the expected error in Q for a given event can be expressed as a function of these variables:

$$\begin{aligned} \Delta Q(\theta_x, \theta_y, \theta_{ms}, p_{HH}) &= \left[\left(\frac{\partial Q}{\partial p_{HH}} \frac{\partial p_{\pi}}{\partial \theta_y} + \frac{\partial Q}{\partial \theta_y} \right)^2 \Delta \theta_y^2 + \left(\frac{\partial Q}{\partial \theta_x} \right)^2 \Delta \theta_x^2 \right. \\ &\quad \left. + \left(\frac{\partial Q}{\partial \theta} \right)^2 \Delta \theta_{ms}^2 + \left(\frac{\partial Q}{\partial p_{\pi}} \frac{\partial p_{\pi}}{\partial p_{HH}} \right)^2 \Delta p_{HH}^2 \right]^{1/2} \end{aligned} \quad (3.1)$$

The D^0 mass can be expressed as with the information on the D^0 being the vector sum of the

$$M_{D^0}^2 = (E_{\pi} + E_D)^2 - (p_{\pi}^2 + p_D^2 + 2p_{\pi}p_D \cos\theta) \quad (3.2)$$

kaon and fast pion measurements and θ here standing for the angle between the D^0 and the slow pion. Keeping in mind that the D^0 mass and the Q value in principle differ by a constant, the appropriate coefficients in Equation (3.1) can be determined:

$$\frac{\partial M}{\partial \theta}(x,y) = \frac{\partial Q}{\partial \theta}(x,y) = \frac{p_{\pi} p_D \sin \theta}{M_D^*}(x,y) \quad (3.3)$$

$$\frac{\partial M}{\partial p_{\pi}} = \frac{\partial Q}{\partial p_{\pi}} = \left(\frac{E_{\pi} p}{E_{\pi}} - p \cos \theta \right) / M_D^* \quad (3.4)$$

From the formula used to calculate momentum:

$$p_{\pi} = P_{HH} / (\sin \theta_{yout} - \sin \theta_{yin}) \cos \theta$$

we get to first order in angle

$$\frac{\partial p_{\pi}}{\partial \theta_y} = \frac{p^2}{P_{HH}} \quad \text{and} \quad \frac{\partial p_{\pi}}{\partial P_{HH}} = \frac{p}{P_{HH}}$$

We next proceeded to estimate the errors on the independent parameters. The current through Henry Higgins monitored throughout the run had a fluctuation of 1 out of 780 amperes, or 0.13 percent for $\Delta P_{HH}/P_{HH}$. Assuming that the average slow pion traversed half a target thickness

$$\Delta \theta_{ms} = 2.02 \times 10^{-3} / p(\text{GeV}/c) .$$

To find the errors in the measured angles one needs the information on the goodness of fit of the hits in the drift chambers and on the uncertainty in the vertex determination. For θ_x the error was defined to be the mean standard deviation of the fit to the slope of a line using one point in each of the three drift chambers, each of which having an uncertainty of 0.012 inches, as determined from a plot of the fit residuals, and a fourth point at the target assigned to the interaction with

an uncertainty in x of 0.24 inches corresponding to the width of the distribution of up or down vertex versus right and left. The result is

$$\Delta\theta_x = 1.25 \times 10^{-3} .$$

In the bending plane slope calculation no single fit is ever made that combines the chamber and vertex information. Consequently, the error in the slope was taken to be the sum, in quadrature, of the error in fitting the chamber hits and the uncertainty in the position of the y vertex, 0.1 inch, divided by the average distance from the target to the magnet center, 60 inches. This yielded

$$\Delta\theta_y = 1.7 \times 10^{-3} .$$

The average ΔQ in the mass and Q region of interest is about 0.6 MeV. In plotting the two body masses we found it convenient to cut on ΔQ , event by event, that is on the quantity

$$R = |Q - Q_{exp}| / \Delta Q$$

in addition to the usual window around the expected Q value of 5.7 Mev.

3.7 RESOLUTION IN THE FAST ARMS

The principal factors contributing to the resolution width in the fast arms are, in decreasing size order, the error in measuring the bend angle in a BM109 arising from the uncertainty in the measured slopes, multiple scattering of the pion and kaon in the target, uncertainty in the relative alignment of the spectrometer arms, and fluctuation of the current in the magnets.

To estimate the magnitude of each of these contributions, we proceed as we did in the last section. By changing the subscripts D^* , D^0 , and π to D^0 , π , and K respectively in Equations (3.2), (3.3), and (3.4), we get the formulas for the D^0 mass and its derivatives provided we inter-

pret θ as θ_{op} , the opening angle of the fast particle pair at the vertex, and θ_y as the change in the angle of either particle due to the kick in the BM109.

$$M_D^0 = (E_K + E_\pi)^2 - (p_K^2 + p_\pi^2 + 2p_K p_\pi \cos\theta)$$

$$\frac{\partial M}{\partial p_{(\pi, K)}} = \left[\frac{E_{(K, \pi)} P_{(\pi, K)} - p_{(K, \pi)} \cos\theta}{E_{(\pi, K)}} \right] / M_D^0$$

$$\frac{\partial M}{\partial \theta} = p_\pi p_K \sin\theta / M_D^0$$

The calculation of the average error in mass is greatly simplified if the momenta in the two fast arms are taken to be equal. Omitting terms of fourth order and beyond in m/p where m is the pion or kaon mass, the expression for the mass resolution reduces to

$$\Delta M = \left[2(1-\cos\theta)^2 (p/M)^2 (p/p_{mag})^2 \Delta\theta_y^2 + 2(1-\cos\theta)^2 (p/M)^2 (p/p_{mag})^2 \Delta p_{mag}^2 + 2(p^2 \sin\theta/M)^2 \Delta\theta_{ms} + (p^2 \sin\theta/M)^2 \Delta\theta_{op}^2 \right]^{1/2}$$

where M is the mass of the πK pair. The leading factors of two in the first three terms are the result of summing over the two symmetric fast arms. The last term accounts for the alignment matching of the arms and only appears once.

The error in measuring the slopes, $\Delta\theta_y$, was calculated using .028 inches for chamber resolution and assuming that one intermediate chamber was missing from the track upstream of the magnet and one downstream of the magnet. That is, the whole lever arm is retained, but two hits are missing. As in the slow arm, this information was taken from a plot of fit residuals and number of hits in a track using the data sample from which the final mass plots were generated.

The number used for chamber resolution is essentially a measure of the contribution of multiple Coulomb scattering in the matter along the spectrometer arms. This contribution dominates over both the wire position measurement error and the drift timing precision. Combining the slope errors before and after the magnet yields a result of $\Delta\theta_y = 4.1 \times 10^{-4}$ in each arm. This translates to a

$$\Delta p/p = p \times 6.3 \times 10^{-4} .$$

The fluctuation in the transverse momentum kick of the BM109s, based on the monitored current fluctuations, was 0.041 percent and turned out to be a negligible contribution to the final result. The multiple scattering contribution, as in the slow arms assuming each particle traverses half a target, is

$$\Delta\theta_{ms} = 2.03 \times 10^{-3}/p \text{ (GeV/c)} .$$

The error in opening angle was taken to be 0.3 milliradians which represents the shifts in the alignment from the nominal 150 milliradian opening angle that were introduced in order to center the vertex distributions.

Collecting all of the terms and putting in the numbers, the expression for the fast spectrometer mass measurement error as a function of the mass and average momentum becomes:

$$\Delta M(p, M) = \left[p^6 (1.01 \times 10^{-10}) + p^4 (4.06 \times 10^{-9}) + p^2 (1.83 \times 10^{-7}) \right]^{1/2} / M .$$

For the D^0 , with $p_{av} = 12$ GeV/c and $M = 1.863$ GeV, $\Delta M = 11$ MeV, of which 9 MeV is due to the first term which represents the error in the measurement in the bend angle through the BM109. For the J/ψ , with $p_{av} = 20$ GeV/c and $M = 3.097$ GeV, $\Delta M = 27$ MeV, of which 26 MeV is due to the momentum measurement uncertainty. The J/ψ calculated width is compati-

ble with our observed J/ψ distribution (the central 14 events have a standard deviation of 25 Mev) but the small sample renders a conclusive comparison impractical.

Chapter IV

RESULTS

4.1 THE J/ψ Signal

Observing the decay

$$J/\psi \rightarrow \mu^+\mu^-$$

gave us an opportunity to check the calibration of our apparatus against a well measured signal comparably small to the one we sought while running under normal conditions. The dimuon mass spectra for the 250 GeV/c run is plotted in Figure 25. Assuming that the accidental dimuon background, which arises from the muon halo of the beam and from π and K decay, is of the same magnitude for both like sign and opposite sign pairs, there is an excess over the background of 14 ± 4 events in the opposite sign spectrum in the region of the J/ψ mass.

To translate this signal to a cross section, J/ψ production was assumed to proceed according to the distribution

$$\frac{dN}{dx} \propto (1 - |x|)^{1.65}$$

where the choice of exponent was taken from the best fit of the Chicago-Illinois-Princeton data.⁶³ The sensitivity was calculated by taking the product of the total number of interactions in the target, the geometric detection efficiency of the spectrometers, and the various data acquisition and analysis efficiencies and dividing by the total hadronic cross section for the beam-target interaction at the running energy. The values used are presented in Table 8. The sensitivity of the 250 GeV/c

⁶³ G.E. Hogan, Ph.D. Thesis, Princeton University, 1979 (unpublished). See also the next reference.

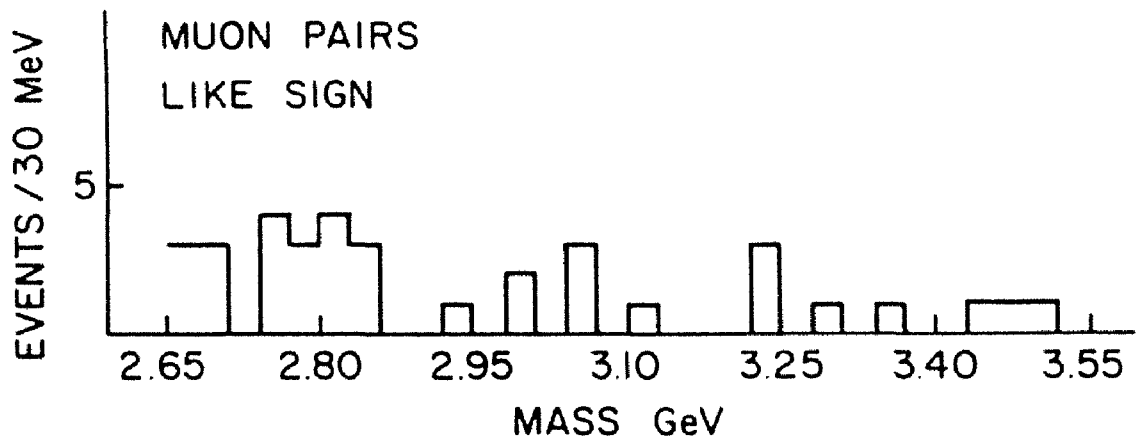
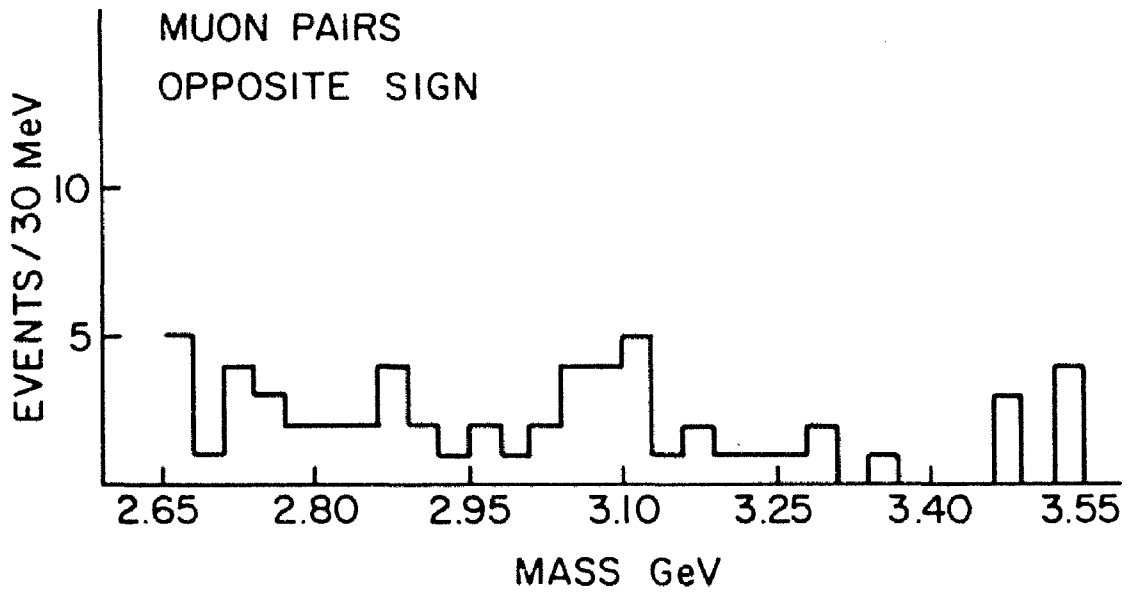


Figure 25: Muon Pair Masses 250 GeV/c Run

data sample for J/ψ was

$\sigma(J/\psi)xB_{\mu\mu} = 1.07$ events/nanobarn/nucleon. We assume a linear dependence on atomic number. The error in the sensitivity is about 15 percent and is dominated by the error in the beam flux normalization.

TABLE 8
Sensitivity for J/ψ

Number of incident pions	6.68×10^{12}
Number of beam-target interactions	1.2×10^{11}
Total cross section/nucleon	25 mb
Geometric acceptance of spectrometer	7.52×10^{-4}
Efficiencies	
Data Acquisition	
Trigger hodoscopes	.95
Muon counters	.85
Counter placement	.93
Reconstruction	
Track recovery	$(.71)^2$
Vertex rejection	.77
Sensitivity for $\sigma(J/\psi)xB_{\mu\mu} = 1.07$ events/nb	

The measured J/ψ cross section is therefore

$$\sigma x B_{\mu\mu} = 13.1 \pm 4.7 \text{ nanobarns/nucleon}$$

where the quoted error is purely statistical. With $B_{\mu\mu} = 7$ percent:

$$\sigma(J/\psi)_{\text{tot}} = 187 \pm 67 \text{ nanobarns/nucleon.}$$

The CIP group reports a cross section for $x > 0$ of

$$\sigma x B_{\mu\mu} = 88 \pm 12 \text{ nanobarns/C}^{12} \text{ nucleus}$$

for 225 GeV/c incident pions.⁶⁴ Again assuming a linear A dependence, and multiplying by two to include all values of x they get

$$\sigma x B_{\mu\mu} = 14.7 \pm 2 \text{ nanobarns/nucleon}$$

in reasonable agreement with our result.

⁶⁴ K.J. Anderson, *et al.*, Phys. Rev. Lett., 42, 944 (1979).

A similar treatment, applied to results from the SPS,⁶⁵ yields

$$\sigma_{\text{xB}_{\mu\mu}} = 13.4 \pm 1.7 \text{ for } 200 \text{ GeV/c } \pi^- \text{'s}$$

and $\sigma_{\text{xB}_{\mu\mu}} = 14.8 \pm 3.4 \text{ nbarn/nucleon for } 280 \text{ GeV/c } \pi^- \text{'s.}$

Because the overall normalization of the 200 GeV/c beam flux was constrained to agree with the CIP result for J/ψ production, we have no independent J/ψ production measurement at 200 GeV/c. In order to compare our 250 GeV/c results with our 200 GeV results, which are plotted in Figure 26, the ratio of sensitivities must be calculated. The 250 GeV/c data has .5 the sensitivity for the J/ψ of the 200 GeV/c data. The contributions to the calculation are listed in Table 9. Using the same background subtraction method for the 200 GeV/c spectra as was used for the 250 GeV/c data, there are a total of 37 ± 8 events in the peak. Ignoring the expected small rise in cross section with beam energy, the two results differ by 1.1 standard deviations.

⁶⁵ J. Badier *et al.*, *op. cit.*, reference 19.

DI-MUON MASS SPECTRA
200 GeV/c RUN

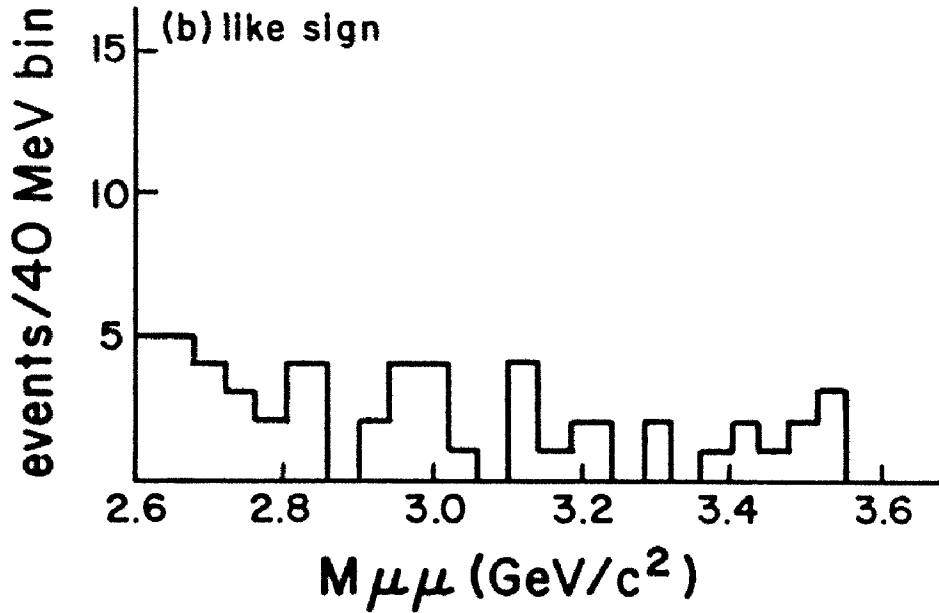
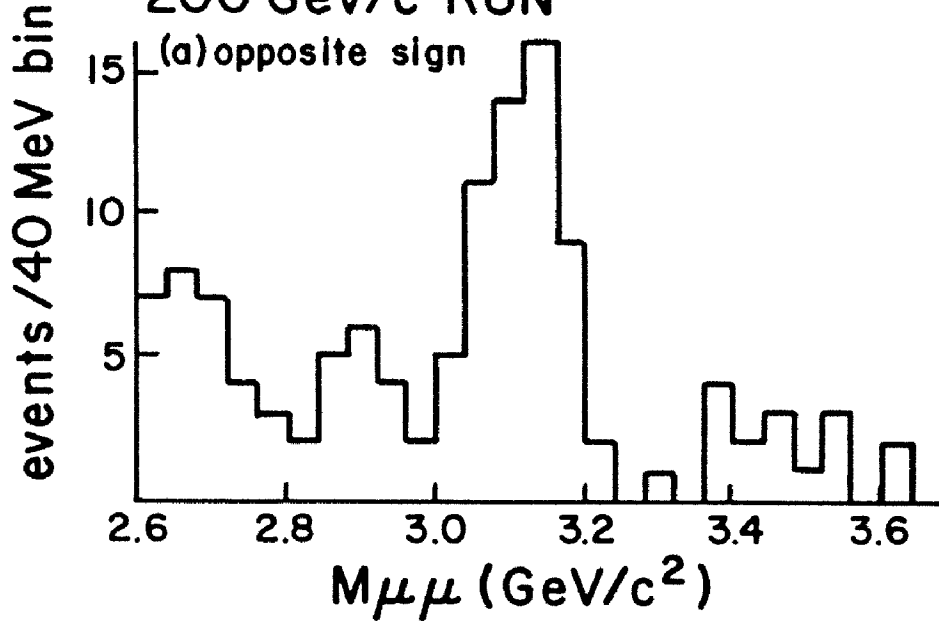


Figure 26: Muon Pair Masses 200 GeV/c Run

TABLE 9

Relative Sensitivity for J/ψ

250 Gev/c run: 200 Gev/c run

Ratio of	
Pions on target	.62
Geometric acceptance	.88
Muon counter placement	.93
Vertex rejection of good events	1.10
Track reconstruction efficiency	.90
	<hr/>
Ratio of sensitivities	.50

4.2 LAMBDA PRODUCTION AND CORRELATIONS

The trigger requirement that one threshold Cerenkov counter be off provided us with a large number of events consisting of two pions and a proton. Of these a significant number contained Λ 's or $\bar{\Lambda}$'s with the decaying into a proton and a slow pion. This signal provided a check on the integration of the fast and slow arms in the analysis as well as an independent check of the mass calibration in the slow arms.

The event sample that was analyzed was selected by choosing only those events in which the fast pion and proton were compatible with having originated within the same target segment, and in which the trajectory of the slow pion intersected that of the oppositely charged proton between 6 and 30 inches downstream of that target. Recall that in this analysis, all particles with momentum below the Cerenkov threshold for isobutane and with no signal in either Cerenkov counter were identified as protons.

The spectrum of Λ and $\bar{\Lambda}$ candidates is plotted in Figure 27. The half width at half maximum of the peak is 3 MeV and the center is at 1.117

GeV, less than 1 MeV from the correct value. If we scale these values by the ratio of the Q values of the D^* and two body decays, the result is a width of 0.45 MeV and a Q normalization error of 0.15 MeV at the D^* .

A determination of the Λ production cross section was not made because of the complications arising from the associated pion required in the trigger. The extra pion does, however, present a unique opportunity. Other groups using double arm spectrometers have studied the various properties of different combinations of hadron pairs, but none have been able to study the $\Lambda \pi$ system. Filtering out the events where the proton - slow pion pair has a mass between 1.11 and 1.12 GeV collects essentially all of the Λ 's. The level of non- contamination is estimated to be less than 40 percent. The sample contains 4608 Λ 's and 2246 $\bar{\Lambda}$'s. Their ratio is equal to the measured production ratio $\sigma(\Lambda)/\sigma(\bar{\Lambda})$ for pions on nucleons at 250 GeV/c.⁶⁶ In figure 28 the mass spectra for the $\Lambda \pi^-$ and $\bar{\Lambda} \pi^+$ pairs are plotted separately. The acceptance was calculated using the same Monte Carlo simulation as was used in the other parts of the experiment. The restriction on the decay path length was put into the acceptance calculation. The mass was allowed to vary, and events were generated in the domain $|x| < .125$, the entire range of acceptance. Figure 29 shows the acceptance for the three body states as a function of mass. The solid line represents the fit to the distribution

$$A(m) = 5.0 \left[1 - e^{-3.8(m - 1.8)^{2.26}} \right] .$$

⁶⁶ See D. Ljung *et al.*, Phys. Rev. D 15, 3163 (1977) and references therein.

$\Lambda^0 + \bar{\Lambda}^0$ CANDIDATES

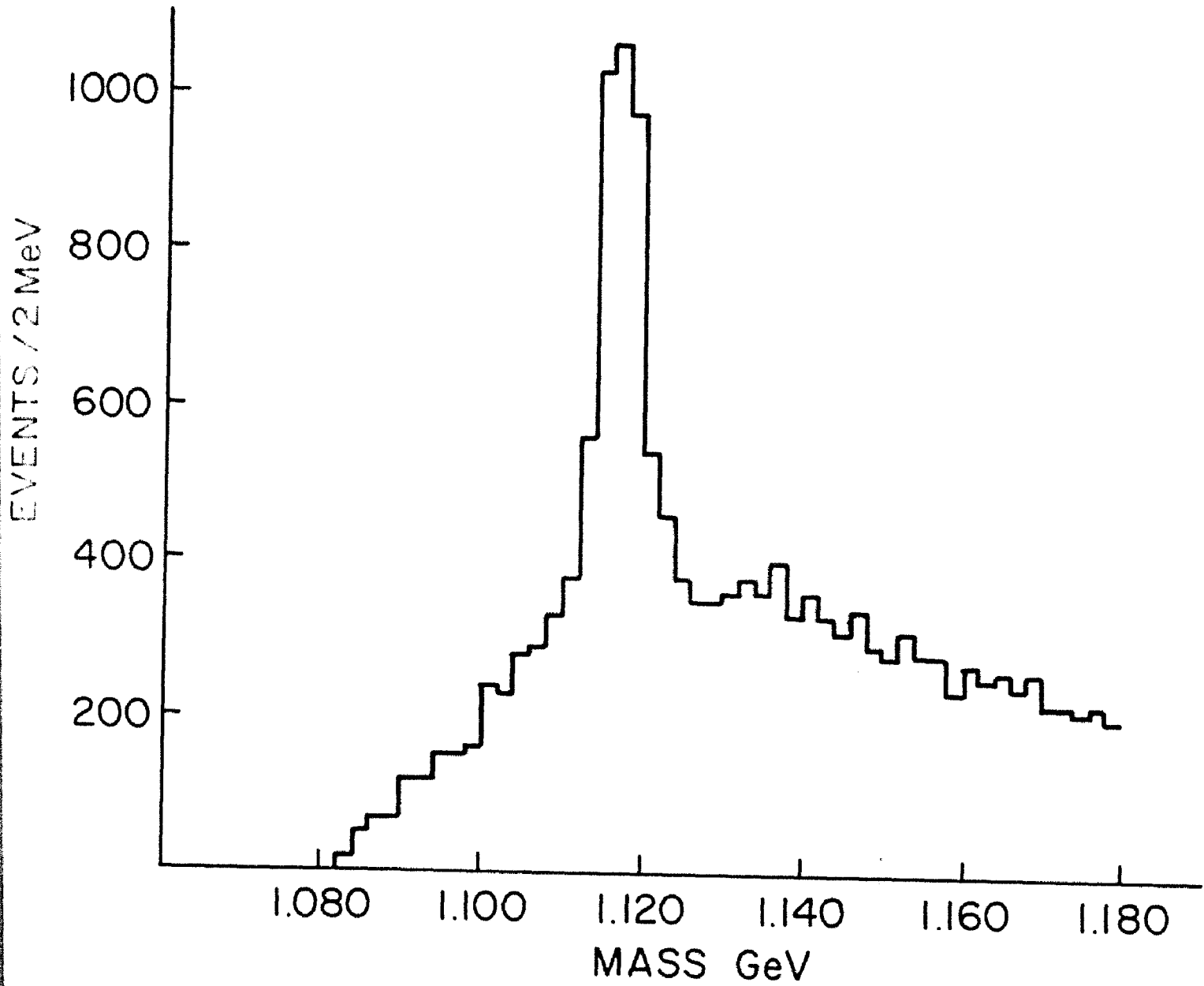
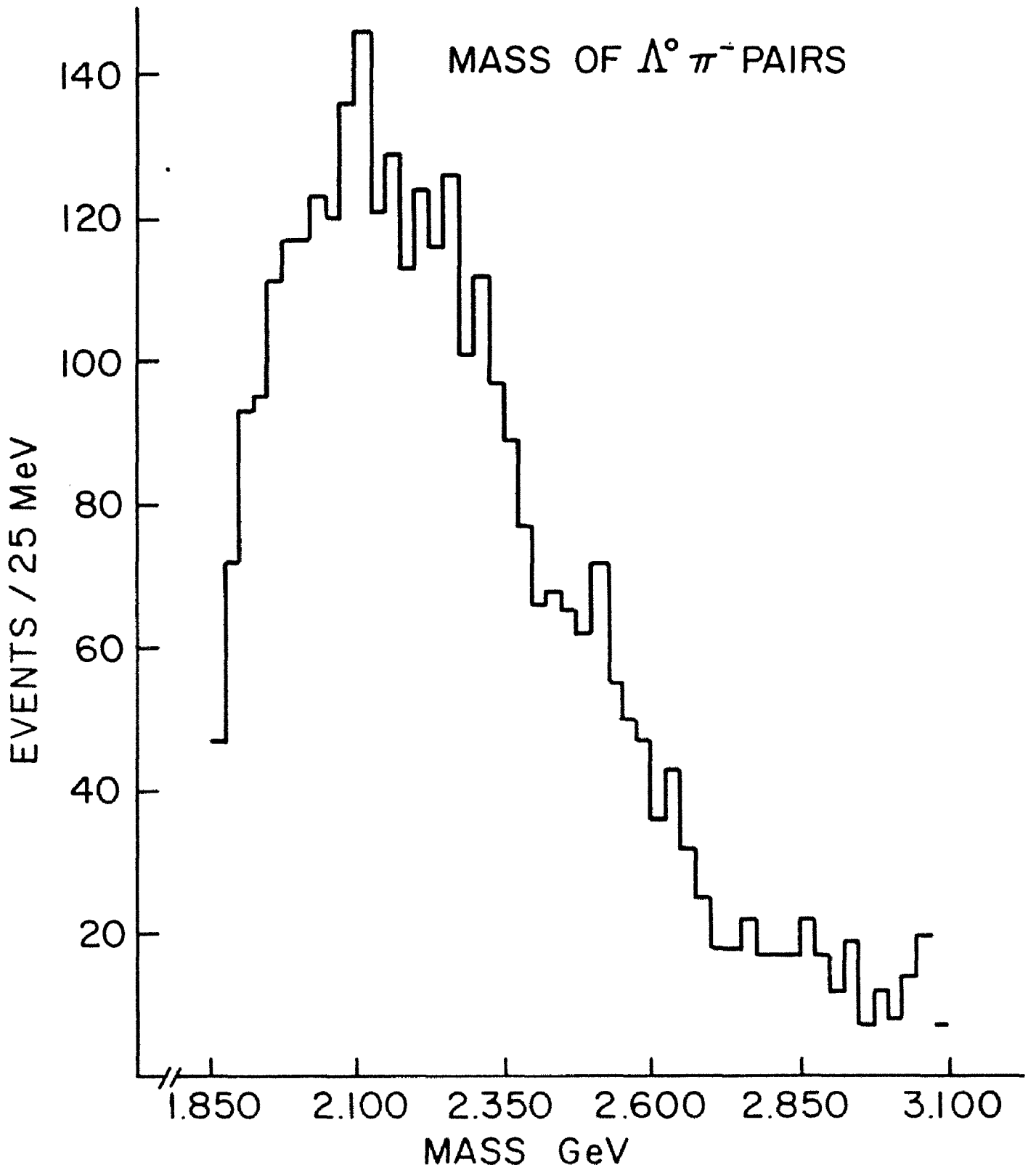


Figure 27: Λ Candidates



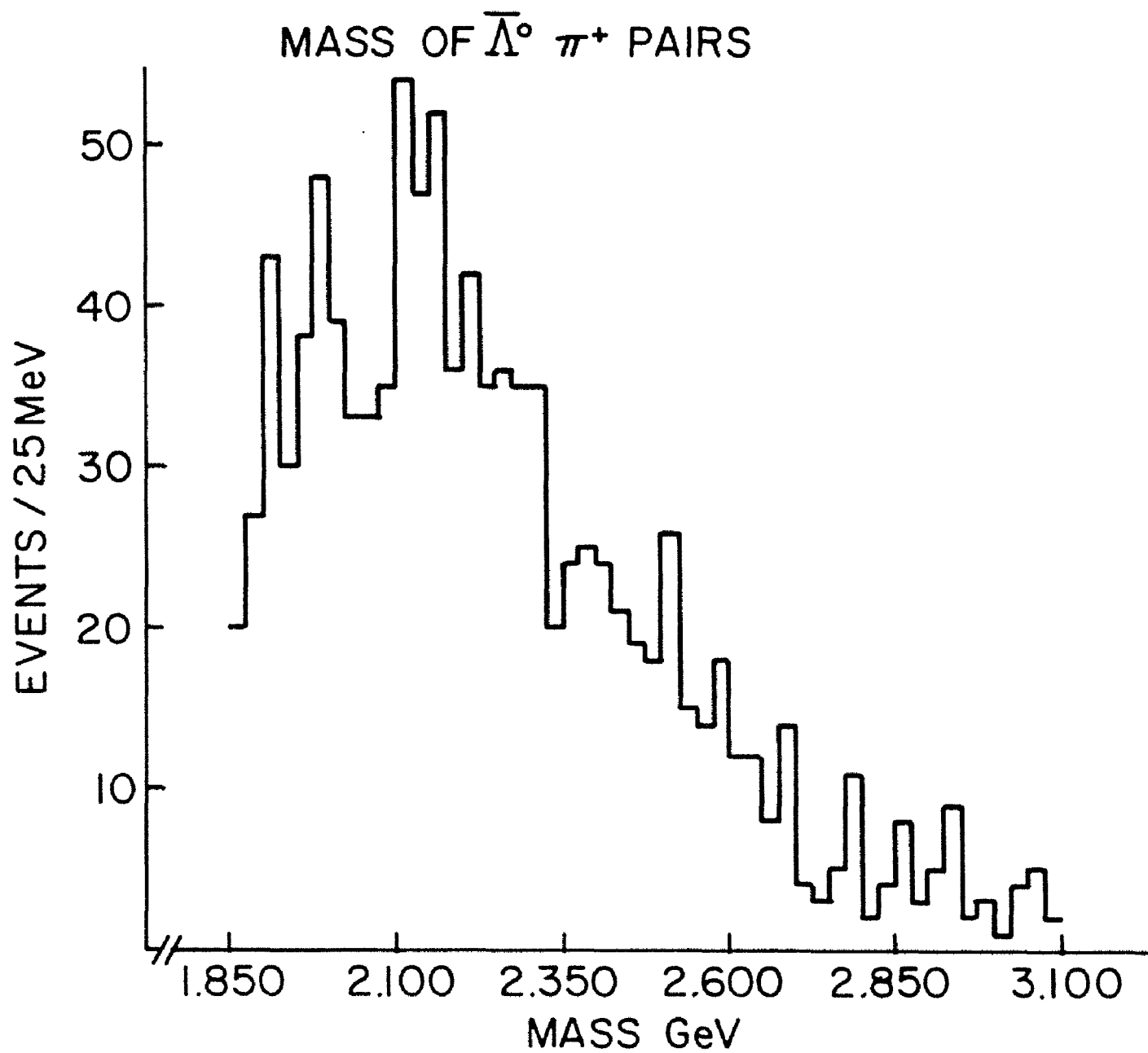


Figure 28: $\bar{\Lambda} - \pi$ Mass Spectra

THREE BODY GEOMETRIC ACCEPTANCE

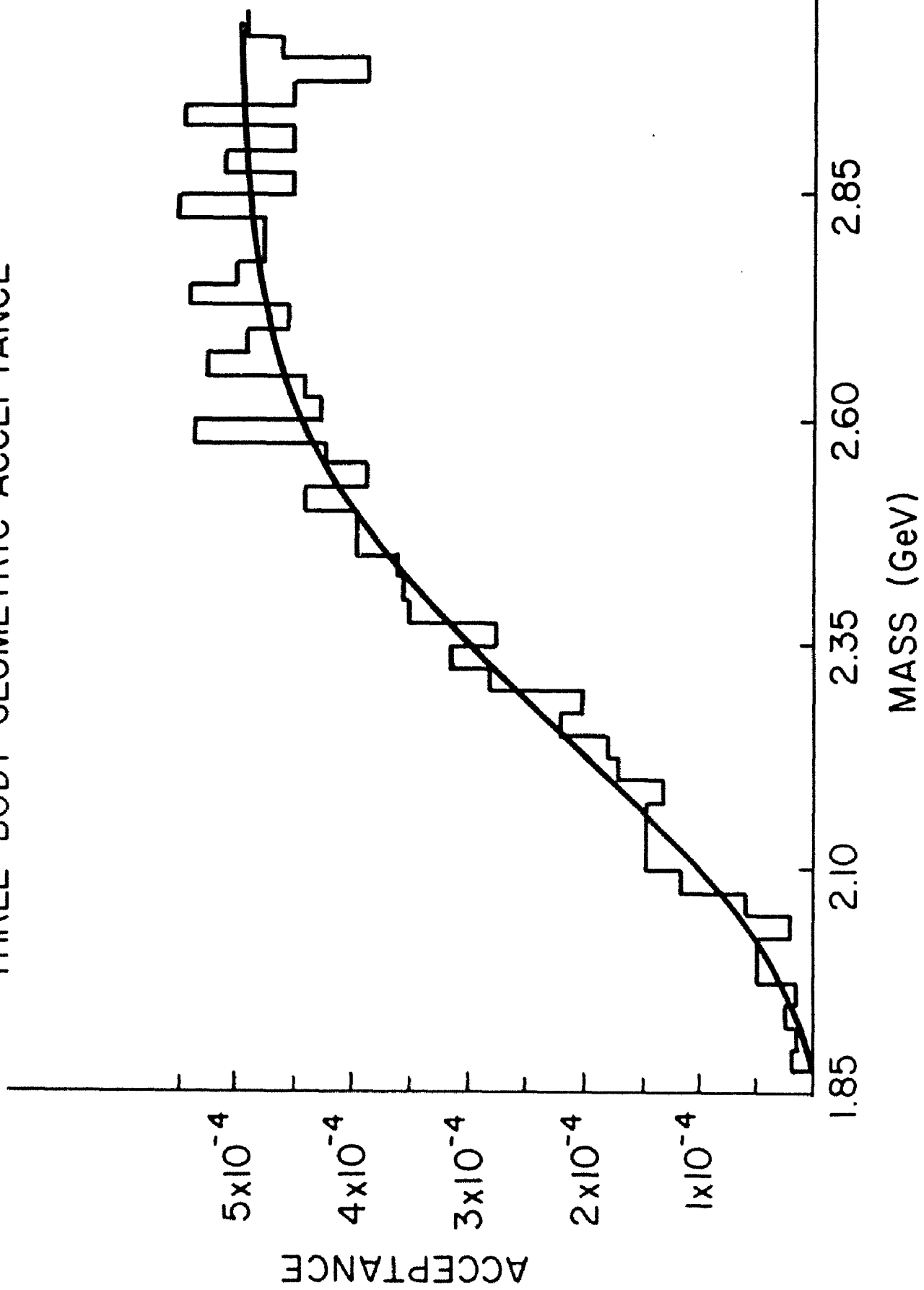


Figure 29: $\Lambda - \pi$ Acceptance Versus Mass

The events in the mass plots were weighted by the acceptance, and the sensitivity was estimated in a similar manner to the D^* and J/ψ with larger uncertainties primarily due to the non-lambda event contamination. The inclusive differential cross section for states decaying into $\Lambda \pi^-$ and $\bar{\Lambda} \pi^+$ are plotted in Figure 30. The normalization is correct to within a factor of 2, and the error bars are solely statistical.

The most striking feature of the data is the steep decline in cross section, three orders of magnitude within 1 GeV of mass. Fitting the points between 2.1 and 2.6 GeV to an exponential

$$d\sigma/dm = ke^{-\alpha m}$$

gives $\alpha = 5.09$ for the Λ events and $\alpha = 5.36$ for the $\bar{\Lambda}$ events. This stands in stark contrast to the $\alpha = 1.4$ found for πK pairs at the same mass by the Fermilab-Michigan-Purdue collaboration.⁶⁷ The Stony Brook-Columbia-Fermilab group also find $\alpha = 1.3$ but at masses between 4 and 9 GeV.⁶⁸

Both of the other experiments used a proton beam and were looking at neutral final states. The CSF results do show an increase in α with the mass of the final state constituents.⁶⁹ Our result may be interpreted qualitatively to show the difficulty in producing a strange baryon from an initial system containing only up and down valence quarks, but for the moment there are no other experiments or theoretical models to use as the basis for a quantitative comparison.

⁶⁷ D. Finley, private communication. See D. Bintinger *et al.*, Phys. Rev. Lett. 37, 732 (1976).

⁶⁸ Kephart, *et al.*, Phys. Rev. Lett. 39, 1440 (1977).

⁶⁹ In their subsequent paper, H. Jostlein, *et al.*, Phys. Rev. D 20, 53 (1979), they abandon the analysis of the mass of the hadron pairs and concentrate on the transverse momentum correlations.

LAMBDA - PION
DIFFERENTIAL CROSS SECTION

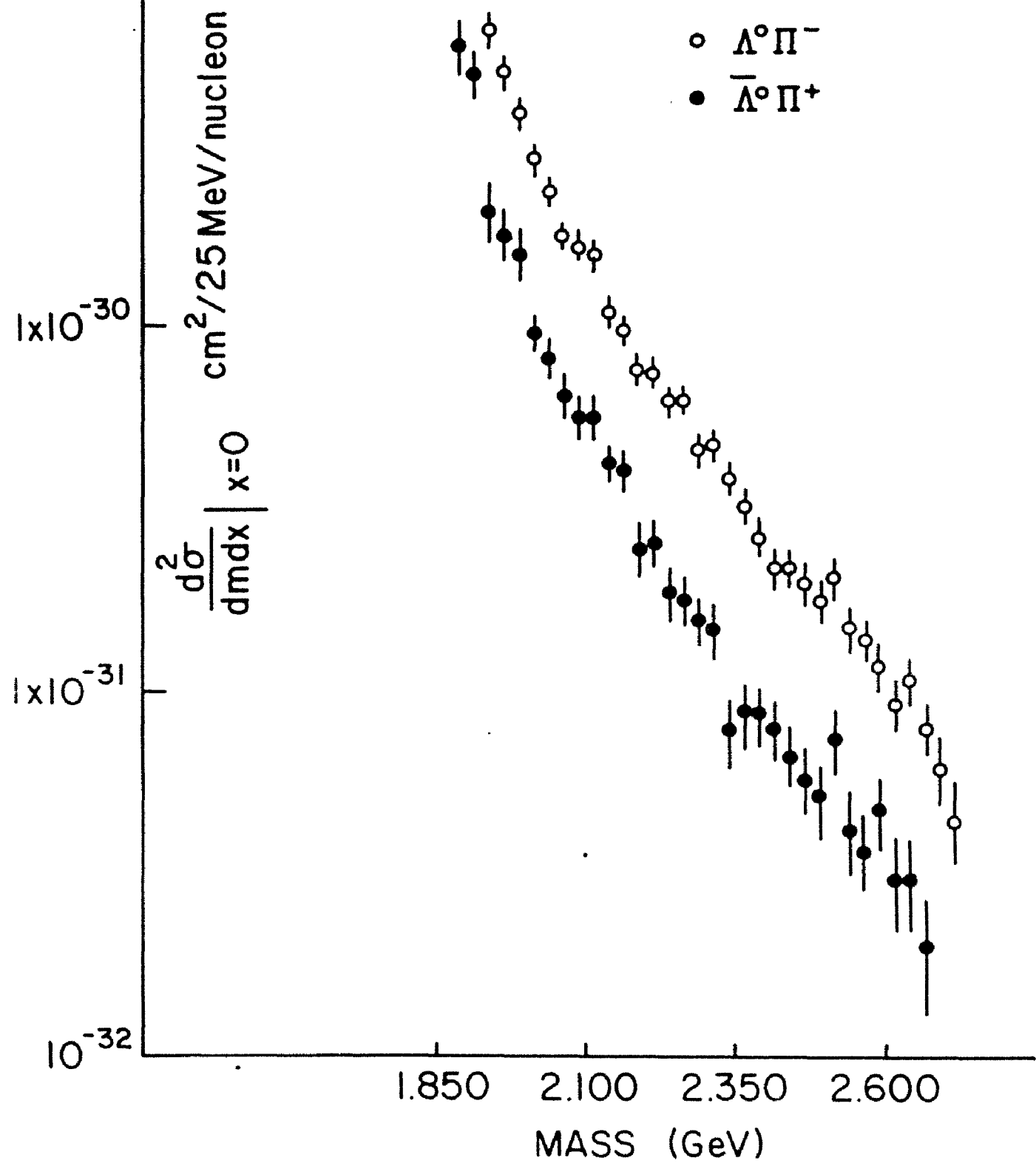


Figure 30: $\Lambda - \pi$ Differential Cross Section

4.3 D^*

The sample of D^* candidate events for the 250 GeV/c run was obtained by filtering the DST's for events containing a $K^+\pi^-\pi^-$ or $K^-\pi^+\pi^+$. The same computer program that performed the final mass calculations was used, but the vertex cuts were wider than those in the final plots. The filtration reduced the 17 DST's to two filtered DST's. Each time a significant change was made in the analysis code, the filtration was redone in order to insure that no events that should have appeared in the final sample were missed.

For convenience in quickly generating different distributions further filtrations were made. These filtrations, which could be kept on disk, had cuts on the mass and Q value as well as more stringent vertex requirements. In the final analysis, the distributions made using the the disk files and the particle identity filtered tapes were found to be identical, as was expected.

The three body mass spectra were plotted, and no significant enhancements were found. Their sum is shown in Figure 31. The absence of an enhancement in the three body mass distribution comes as no surprise because the three body spectrum fails to take advantage of the kinematics of the D^* decay. To do that one must generate a scatter plot of the mass of the K π pair versus the Q value for each event. The scatter plot in the region of the D^* is presented in Figure 32. Again, no enhancement is present.

To be sure that there was no systematic error shifting the mass away from the expected value, a search for a signal was performed by plotting the K π mass distribution while scanning over the Q value varying both the width and the center of the window in Q. The same procedure was

MASS DISTRIBUTION
 $K^+\pi^-\pi^- + K^-\pi^+\pi^+$

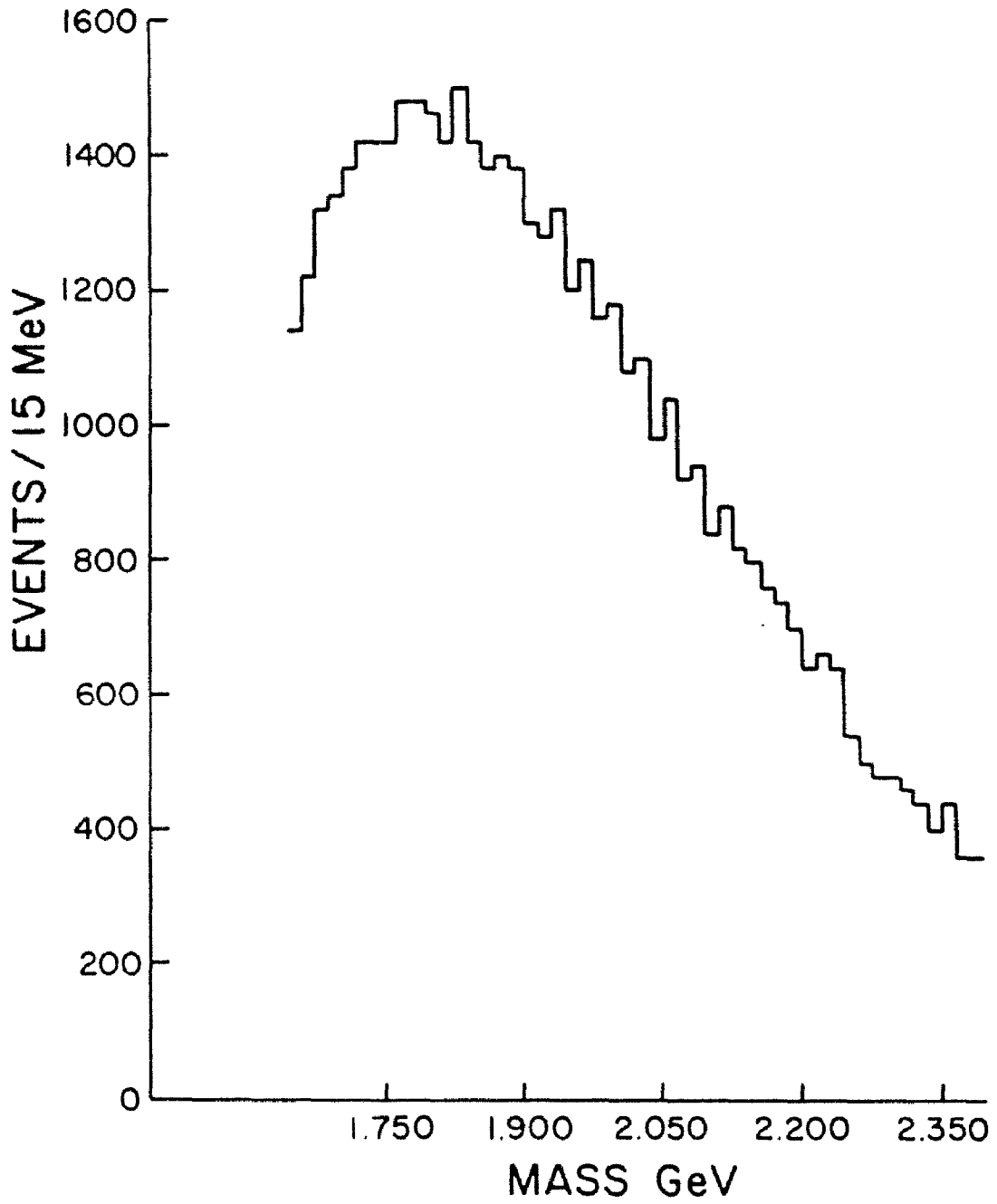


Figure 31: $K\pi\pi$ Mass Spectrum

SCATTER PLOT
MASS VERSUS Q

Q MeV

	3.0	3.5	4.0	4.5	5.0	5.5	6.0	6.5	7.0	7.5
1.736	12	8	15	16	20	20	11	19	16	13
1.808	18	10	10	11	14	20	12	11	12	9
1.820	11	11	16	13	11	13	12	15	4	9
1.832	15	11	12	8	8	10	13	11	14	12
1.844	11	9	12	10	9	15	17	18	14	13
1.856	11	13	15	9	11	6	9	7	14	11
1.868	8	9	13	14	12	15	14	19	15	13
1.880	6	15	15	12	9	17	8	9	10	12
1.892	11	13	9	17	9	9	13	13	12	11
1.904	12	6	14	11	9	13	14	15	11	9

Figure 32: Mass Versus Q Scatter Plot

followed looking at the Q distribution while scanning in mass. The search was performed both by eye and using the library computer program MINUIT. In no case did a peak in one variable correspond to one in the other when the peak was used as a window.

The final mass distributions, summed over the two signs, are plotted in Figure 33. The mass distribution is shown with Q cut both on a value window and on the basis of the error calculated event by event as described in the last chapter. The solid curves represent a fit to the background spectra which are presented in Figure 34. These spectra were obtained by omitting the region of the D^* from the K π mass and Q value distributions. The mass was fit to a third degree polynomial using MINUIT, and the Q spectrum to a function of the form:

$$A(1 - BQ)(1 - e^{-CQ^7})$$

When applying the background shapes to the actual distributions, only the overall scale was permitted to float. In every case, as shown in the Figures, $\chi^2/(\text{number of degrees of freedom})$ was close to unity. When using MINUIT to search for peaks, a Gaussian of width compatible with our resolution was superimposed on the background shape. Figure 35 illustrates our scanning technique. It was plotted in response to an enhancement MINUIT found in Figure 33 at a Q value of 7.0 MeV.

Fitting a Gaussian to the mass distribution of Figure 33 with the constraints that it be centered at 1.863 GeV, the D^* mass, and have a standard deviation of .011 GeV results in a peak having an area 7.63 events. The same procedure applied to the Q value distribution, with the center fixed at 5.7 MeV and the width set to .55 MeV, shows a dip of

3.47 events. Our D^* measurement is the average of these two numbers, 2.08 events, over a background of 61.5 events.

The calculation of the sensitivity for the D^* is summarized in Table 10. More factors enter than for the J/ψ because of the additional information from the third arm and the fast arm momentum correlation trigger requirement. The result is a sensitivity of 2.7 $\mu\text{barn}/\text{event}$. The measurement of D^* cross section at 250 GeV/c incident pion momentum is therefore

$$\left[\sigma(D^{*+}) + \sigma(D^{*-}) \right] = 0.8 \pm 2.9 \text{ } \mu\text{barns.}$$

Recall that the result of the 200 GeV/c running expressed in the same terms is

$$\left[\sigma(D^{*+}) + \sigma(D^{*-}) \right] = 8.4 \pm 2.8 \text{ } \mu\text{barns.}$$

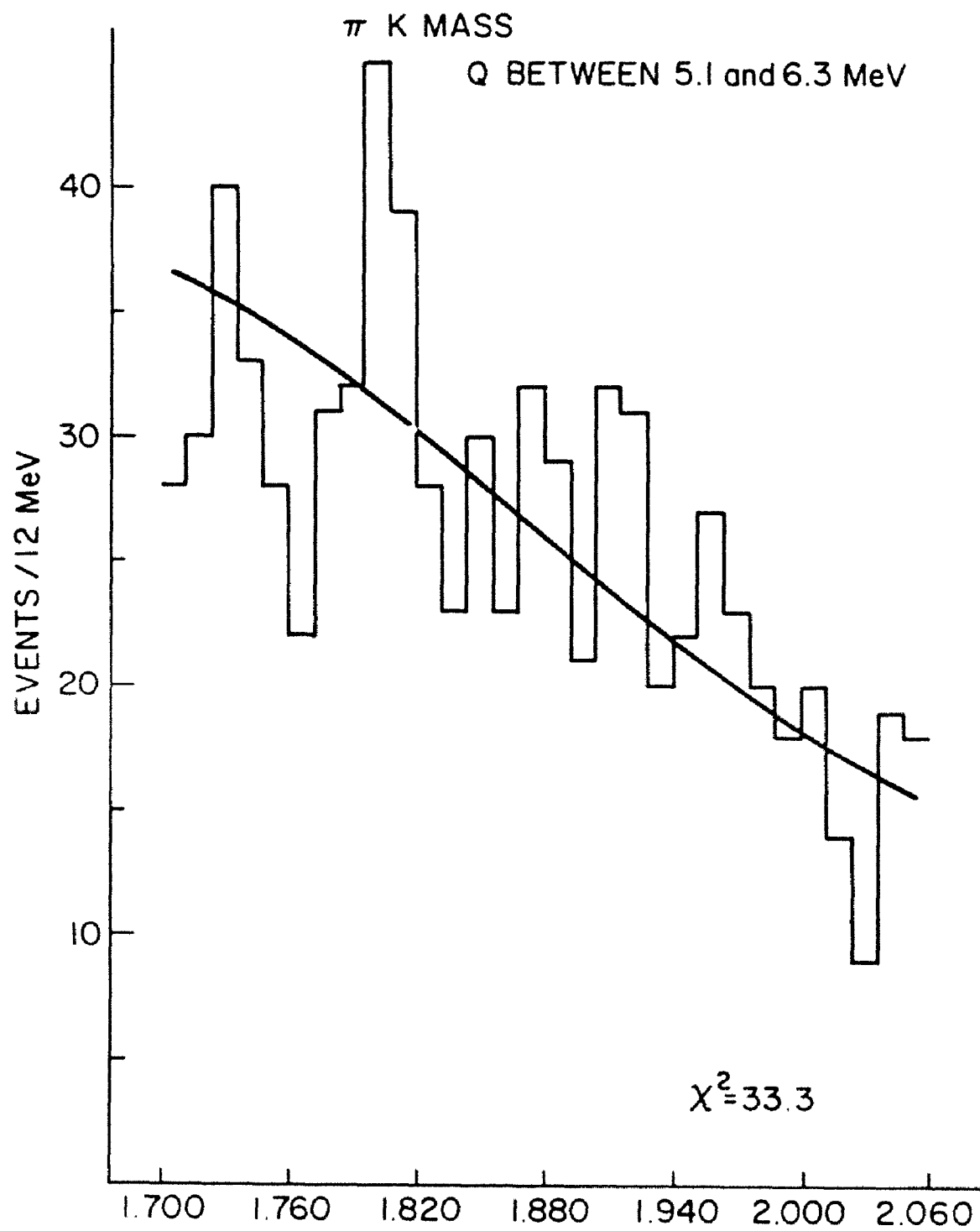
These two results are three standard deviations apart. If the D^* cross section rises with energy the same way as the J/ψ cross section does, we would expect to have measured a cross section about 10 percent higher at 250 GeV/c than at 200 GeV/c.⁷⁰

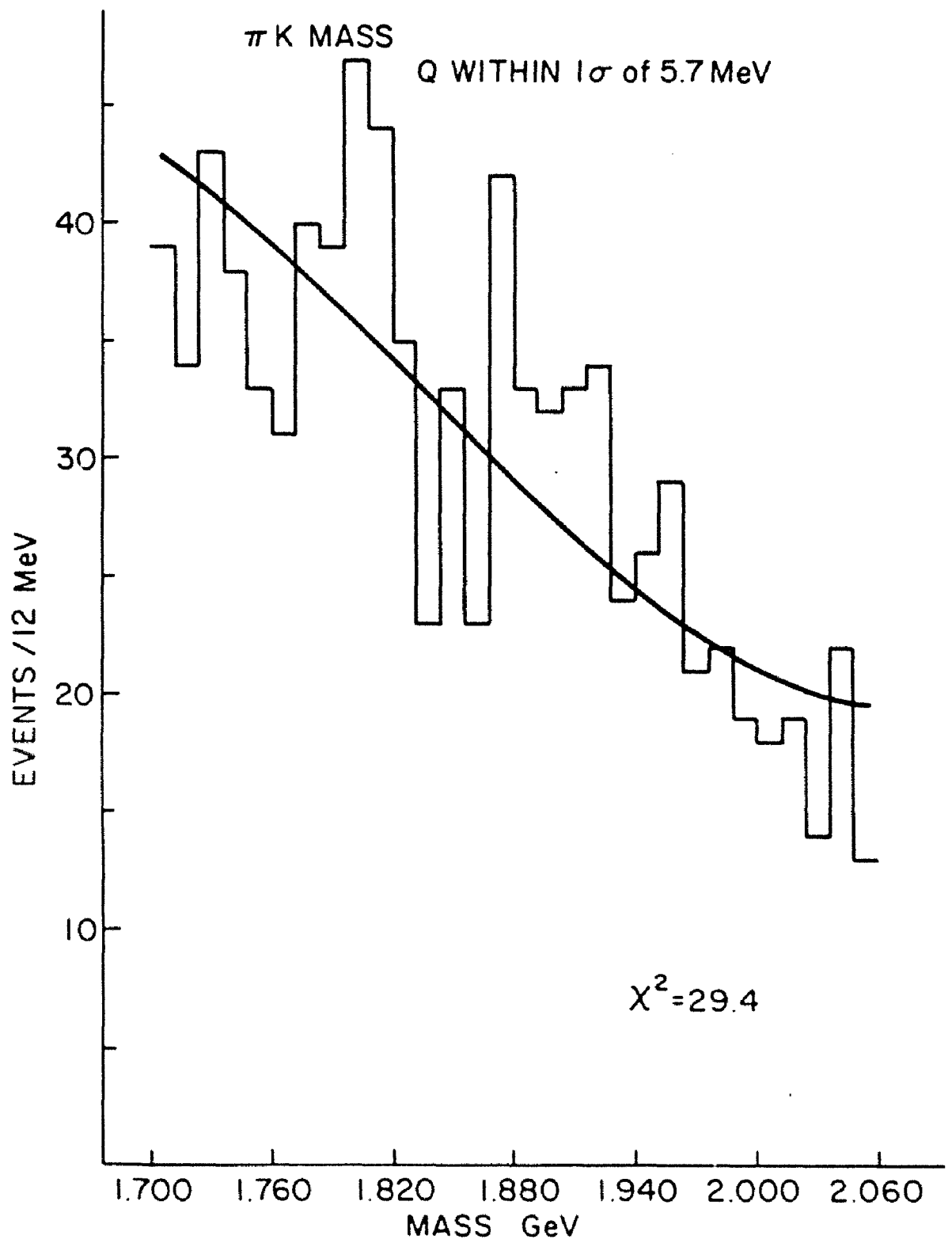
Neglecting the energy dependence of the cross section, we can consider these results as two independent measurements of D^* production. Taking their average yields a final result of

$$\left[\sigma(D^{*+}) + \sigma(D^{*-}) \right] = 4.6 \pm 2.0 \text{ } \mu\text{barns}$$

with each contribution 1.5 standard deviations away from the mean.

⁷⁰ See reference 41.





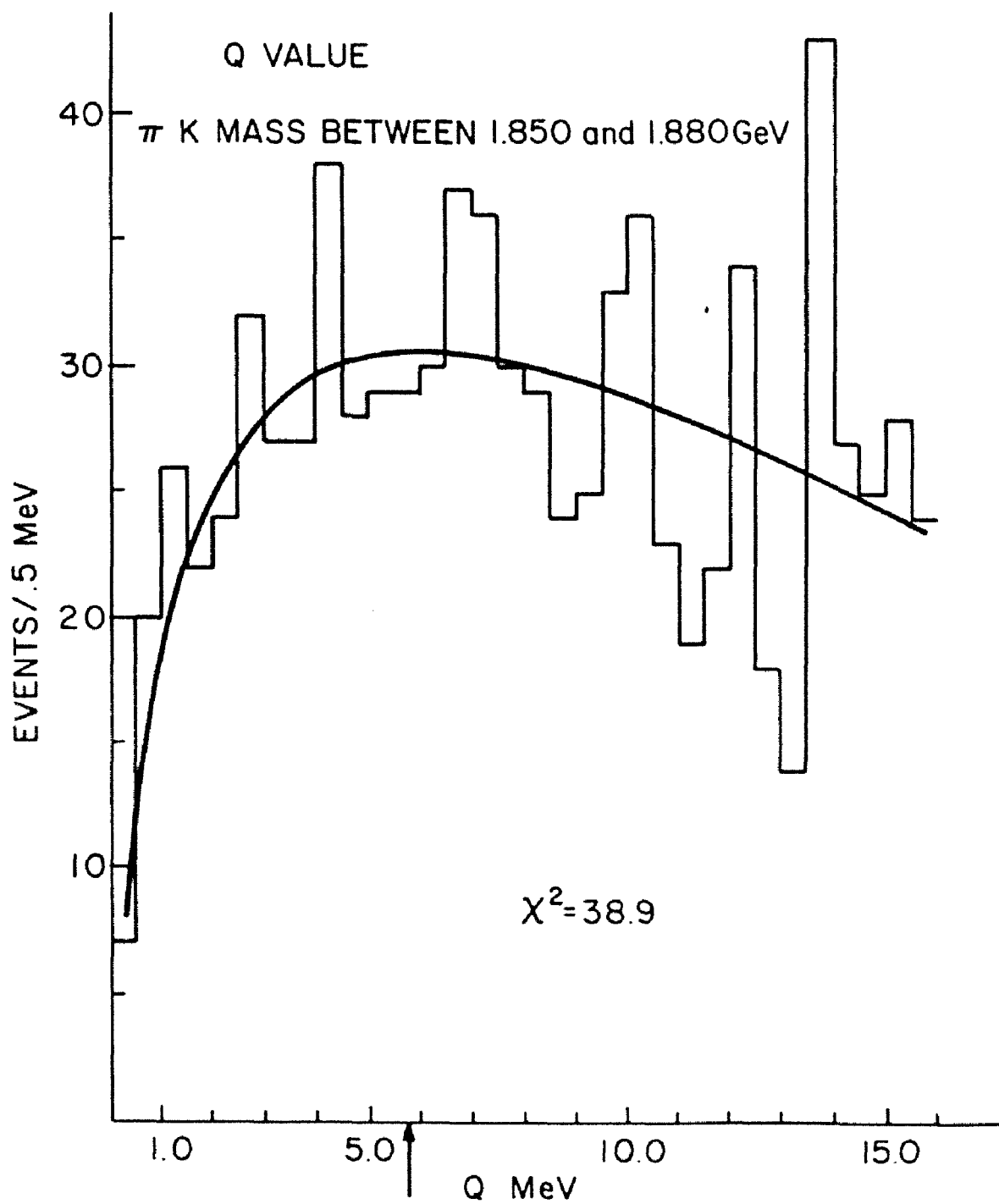
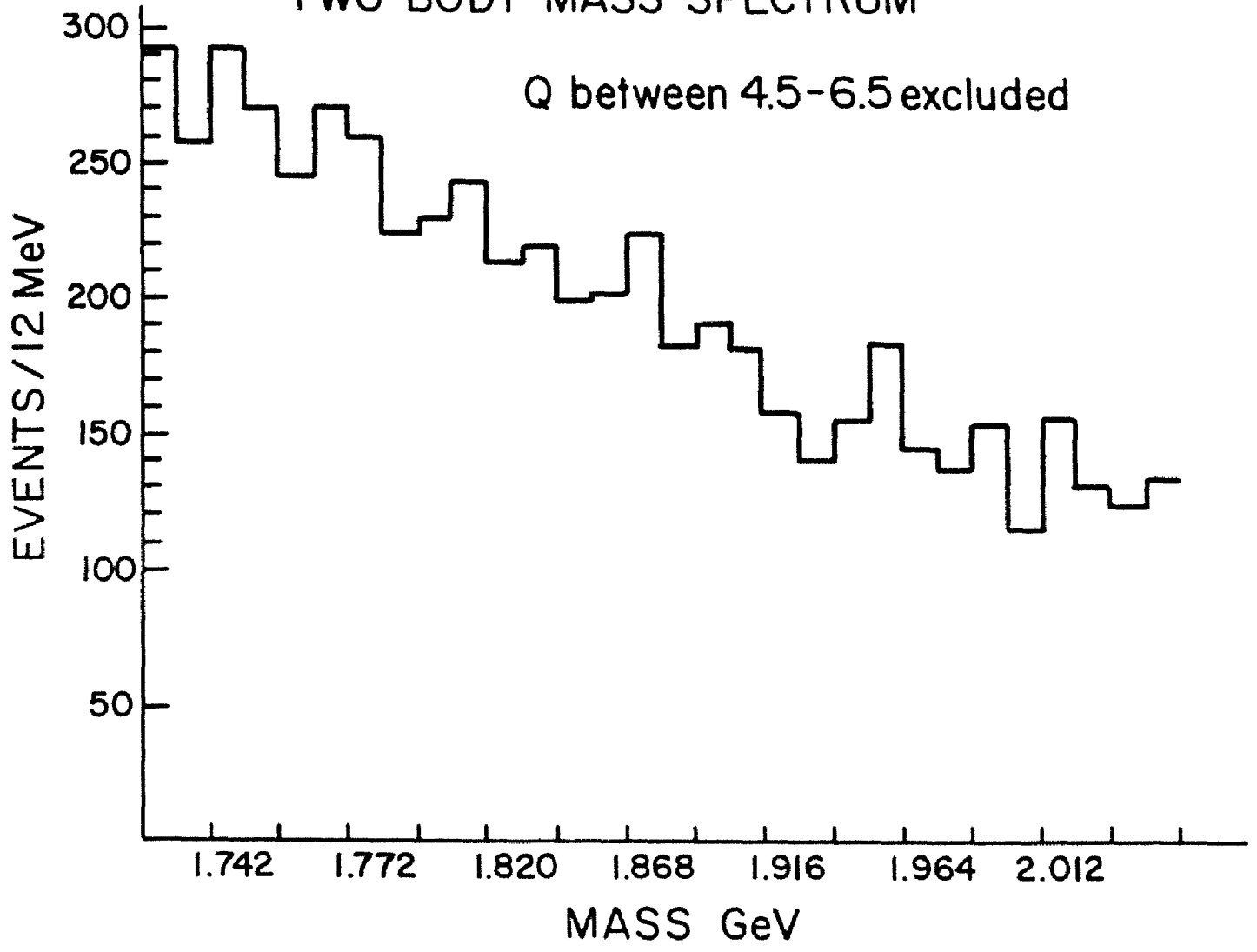


Figure 33: D^* Mass Plots

TWO BODY MASS SPECTRUM

Q between 4.5-6.5 excluded



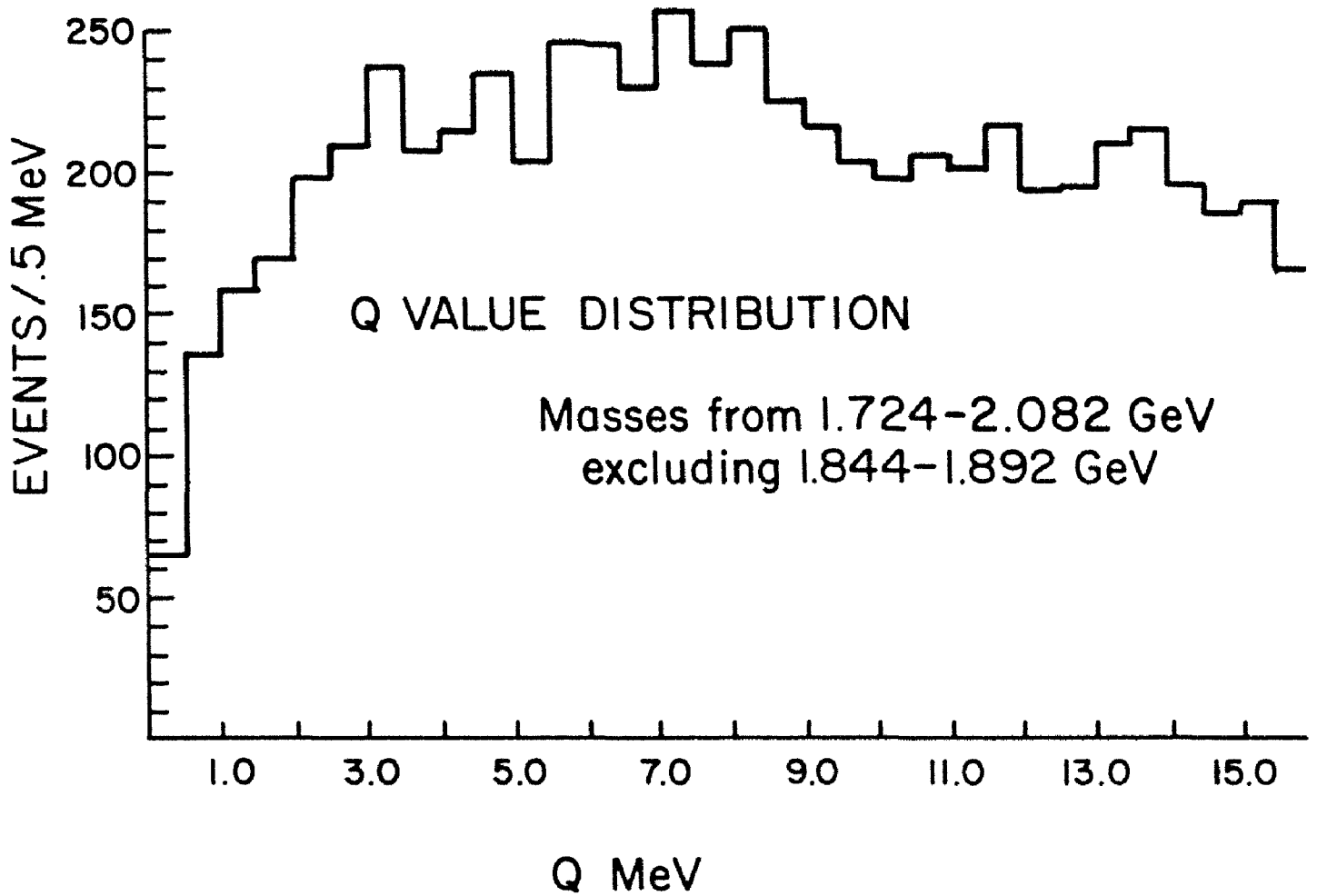


Figure 34: Background Distributions

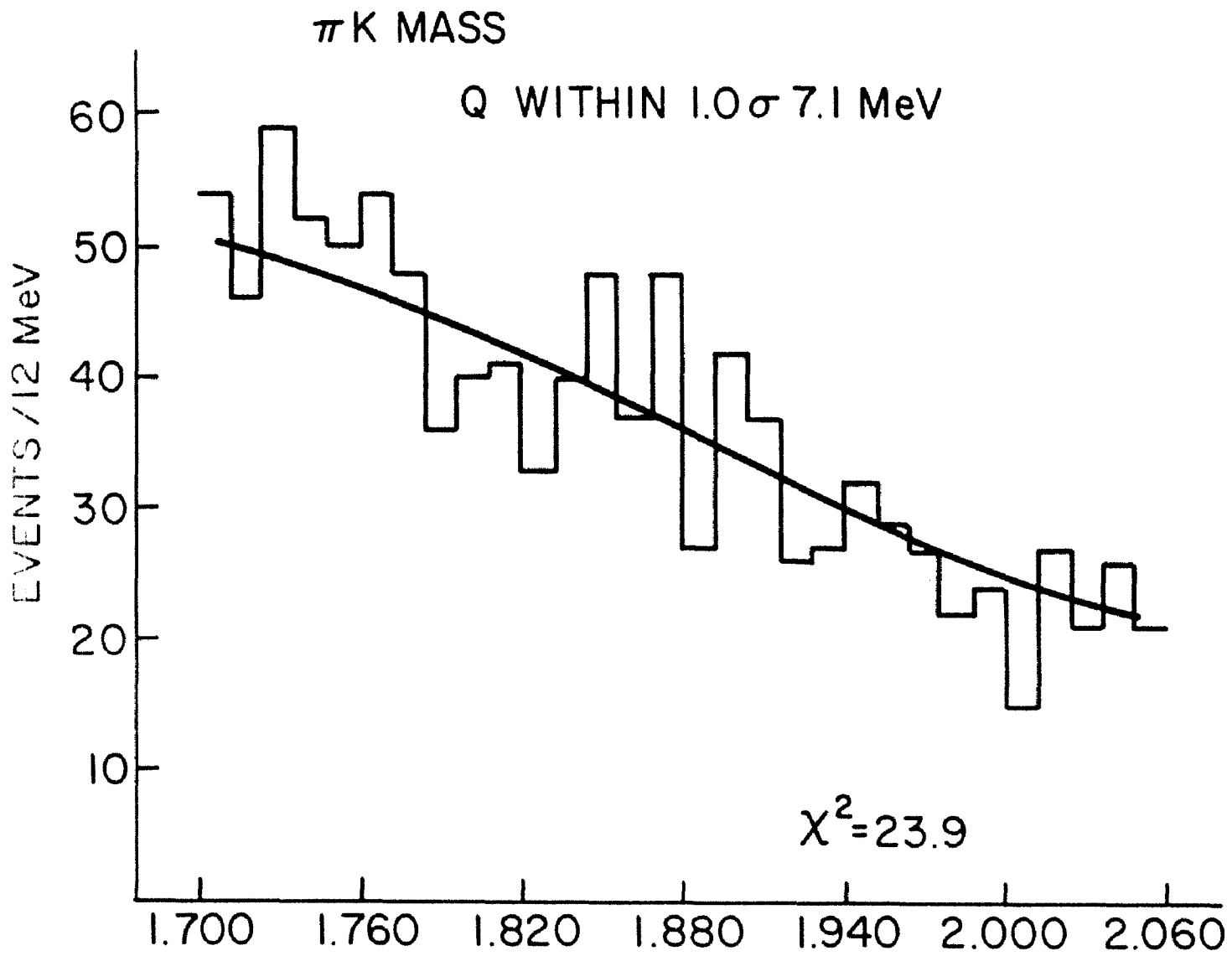


Figure 35: Mass Plot for Q near 7.1 MeV

TABLE 10
Sensitivity for D^*

Number of beam-target interactions	1.2 x 10 ¹¹
Total cross section/nucleon	25 mb
Geometric acceptance of spectrometer	2.4 x 10 ⁻⁴
Efficiencies	
Data Acquisition	
Trigger hodoscopes	.95
Mass matrix	.89
K decay	.80
Reconstruction	
R-L recovery	(.71) ²
Up-Down recovery	.54
Vertex R-L	.77
Vertex Up-Down	.85
Branching ratios	
$D^{*+} \rightarrow D^0 \pi^+$.60
$D^0 \rightarrow K^- \pi^+$.03
Sensitivity for $D^* = 2.7 \pm .5$ events/microbarn	

4.4 CONCLUSIONS

To compare these results with other experiments and with theory, the measured D^* cross section must be related to the total charm cross section. Consider first the fraction of charged D^* to all D meson production. The three assumptions of equal up and down quark mass, associated production of D meson pairs, and production weighted according to the number of spin degrees of freedom lead to the following ratios for D production:

$$D^{*0} : D^{*+} : D^0 : D^+ \\ 3 : 3 : 1 : 1$$

⁷¹ This argument was first made by J.L. Rosner in Proceedings of the 1978 Bartol Foundation Conference on Cosmic Rays and Particle Physics, edited by T. Gaisser (New York: American Institute of Physics, 1979) p. 297. Note that $\sigma(\text{charm})$ refers to states of charm +1 which under the assumption of associated production is equal to the cross section for states with charm -1.

That implies $\sigma(D^{*+})/\sigma(\text{charm}) = 3/8$.⁷¹ Our result for associated DD production is then

$$\sigma(DD) = 6.1 \pm 2.7 \text{ } \mu\text{barns} .$$

Even at this energy the total charm cross section must include contributions from strange, charmed mesons and charmed baryons. The F^{*+} and F^+ mesons represent an additional four states, but the experimental evidence for them is scant.⁷² If we say that the suppression for dressing a charm quark with a strange quark follows the production ratio $\sigma(K^{*+})/\sigma(\rho^0)$ which is approximately .3, we get an extra contribution of 1.2 to the 8 in the total charm denominator. As for the charmed baryons, comparing charmed baryon production⁷³ with charm meson production⁷⁴ in e^+e^- machines, we should add another quarter of the total to the denominator making the ratio

$$\sigma(D^{*+})/\sigma(c\bar{c}) = 3/11.5$$

for a final result of

$$\sigma(c\bar{c}) = 8.8 \pm 3.8 \text{ } \mu\text{barns} .$$

Based on the general scheme outlined in the first chapter, we would expect a total charm cross section somewhere in the region of fifteen microbarns. Our result is lower than this by about a factor of two, but our sensitivity (especially in the 250 GeV/c running) is not great enough to present a conclusive challenge to the consensus. These results underscore the difficulties that have persisted in performing direct measurements of charm production. Nonetheless, if we maintain that measuring charm production is a useful probe of fundamental physics and that direct observation is the only reliable signature, then these ef-

⁷² See Goldhaber and Wiss, op. cit., reference 27.

⁷³ G.S. Abrams Phys. Rev. Lett., 44, 10 (1980).

⁷⁴ Petros-Afentoulis Rapidis, Ph.D. thesis, SLAC Report 220 (1979).

forts should continue. Future experiments, at least those at energies comparable to ours, will have to be designed with at least an order of magnitude greater sensitivity if they are to achieve results that will elucidate the mechanisms of charm production, and they should be carried out in the entire range of x . Those who set out to measure beauty and the flavors beyond should keep the experience of charm in mind.